Numerical approximation of higher-dimensional Continuum Dislocation Dynamics theory in single crystal plasticity

Zur Erlangung des akademischen Grades eines

DOKTORS DER NATURWISSENSCHAFTEN

von der Fakultät für Mathematik des
Karlsruher Instituts für Technologie (KIT)
genehmigte

DISSERTATION

von
M.Sc. Ekkachai Thawinan
aus
Roi-Et, Thailand

Hauptreferent: Prof. Dr. Christian Wieners
Korreferent: Prof. Dr. Willy Dörfler
Tag der mündlichen Prüfung: 07.10.2015

Acknowlegements

Contents

1 | Introduction

Observation and multiscale in plastic deformation

Models of plastic deformation of crystals have different perspectives based on scales of observation. Crystal plasticity presents a multiscale problem in time and in space of considerable complexity. It is worth to understand how plastic deformation can be observed and considered in material science which can benefit the development of models that aimed at explaining the behavior of materials in the interested scale.

The observations of slip lines in natural metal single crystals such as Cu, Ag, and Au leaded to the establishment of the concept of the glide plane in metal by Mügge as early as 1899. This was already before the work of Laue, Friedrich, and Knipping in 1912 that X-rays had become available as a tool for studying crystal structures, crystallographic orientations and the perfection of crystals. X-ray diffraction studies of deformed crystals confirmed not only the conclusions on the crystallography of the glide processes drawn earlier from surface observations but also demonstrated convincingly that plastic deformation preserved the crystal structure as well as the specific volume within the experimental accuracy achievable at the time. The results shown by the X-ray diffractograms of deformed crystals was correctly interpreted as being caused by local rotations of the crystal structure around an axis lying in the glide plane perpendicular to the glide direction.

Subsequent attempts to explain the discrepancy between the theoretically predicted shear strength of a metal and the experimentally observed yield stresses lead to the concept of the *dislocation*, a linear crystal defect, which was proposed in 1934 almost simultaneously by Orowan, Polanyi, and Taylor.

The approach to dislocation to dislocation theory proved exceedingly successful in accounting, often quantitatively, for physical phenomena that are governed primarily by the properties of individual dislocations. To some extent the mechanistic approach was assisted by the possibility to observe individual dislocations by transmission electron microscopy (TEM) and thus to test many of its predictions.

Therefore, the plastic deformation involves interconnected processes on length scales that extend from the atomistic scale, on which the arrangement of single atoms is

considered, to the concept of dislocations and up to the macroscopic scale given by the specimen size.

10^{-8} m		10^{-6} m	10^{-4} m	10^{-2} m
atomistic	microscopic	mesoscopic I	mesoscopic II	macroscopic
dislocaiton cores	individual dislocaitons	dislocaiton ensembles	grain structure texture	external tractions
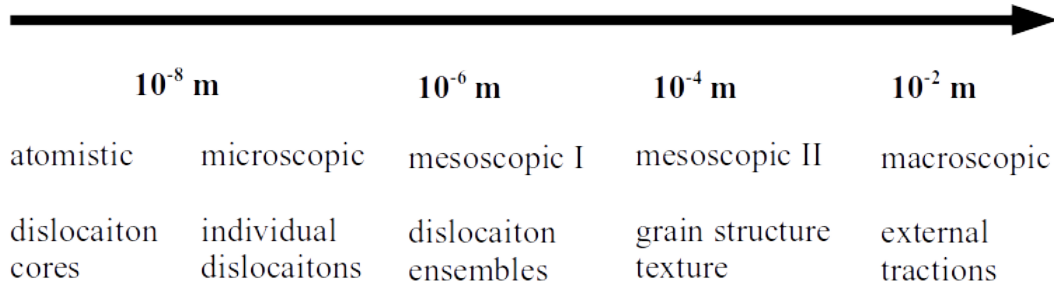
Figure 1.1: Length scales associated with dislocation systems

Appropriate length scales may be defined as follows:

- The *atomistic scale* deals with the arrangement and the interactions between individual atoms. These interactions govern the dislocation core structures and, therefore, influence dislocation mobilities and short-range interactions between dislocations.

- On the microscopic scale the elementary 'units' of plastic deformation are dislocation segments or isolated dislocation lines. On this scale, dislocations are treated as line singularities in an elastic continuum. The appropriate tool for calculating their stress fields and the elastic interactions mediated by these fields is continuum mechanics. In many cases the dislocation motion can be described by force-velocity relationships.

- The mesoscopic scale is the spatial scale on which the evolution of the dislocation system may be described in terms of dislocation densities and dislocation correlation functions. On this scale, it is expedient to consider separately the external stress and the internal stress arising from the superposition of the stress fields of a large number of dislocations and spatially varying on the length scale. Under certain circumstances it may be appropriate to introduce a hierarchy of mesoscopic scales, e.g. in polycrystals whose grain size is small compared with the macroscopic dimensions. In this example two mesoscopic scales arise naturally. mesoscopic scale I deals with the dislocation patterns (cells, subgrains, etc.) within the grains, whereas mesoscopic scale II comprises many grains.

- On the macroscopic scale, the specimen may be considered as being composed of macroscopic volume elements whose extensions are large compared to the mesoscopic length scales of the microstructure. On this scale, it is in many cases possible to describe the plastic response by deterministic constitutive laws which result from averaging over the dynamics of the dislocation system on microscopic and mesoscopic scales.

A brief history of modeling

From the top down point of view, phenomenological continuum models for plasticity which are not based on dislocation mechanics have been successful in a wide range of engineering applications. They operate on length scales where the properties of materials and systems are scale invariant. The scale-invariance, however, breaks down at dimensions below a few micro-meters, which is also a scale of growing technological interest. These microstructural effects become more and more pronounced in small systems and lead to so-called 'size effects' (e.g. Ashby, 1970; Arzt, 1998) and various experimental work (e.g. Stolken and Evans, 1998; Fleck et al., 1994). Phenomenological continuum theories incorporate internal length scales by introducing strain gradient terms - sometimes based on the consideration of GND densities - into their constitutive equations (e.g. Fleck et al., 1994; Nix and Gao, 1998; Gurtin, 2002; Gao and Huang, 2003) but are not able to consider fluxes of dislocations or the conversion of SSDs into GNDs and vice versa. The benefit of these approach are that there are a firm basis in mathematics formulation based on convex analysis which leads to the well posed problem of numerical methods. This also include advanced models for gradient plasticity introduced by , e.g., Gurtin et al. (2007). These models are analyzed numerically by Wieners and Wohlmuth (2011) and for gradient crystal plasticity Reddy et al. (2012) which are already realized numerically by using the framework of the energetic approach of A. Mielke Mielke (2005). However these are not the approach that can explain and take the account of the interaction of dislocations to the consideration.

On the other hand from the button up approach from the microstructure, Discrete dislocation dynamics (DDD) models (e.g. Kubin and Canova, 1992; Devincre and Kubin, 1997; Fivel et al., 1997; Ghoniem et al., 2000; Weygand et al., 2002; Bulatov and W., 2002; Arsenlis et al., 2007; Zhou et al., 2010) contain very detailed information about the dislocation microstructure and the interaction and evolution of dislocations and have been very successful over the last two decades in predicting plasticity at the micro-meter scale. DDD simulations allow to investigate very complex plastic deformation mechanisms but are, however, due to their high computational cost limited to very small system size/small densities.

In the level of mesoscopic scale, there were some investigation already about two decades after the invention of the idea of dislocations leading by Kondo (1952); Nye (1953); Bilby et al. (1955); Kröner (1958) independently introduced equivalent measures for the average plastic deformation state of a crystal in the form of a second-rank dislocation density tensor. This 'Kröner-Nye tensor' is introduced to link the microscopically discontinuous to a macroscopically continuous deformation state and is the fundamental quantity in Kröner's continuum theory of dislocations. This

tensor, however, only captures inhomogeneous plastic deformation states associated with so-called geometrically necessary dislocations (GNDs) and does not account for the accumulation of so-called statistically stored dislocations (SSDs) in homogeneous plasticity. This renders the classical dislocation density measure problematic as a foundation for a continuum theory of plasticity.

Later in order to generalize the classical continuum theory of dislocations, Groma and coworkers Groma (1997); Groma et al. (2003) used methods from statistical physics to describe systems of positive and negative straight edge dislocations in analogy to densities of charged point particles. They derived evolution equations which are able to faithfully describe fluxes of signed edge dislocations. The subsequent generalization to systems of curved dislocation loops, however is not straightforward. Pioneering steps into that direction have been undertaken by Kosevich (1979); El-Azab (2000); Sedláček et al. (2003) and 'screw-edge' representations also by Zaiser and Hochrainer (2006); Arsenlis et al. (2004); Reuber et al. (2014). A new approach based on statistical averages of differential geometrical formulations of dislocation lines has been done by Hochrainer et al. (Hochrainer (2006); Hochrainer et al. (2007); Sandfeld (2010a); Sandfeld et al. (2010)) who generalized the statistical approach of Groma towards systems of dislocations with arbitrary line orientation and line curvature introducing the higher-dimensional Continuum Dislocation Dynamics (hdCDD) theory. The key idea of hdCDD is based on mapping spatial, parameterized dislocation lines into a higher-dimensional configuration space, which contains the local line orientation as additional information. In order to avoid the high computation cost of the higher-dimensional configuration space 'integrated' variants of hdCDD - denoted by CDD - have also been developed recently Hochrainer et al. (2009); Sandfeld et al. (2011); Hochrainer et al. (2013); Monavari et al. (2014); Hochrainer (2015). Their simplifying assumptions already have been benchmarked for a number of situation. Until now, hdCDD nonetheless serves as the reference method for all CDD formulations, since it can be considered as an almost exact continuum representation of curved dislocations.

However a complete dislocation based plasticity theory that is based on hdCDD and CDD was not developed from the beginning because the aim of the development of these theories were only trying to establish the mathematical framework needed to perform meaningful averages over systems of moving curved dislocations that provide a consistent framework for a statistical mechanics of curved dislocation lines. The first attempt to investigate the full hdCDD based plasticity was proposed by Sandfeld et al. (2010). They considered the problem of micro-bending of a free-standing thin film by assuming the homogeneous of dislocation glides in the direction parallel to the film that can simplify the system to use only one representative slip plane per slip system for the simulation. This setting was limited to the given external stress

and mean field stress that was derived explicitly in Zaiser et al. (2007); Nikitas (2008). To overcome the limitation of homogeneous slip planes assumption, the relaxed system with discrete slip planes was introduced in Sandfeld et al. (2013) by using the Groma's continuum dislocations system and for a better explaination for dislocation loops in the recent work Sandfeld and Po (2015). For the system with hdCDD theory with discrete slip planes has not been studied before, due to the high computational cost of additional dimension in hdCDD system and the complexity of geometries itself. To overcome this problem the new framework and numerical methods have to be developed which is the main purpose of this work.

Within this thesis, the elasto-plasticity based on hdCDD theory will be developed by trying to answer the following questions:

- Investigate whether the hdCDD problem is well-posted.

- Develop numerical methods for hdCDD on single slip and provide a framework for parallel computation for the multi-slips on the full system.

- Develop a framework that allows the coupling of hdCDD and linear elastic problems.

- Study the behavior of the full setting by applying to thin film applications.

Outline

The structure of the thesis is organized as the following:

In **Chapter 2**, overviews of dislocations in material science and in the continuum mechanics theory together with the theory of hdCDD are discussed. For the material science perspective, the concept of individual dislocations to the concept of classical continuum theory of Kröner will be shown. On the other hand dislocation densities in continuum mechanics will be illustrated from the framework of Gurtin et al. (2007) to show the different point of views that the scalar quantity of dislocation densities can be postulated from the plastic slip that used as a internal variable in the energy framework of classical plasticity theory. Moreover the benefit of this postulated dislocation densities is shown in the concept of gradient plasticity taking this dislocation densities to be an additional internal variable that can provide a size dependent behavior to the classical plasticity theory. We finish this chapter with the introduction of hdCDD theory to show a general concept for continuum dislocation densities with arbitrary line orientation proposed by Hochreiner and a specific modeling perspective to give a connection to continuum mechanics for the numerical experiment purpose.

In **Chapter 3**, the mathematical analysis of the reformulation of hdCDD theory in a general form so called Friedrich system is discussed. The well-posedness of the

hdCDD system under the assumption that velocity of dislocation density does not depend on the orientation direction is shown. Moreover the standard discontinuous Galerkin scheme for the space discretization and explicit Runge-Kutta for the time integration (explicit-RKDG) are shown together with the error analysis of the scheme with RK3 based on the framework of Burman et al. (2010).

In **Chapter 4**, we will show the numerical result for the RKDG from previous chapter and discuss behaviors of the hdCDD system over a single slip. Furthermore, the limitation of both theory of hdCDD and our standard DG method proposed in the previous chapter are pointed out. The main problem for numerical method comes from the additional dimension of line orientation that have a drawback with a large number of degree of freedom for the dG discretization. Moreover with our proposed model of embedded slip planes in the elastic body, a standard mesh discretization of hdCDD system will also cause a problem for mesh distribution for parallel treatment. A new type of basis functions called Finite Volume Fourier elements(FVF) for DG method is introduced to overcome these problems. At the end of the chapter, one possibility of the simplified Continuum Dislocation Dynamics (sCDD) theories proposed to approximate the hdCDD system by reducing the information from the line orientation dimension will be shown.

The main results of this thesis for the full-coupled elasto-plasticity based on hdCDD theory for 2D body will be shown in **Chapter 5**. The modeling proposed in the Chapter 2 will be implemented by using the reduced hdCDD system of the embedded slip planes for the 2D body. The RKDG with FVF elements will be used for the evolution of hdCDD system as the micoscopic part together with the standard FEM methods for elastic body of macroscopic domain. The fully coupled system will be further investigated upto two slip systems by applying to the applications of thin film with tensile and shearing tests.

In **Chapter 6**, the main idea to implement DG methods is provided by modifying the existing geometric data structure so called Distributed Point Objects concept in the in-house FEM software package M++, Wieners (2010). The main difference is that in the conforming FEM, the consistency of values over nodal points on the interface of distributed domain on different processors have to be preserved, but in the case of DG these value are discrete and related to different values, so the consistency over them is not needed. However the communication between the neighboring cells is required for the numerical flux of DG scheme. With this requirement, the concept of *overlapping cells* within the geometric data structure is introduced to treat the required information for the communication of distributed meshes.

Parts of the results in this thesis are already published in:

- E. Thawinan, C.Wieners, S. Sandfeld, *The higher dimensional continuum dislocation dynamics theory: A Runge-Kutta discontinuous Galerkin approach.* Proceedings in Aplied Mathematics and Mechanics, 257-258, 2013.

- M. Hochbruck, T. Pažur, A. Schulz, E. Thawinan, C. Wieners, *Efficient time integration for discontinuous Galerkin approximations of linear wave equations.* Zeitschrift für Angewandte Mathematik und Mechanik, 95(3), 237-259, 2015.

- S. Sandfeld, E. Thawinan, C. Wieners, *A link between microstructure evolution and macroscopic response in elasto-plasticity: formulation and numerical approximation of the higher-dimensional Continuum Dislocation Dynamics.* International Journal of Plasticity, 72, 1-20, 2015.

2 | Dislocations and Single Crystal Plasticity

Overviews of dislocations in material science, dislocation densities in continuum mechanics and the theory of higher-dimensional Continuum Dislocations Dynamics (hd-CDD) are given in this chapter. The different terminology of dislocation densities in continuum mechanical and materials science will be pointed out, because although the terms such as *dislocation densities* are used in both communities, however, they refer sometimes to different quantities and therefore can lead to misunderstanding. Dislocations in material science serves the perspective of botton-up idea which is based on the structure of individual dislocations to the concept of continuum dislocation density. On the other hand dislocation densities in continuum mechanics will illustrate the different point of view that the scalar quantity of dislocation densities can be obtained from the internal variable in the energy framework of classical plasticity theory. The framework of Gurtin will be addressed and this can lead to the concept of gradient plasticity based on dislocation densities to provide a size dependent behavior to the classical plasticity theory. At the end, the theory of higher-dimensional Continuum Dislocations Dynamics (hd-CDD) is given to show a general concept for continuum dislocation densities with arbitrary line orientation by Hochreiner and a specific modeling perspective to give a connection to continuum mechanics for the numerical experiment purpose. Moreover this will provide material for the mathematical analysis and for numerical methods of hd-CDD in later chapters.

2.1 Dislocations in Material Science

2.1.1 Concept of Dislocations

Dislocation is the concept that is used to explain plastic deformation of materials which can be viewed as a defect in the crystal lattice. In general, these defects can be occurred in all dimensions such as point defects (0 dimension), line defects (1 dimension), planar defects (2 dimension) and volume defects (3 dimension). In

many cases, line defects are one of the most important classes where it can generate planar defects by the movement of the defected lines and volume defects can be viewed as the averages of defected lines over volume which leads to the concept of continuum dislocations.

The first introduction of dislocations came in the form of line singularity by Volterra (1907); Love (1927) in a continuous elastic body even before the beginning of the observation of dislocations by experiments. The explanation of Volterra can be seen in literature in the form of Volterras tubes that one can take a cylinder of material around the dislocation line, cut it along some wall, shift the surfaces of the cut in all possible ways. After welding the walls together where in some cases material has to be added or removed, this will lead to different deformation states around the dislocation line.
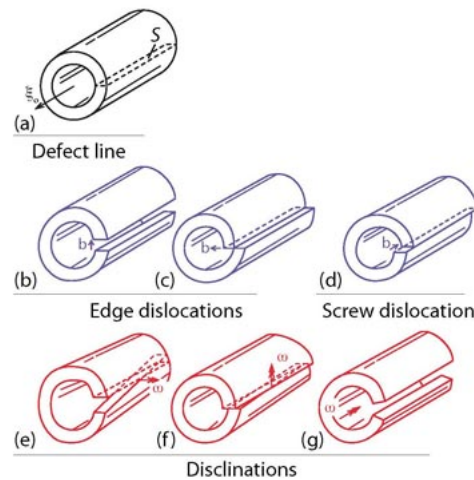
Figure 2.1: Types of Voltera's distortions tubes, Cordier et al. (2014)

The dislocation had been more welcomed in the content of planes slides of atoms on each others inside crystal in order to close the gap of predicted stresses between the experimentally observed in yield stress in actual crystal and the theoretically calculation that first calculated by Frenkel in 1926. The explanations by using the concept of dislocation were independently given by Orowan (1934); Polanyi (1934); Taylor (1934). Two important fundamental types of dislocations, edge and screw dislocations, has been used to explain the characteristic of distortion of the originally perfect crystal in particular regions around the dislocation line. Other forms of movement (e.g. so-called climb) are not considered throughout this thesis.

If one considers the special cases of dislocations as straight lines in perfect crystals, and combine with the edge and screw deformation from Volterra tube. One can see the deformation more clearly from the visualization as the deformed structure of perfect crystal. A screw dislocation will cause atoms to shift parallel to the line

direction and parallel to the moving direction of dislocation. An edge dislocation
will cause atoms to shift perpendicular to the line and parallel to the direction of
dislocation movement.
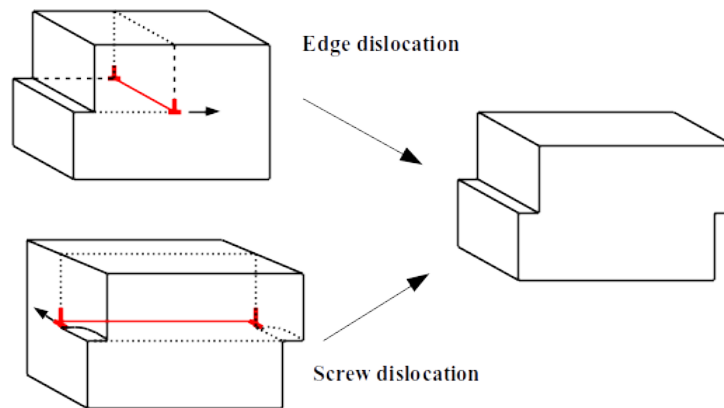
Figure 2.2: Motion of edge and screw dislocations and their formation

However the dislocation line can be in any form and is not necessary a straight line,
the case of dislocation loop will be considered in the part of hd-CDD theory.

2.1.2 Burgers Circuit, Burgers Vector and Plastic Slip

Burgers circuit/Burgers vector To fully characterize a dislocation it is necessary
to introduce the Burgers circuit. The Burgers circuit can be started by considering
a closed path in a perfect crystal, then when a dislocation, edge or screw, moves
inside the closed path and have the additional length that added up to the Burgers
circuit called Burger vector, **b**.
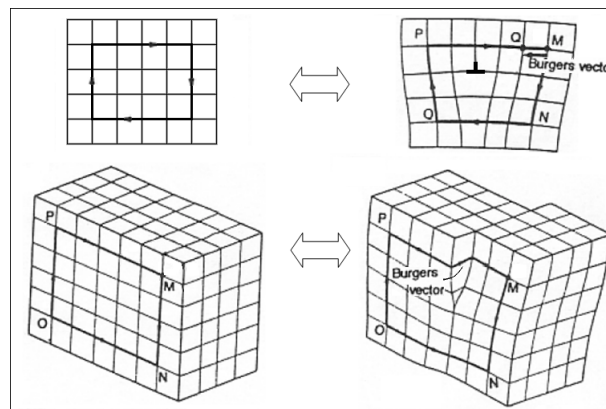
Figure 2.3: Burgers circuit in a perfect crystal and Burger vectors as additional
            length generated when edge and screw dislocations move inside the closed
            path (see https://en.wikipedia.org/wiki/Burgers_vector)

The direction of the Burgers vector depends on the direction of the orientation of
the Burgers circuit which is conventional matter. Here, the clockwise orientation

direction is used for the circuit and the Burger vector is pointed in the opposite direction. The magnitude of Burger vector, $b = |\mathbf{b}|$, is considered as the physical length between atoms in crystal structure on the glide plane.

To give the definitions of edge and screw dislocations more specifically, one can define the line direction for the dislocation line, $\hat{\mathbf{l}}$, and the movement direction, $\hat{\mathbf{v}}$, that are perpendicular to each other. The edge dislocation will create a Burger vector that is perpendicular to the dislocation line direction and parallel to the movement direction which can be interpreted as $\mathbf{b} \cdot \hat{\mathbf{l}} = 0$ and $\mathbf{b} \cdot \hat{\mathbf{v}} = \pm b$. One the other hand, the screw dislocation will create a Burger vector that is parallel to the dislocation line and perpendicular to the dislocation movement, $\mathbf{b} \cdot \hat{\mathbf{l}} = \pm b$ and $\mathbf{b} \cdot \hat{\mathbf{v}} = 0$.

Plastic slip An important measurement for plastic deformation of the dislocations system is the plastic slip, γ. This quantity is a volume based scalar and can be defined as total area swept by dislocations to the volume of considered crystal. The swept area can be illustrated by the area on the boundary on a lattice plane which as slipped by dislocations which is given by the length of dislocation line times size of Burger vector per dislocation line and can be computed by the superposition principle of the system with many dislocations. This assume to be happened on the specific lattice plane that dislocation line lays on, since only the edge and screw dislocations are considered and other forms of movement that can be seen in the Volterra cut plane are not considered.
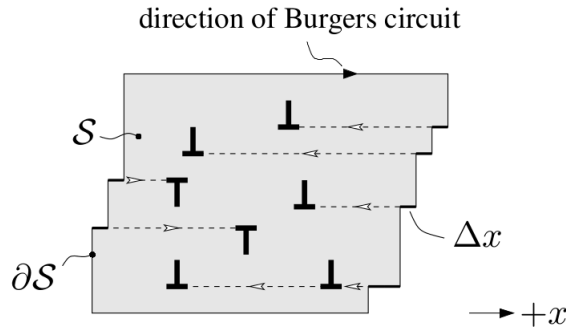
Figure 2.4: Multiple edge dislocations and their Burgers circuit $\partial\mathcal{S}$ over the area $\mathcal{S}$. Each dislocation entering the volume leave behind a surface step $\pm\triangle x$, Sandfeld (2010a).

For the case of an edge dislocation, the plastic slip can be computed as follow:

$$\gamma \quad := \quad \frac{\text{swept area}}{\text{crystal volume}} \quad = \quad \frac{\sum_i \mathbf{b} \cdot \hat{\mathbf{l}}_i l}{hl} \quad = \quad \frac{\sum_i \mathbf{b} \cdot \hat{\mathbf{l}}_i}{h},$$

where $\mathbf{l}_i$ is a line direction of each edge dislocations, h is the height of the crystal, l is the length of the dislocation line and $\mathbf{b}$ is the Burger vector with given direction.

2.1.3 Single Crystals and Slip Systems

Real metals are most often encountered in the form of polycrystalline aggregates, composed of grains separated by grain boundaries, with the grain interiors having a structure close to that of a single crystal. However, with the current work in this thesis, only single crystals are considered.

As in the previous discussion, plastic deformation in the individual crystals (grains) generally occurs via the motion of dislocations on crystallographic slip planes in crystallographic slip directions. This microscopic motion results in macroscopic motion results in macroscopic shearing of the slip planes in the silp directions. Such shears are generally referred to as slips.

The most common crystal structures in metals are:

- face-centered cubic (fcc); for example, Al, Cu, Ni, Ag, γ-Fe;

- body-centered cubic (bcc); for example, Ta, V, Mo, Cr, α-Fe;

- hexagonal close-packed (hcp); for exampel, Ti, Mg, Zn, Cd.

Schematics of these structures are shown in figure:
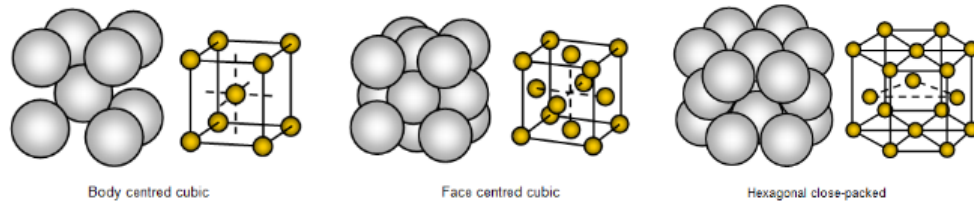
Figure 2.5: Examples of crystal structures (see http://www.schoolphysics.co.uk)

Stated precisely, plastic deformation occurs by slip in preferred slip directions which can be referred to unit Burger vector with a given direction,

$$\mathbf{d}_s, \quad s = 1, 2, ..., N,$$

on preferred slip planes identified by their normals

$$\mathbf{m}_s, \quad s = 1, 2, ..., N,$$

where $\mathbf{d}_s := \mathbf{b}_s/b$, $\mathbf{m}_s$ are constant orthonormal lattice vectors and N is referred to the number of *slip systems* that can also be represented by the pairs $(\mathbf{d}_s, \mathbf{m}_s)$. The number of slip systems depends on the structure of the crystal, for example in fcc structure there are in total 12 slip systems.

2.1.4 Connection to Continuum Dislocations Densities

The study of individual dislocation lines leads to the field of the discrete dislocation density (DDD) theory that can serve for well explanations matching with experiments. However, when the larger system is considered in the range of micrometers the DDD theory seem to reach its limitation with the complexity of the large system. The continuum dislocations density has been developed to close this gap.

The continuum framework of dislocations started from the development of the classical dislocation density tensor which was introduced independently and with slightly different accents by Nye and Kröner as well as in a much more formal way by Kondo and Bilby et al. In the following we adopt the definitions and notations by Kröner because they may directly be translated to the kinematic formalism based in differential forms which we use in the following. Nye's lattice curvature (contortion), by contrast, plays a more prominent role for the calculation of internal stresses from dislocation distributions. Kröner's dislocation density tensor $\boldsymbol{\alpha}$ is traditionally written as a second rank tensor. By definition it measures the net Burgers vector flux $\mathbf{b}$ through a surface $\mathcal{F}$, thus

$$\int_{\mathcal{F}} \boldsymbol{\alpha}^{\top} \mathbf{n} \, \mathrm{d}a \;=\; \mathbf{b}, \tag{2.1}$$

where $\mathbf{n}$ denotes the normal to the surface $\mathcal{F}$ pointing outside the crystal.
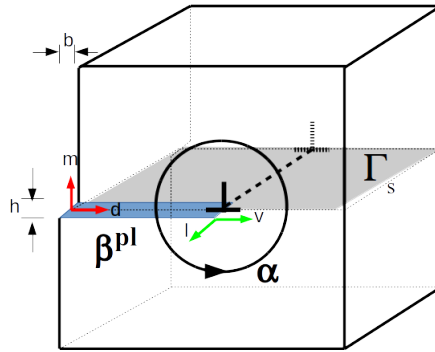
Figure 2.6: The representation of edge dislocation illustrated in the content of continuum framework

On the other hand the net Burgers vector flux through $\mathcal{F}$ may in the case of pure dislocation plasticity (which is assumed throughout the whole thesis) be determined by adding up, i.e. integrating, the plastic distortions, $\boldsymbol{\beta}^{p} := \gamma \mathbf{b} \otimes \mathbf{l}$, along the boundary curve $\mathcal{C} = \partial \mathcal{F}$. Therefore,

$$\int_{\mathcal{F}} \boldsymbol{\alpha}^{\top} \mathbf{n} \, \mathrm{d}a \;=\; \int_{\mathcal{C}} \boldsymbol{\beta}^{p} \mathbf{l} \, \mathrm{d}s \tag{2.2}$$

As a direct consequence one obtains by Stokes' theorem $\boldsymbol{\alpha} = \nabla \times \boldsymbol{\beta}^p$. The fact that dislocations do not end inside the crystal implies that $\int_{\mathcal{F}} \boldsymbol{\alpha} \mathbf{n} da = 0$ for all closed surfaces $\mathcal{F}$. By the Gauss integration theorem, $\boldsymbol{\alpha}$ as a consequence is solenoidal such that

$$\text{div } \boldsymbol{\alpha} \;=\; 0. \tag{2.3}$$

It has been known in the modeling perspective that the dislocation density tensor does – as an averaged object – not carry enough information about the dislocation state to deduce from it the rate of plastic deformation $\partial_t \boldsymbol{\beta}^p$. Because of $\partial_t \boldsymbol{\alpha} = \nabla \times \partial_t \boldsymbol{\beta}^p$, the absence of a relation between $\boldsymbol{\alpha}$ and the deformation rate implies that the evolution of $\boldsymbol{\alpha}$ itself cannot be formulated in closed form. This is the reason why it is in general not possible to build a closed theory of plasticity solely on the classical dislocation density tensor. However, the classical formulation is suited for the treatment of single dislocations as singular densities, as well as for the special situation where dislocations form smooth line bundles. Only in these special cases the dislocation density tensor contains complete information about the dislocation state, that is the total dislocation density ρ_t and the local line-direction $\mathbf{l}$. For only one glide system, $\boldsymbol{\alpha}$ in this case has the form

$$\boldsymbol{\alpha} \;=\; \rho_t \mathbf{l} \otimes \mathbf{b}, \tag{2.4}$$

with $\mathbf{b}$ denote the Burgers vector direction. Because the line direction $\mathbf{l}$ is known, it makes sense to assign to the dislocation density a smooth velocity field $\mathbf{v}$, which is at each point orthogonal to the line direction of the dislocations. From the infinitesimal area swept by a line segment, which reads $\mathbf{l} \times \mathbf{v} = -\mathbf{v} \times \mathbf{l}$, the plastic distortion rate is obtained as

$$\partial_t \boldsymbol{\beta}^p \;=\; -\rho_t \mathbf{v} \times (\mathbf{l} \otimes \mathbf{b}) = -\mathbf{v} \times \boldsymbol{\alpha}. \tag{2.5}$$

This formula was first given by Mura and is the tensorial version of Orowan's equation for the shear rate on a glide plane

$$\partial_t \gamma^p \;=\; \rho_t v b \tag{2.6}$$

with a (pseudo) scalar velocity v and b denoting the length of the Burgers vector. The closed evolution equation for the dislocation density tensor is hence given by

$$\partial_t \boldsymbol{\alpha} \;=\; -\nabla \times (\mathbf{v} \times \boldsymbol{\alpha}). \tag{2.7}$$

The above set of equations is a suitable approach for describing the kinematics of averaged systems of smooth bundles of non-intersecting dislocations – represented by a density – in a continuum framework.

One of the first successful of continuum dislocation density theory that steps into this direction was undertaken by Groma and co-workers (Groma (1997); Groma et al. (2003)). They used methods from statistical physics to describe systems of positive and negative straight edge dislocations in analogy to densities of charged point particles. They arrived at a set of evolution equations which is able to describe fluxes of signed edge dislocations, including the conversion of GND density into 'statistically stored dislocation' (SSD) density and vice versa. Similar to the Kröner-Nye framework, the dislocation velocity is again of constitutive nature. The generalization of this work with the system of only edge dislocations to arbitrary systems of dislocations with different orientations as well as varying curved geometries, however, is a highly non-trivial task. Only recently, Hochrainer and co-workers generalized the statistical approach of Groma towards systems of dislocations with arbitrary line orientation and line curvature introducing the higher-dimensional Continuum Dislocation Dynamics theory that can be found later in this section.

2.2 Dislocation Densities in Continuum Mechanics

In this section, the postulated dislocation densities in continuum mechanics will be illustrated under the framework of Gurtin et al. (2007) in the content of strain-gradient model. The classical continuum model for single-crystal plasticity will be first addressed to provide the needed information and connection to the strain-gradient single-crystal plasticity model.

2.2.1 A Classical Continuum Model for Single-crystal Plasticity

The idea behind crystal plasticity is that the plastic deformation happened with shear deformation. This simple ideas carry to introduce the plastic slip in crystals. Suppose that there are N slip systems. Each of them can be represented by a pair of two unit vectors $(\mathbf{d}_s, \mathbf{m}_s)$, $s \in \{1, ..., N\}$ where $\mathbf{d}_s$ is the direction in which slip takes place that normally is the direction of a given Burger vector and $\mathbf{m}_s$ is the normal to the plane that slip takes place. To complete the description the plastic slip along the slip plane s is denoted by γ_s. This is the same notation that we used for slip systems and plastic slip created from dislocation in the previous section.

For the global setting, let the reference configuration $\mathcal{B}$ be a bounded Lipschitz domain in $\mathbb{R}^3$ and let $\partial_D\mathcal{B} \cup \partial_N\mathcal{B} = \partial\mathcal{B}$ be a non-overlapping decompositions into

Dirichlet boundary $\partial_D \mathcal{B}$ and Neumann boundary $\partial_N \mathcal{B}$. The position of a material point is denoted by $\mathbf{x}$ and the displacement of the body from its reference configuration at time t by $\mathbf{u}(\mathbf{x}, t)$.

Small deformations are assumed so that the infinitesimal strain $\boldsymbol{\varepsilon}$ is given by

$$\boldsymbol{\varepsilon} = \boldsymbol{\varepsilon}(\mathbf{u}) = \text{sym}(\nabla \mathbf{u}), \tag{2.8}$$

where the symmetric part of a tensor is defined as

$$\text{sym}(\cdot) := \frac{1}{2}(\cdot + (\cdot)^\top) \tag{2.9}$$

and can be decomposed additively in the form

$$\boldsymbol{\varepsilon} = \boldsymbol{\varepsilon}^{\text{el}} + \boldsymbol{\varepsilon}^{\text{pl}}, \tag{2.10}$$

where $\boldsymbol{\varepsilon}^{\text{el}}$ is the elastic strain depended only of the stress, while $\boldsymbol{\varepsilon}^{\text{pl}}$ is the plastic strain depended only on the internal variables of plastic deformations.

The classical macroscopic equilibrium equation is given by

$$-\nabla \cdot \boldsymbol{\sigma} = \mathbf{f}_{\mathcal{B}} \quad \text{in } \mathcal{B} \tag{2.11}$$

where $\boldsymbol{\sigma}$ is the Cauchy stress tensor with the constitutive relation

$$\boldsymbol{\sigma} = \mathbb{C}\boldsymbol{\varepsilon}^{\text{el}} = \mathbb{C}(\boldsymbol{\varepsilon} - \boldsymbol{\varepsilon}^{\text{pl}}) \tag{2.12}$$

and $\mathbb{C}$ is the elasticity tensor. The macroscopic boundary conditions are

$$\mathbf{u} = \mathbf{u}_D \quad \text{on} \quad \partial_D \mathcal{B}, \quad \boldsymbol{\sigma}\mathbf{n} = \mathbf{t}_N \quad \text{on} \quad \partial_N \mathcal{B}. \tag{2.13}$$

The displacement gradient which sometimes is called *the deformation tensor* $D\mathbf{u}$ is assumed to be decomposed similarly to the strain $\boldsymbol{\varepsilon}$ into elastic and plastic parts $\boldsymbol{\beta}^{\text{el}}$ and $\boldsymbol{\beta}^{\text{pl}}$ respectively,

$$D\mathbf{u} = \boldsymbol{\beta}^{\text{el}} + \boldsymbol{\beta}^{\text{pl}}. \tag{2.14}$$

It follows that for a single crystal that plastic distortion $\boldsymbol{\beta}^{\text{pl}}$ coming purely from shear deformation can be completely described by the relation

$$\boldsymbol{\beta}^{\text{pl}} = \sum_{s=1}^{N} \gamma_s \mathbf{d}_s \otimes \mathbf{m}_s. \tag{2.15}$$

For later use, the tensor

$$\mathbf{M}_s = \mathbf{d}_s \otimes \mathbf{m}_s \tag{2.16}$$

is referred to as the *Schmid tensor* which is the projection tensor accounting for the orientation of the slip system s.

Depending on the vector of plastic shear strains $\boldsymbol{\gamma} = (\gamma_1, ..., \gamma_N)^\top$, the plastic strain is given by

$$\boldsymbol{\varepsilon}^{\mathrm{pl}} = \boldsymbol{\varepsilon}^{\mathrm{pl}}(\boldsymbol{\gamma}) = \mathrm{sym}(\boldsymbol{\beta}^{\mathrm{pl}}) = \sum_s \gamma_s \mathbf{M}_s^{\mathrm{sym}}, \qquad \mathbf{M}_s^{\mathrm{sym}} = \mathrm{sym}\,\mathbf{M}_s. \tag{2.17}$$

This defines the elastic strain

$$\boldsymbol{\varepsilon}^{\mathrm{el}} = \boldsymbol{\varepsilon}^{\mathrm{el}}(\mathbf{u}, \boldsymbol{\gamma}) = \boldsymbol{\varepsilon}(\mathbf{u}) - \boldsymbol{\varepsilon}^{\mathrm{pl}}(\boldsymbol{\gamma}). \tag{2.18}$$

Generalized stresses: Suppose for definiteness that the free energy ψ is a function of the elastic strain, and let $\boldsymbol{\eta} = (\eta_1, ..., \eta_N)^\top$ be a vector of scalar hardening variables for each of the slip systems. Thus the free energy can take the form

$$\psi(\boldsymbol{\varepsilon}^{\mathrm{el}}, \boldsymbol{\eta}) = \psi^{\mathrm{el}}(\boldsymbol{\varepsilon}^{\mathrm{el}}) + \psi^{\mathrm{h}}(\boldsymbol{\eta}). \tag{2.19}$$

where the free energy of elastic part is , $\psi^{\mathrm{el}}(\boldsymbol{\varepsilon}^{\mathrm{el}}) = \frac{1}{2}\boldsymbol{\varepsilon}^{\mathrm{el}} : \mathbb{C}\boldsymbol{\varepsilon}^{\mathrm{el}}$. Under the assumptions of isothermal processes and no additional heat involved, the local dissipation inequality takes the form

$$\dot{\psi} - \boldsymbol{\sigma} : \dot{\boldsymbol{\varepsilon}} \leq 0. \tag{2.20}$$

It follows that

$$-\boldsymbol{\sigma} : \dot{\boldsymbol{\varepsilon}}^{\mathrm{pl}} + \sum_s \frac{\partial \psi^h}{\partial \eta_s} \dot{\eta}_s \leq 0 \tag{2.21}$$

by using

$$\dot{\psi}^{\mathrm{el}} = \frac{\partial \psi^{\mathrm{el}}}{\partial \boldsymbol{\varepsilon}^{\mathrm{el}}} : \dot{\boldsymbol{\varepsilon}}^{\mathrm{el}} = \mathbb{C}\boldsymbol{\varepsilon}^{\mathrm{el}} : \dot{\boldsymbol{\varepsilon}}^{\mathrm{el}} = \boldsymbol{\sigma} : (\dot{\boldsymbol{\varepsilon}} - \dot{\boldsymbol{\varepsilon}}^{\mathrm{pl}}). \tag{2.22}$$

Now for the case of single crystals by using the assumption for $\boldsymbol{\varepsilon}^{\mathrm{pl}}$ and the symmetry of the stress,

$$\boldsymbol{\sigma} : \dot{\boldsymbol{\varepsilon}}^{\mathrm{pl}} = \boldsymbol{\sigma} : \sum_s \dot{\gamma}_s \mathbf{d}_s \otimes \mathbf{m}_s = \sum_s \dot{\gamma}_s \boldsymbol{\sigma} : \mathbf{d}_s \otimes \mathbf{m}_s = \sum_s \dot{\gamma}_s \tau_s. \tag{2.23}$$

where τ_s is the shear stress projection on the slip plane s. To define the generalized stresses and plastic strains, the conjugate stress of the hardening variable η_s is defined by

$$g_s = -\frac{\partial \psi^h}{\partial \eta_s}. \tag{2.24}$$

Then the reduced dissipation inequality becomes

$$\sum_s \Sigma_s \cdot \dot{P}_s = \sum_s (\tau_s \dot{\gamma}_s + g_s \dot{\eta}_s) \geq 0, \tag{2.25}$$

where Σ_s, P are defined to be the generalized stress and the plastic strains, respectively, as follows

$$\Sigma_s = (\tau_s, g_s), \quad P_s = (\gamma_s, \eta_s). \tag{2.26}$$

Yield: In phenomenological plasticity the yield function for a single crystal can take the simple form

$$\phi(\Sigma_s) := |\tau_s| + g_s - \tau_0, \tag{2.27}$$

where τ_0 is an initial yield stress and here for simplicity it can be all the same for all slip systems. The elastic regions $\mathcal{E}$ for which

$$\mathcal{E} = \bigcap_s \{(\boldsymbol{\sigma}, \mathbf{g}) \mid \phi(\Sigma_s) \leq 0, \ s = 1, ..., N\} \tag{2.28}$$

is considered. This elastic region can be shown to be convex.

Property 2.2.1. The elastic region $\mathcal{E}$ defined in (2.28) is convex.

Proof. Let $\Sigma^1 = (\boldsymbol{\sigma}_1, \mathbf{g}_1)$, $\Sigma^2 = (\boldsymbol{\sigma}_2, \mathbf{g}_2) \in \mathcal{E}$. We have to show that for any $\omega \in (0, 1)$ the combination $\omega \Sigma^1 + (1 - \omega) \Sigma^2$ is in $\mathcal{E}$. Consider on each slip system s

$$
\begin{aligned}
0 &\geq \omega \phi(\Sigma_s^1) + (1 - \omega) \phi(\Sigma_s^2) \\
&= \omega(|\tau_{s,1}| + g_{s,1} - \tau_0) + (1 - \omega)(|\tau_{s,2}| + g_{s,2} - \tau_0) \\
&\geq |\omega \tau_{s,1} + (1 - \omega) \tau_{s,2}| + \omega g_{s,1} + (1 - \omega) g_{s,2} - \tau_0 \\
&= \phi(\omega \Sigma_s^1 + (1 - \omega) \Sigma_s^2).
\end{aligned}
$$

Therefore $\omega \Sigma^1 + (1 - \omega) \Sigma^2 \in \mathcal{E}$ and thus $\mathcal{E}$ is convex. $\qquad \square$

With the principle of maximal plastic work and the reduced dissipation inequality
(2.25) and a convex yield surface, the normality law now becomes

$$\dot{\gamma}_s \; = \; \lambda_s \frac{\partial \phi}{\partial \tau_s} \tag{2.29}$$

$$\dot{\eta}_s \; = \; \lambda_s \frac{\partial \phi}{\partial g_s} \quad = \quad \lambda_s \tag{2.30}$$

where λ_s is the *plastic multiplier* together with the complementarity relations

$$\lambda_s \geq 0, \quad \phi(\Sigma_s) \leq 0, \quad \lambda_s \phi(\Sigma_s) = 0. \tag{2.31}$$

Example of hardening relations: An example of a hardening relation can be
found in Steinmann and Stein (1996) where the hardening energy ψ^h depends only
on η such that

$$\psi^h(\eta_s) \; = \; -\tau_0 \eta_s - \frac{(\tau_\infty - \tau_0)^2}{h_0} \ln\Big(\cosh\Big(\frac{h_0 \eta_s}{\tau_\infty - \tau_0} \Big) \Big), \tag{2.32}$$

with material constants τ_0, τ_∞ and h_0. Then the conjugate stress g_s takes the form

$$g(\eta_s) \; = \; -\frac{\partial \psi^h(\eta_s)}{\partial \eta_s} \quad = \quad \tau_0 + (\tau_\infty - \tau_0)\tanh\Big(\frac{h_0 \eta_s}{\tau_\infty - \tau_0} \Big). \tag{2.33}$$

A more general hardening rule that distinguish between *self-hardening* which char-
acterizes hardening on a slip plane due to slip on all slip systems coplanar to the
given plane; and *latent hardening* which refers to hardening on a slip plane due to
slip on all other individual slip planes can be found in Gurtin et al. (2007).

Example of viscoplastic behavior: In order to extend the framework to support
rate-dependent materials, it can be introduced the viscoplastic form. An example
for a viscoplastic law is given by Hoff (1960) by first recall the flow law (2.29) of
plastic slip to the form

$$\dot{\gamma}_s \; = \; \text{sign}(\tau_s)\lambda_s, \tag{2.34}$$

then rewrite the yield condition (2.27) in the form

$$\Phi(\tau_s, g_s) \; = \; \frac{|\tau_s|}{\tau_0 - g_s} \quad \leq \quad 1. \tag{2.35}$$

The Norton-Hoff viscoplastic regularization of the flow law is done by replacing
(2.34) with

$$\dot{\gamma}_s \; = \; \frac{\partial \tilde{f}}{\partial \tau_s}, \quad \text{where} \quad \tilde{f} \; = \; \frac{d_0}{q}\Phi^q, \tag{2.36}$$

where $q \geq 2$ and d_0 are positive constants.

2.2.2 Strain-gradient Single-crystal Plasticity

Strain-gradient theories of plasticity have got attention since the early contribution of Aifantis (1984). The benefit of these theories is the ability to introduce a length scale together with the non-local nature of the gradient terms that allow the theory to capture the size-dependence behavior observed in experiments and lacking from the classical theories of plasticity. Furthermore, the inclusion of gradients of plastic strain shades some light to a link at the continuum level between observed size effects and the underlying behavior of dislocations.

In this subsection, the extension of the classical theory of single-crystal plasticity to the gradient model will be presented in the way of the framework of Gurtin et al. (2007).

Characterization of Burgers vector in Gurtin framework: To derive the macroscopic counterpart of this notion, consider first the decomposition of the displacement gradient $\nabla \mathbf{u}$ into elastic and plastic parts $\boldsymbol{\beta}^{\text{el}}$ and $\boldsymbol{\beta}^{\text{pl}}$ as in (2.14) Now consider a closed curve $\mathcal{C}$ of the surface $\mathcal{F}$ in the body and because $\boldsymbol{\beta}^{\text{pl}}$ represents the distortion of the lattice due to the formation of dislocations, the corresponding integration around $\mathcal{C}$ in the distorted lattice is represented by the integral

$$\mathbf{b}(\mathcal{C}) \;=\; \int_{\mathcal{C}} \boldsymbol{\beta}^{\text{pl}} \mathbf{ds} \;=\; \int_{\mathcal{F}} (\nabla \times \boldsymbol{\beta}^{\text{pl}})^{\top} \mathbf{n} \mathrm{d}a. \tag{2.37}$$

Because $\boldsymbol{\beta}^{\text{pl}}$ is not generally the gradient of a vector field, the integral does not generally vanish. The vector $\mathbf{b}(\mathcal{C})$, which represents the Burgers vector corresponding to the curve $\mathcal{C}$, is a macroscopic analog of the Burgers vector as defined at the microscopic level.

The local consequence of this is basic to what follows. We associate the vector measure $(\nabla \times \boldsymbol{\beta}^{\text{pl}})^{\top} \mathbf{e} \mathrm{d}a$ with the Burgers vector corresponding to the boundary curve of the surface-element $\mathbf{n}\mathrm{d}a$. In this sense, the tensor field

$$\boldsymbol{\alpha} \;=\; \nabla \times \boldsymbol{\beta}^{\text{pl}} \tag{2.38}$$

which we refer to as the **Burgers tensor**, provides a local characterization of the Burgers vector.

Decomposition of Burgers tensor into edge and screw dislocations: We consider the reformulation of Burgers vector by using the single-crystal hypothesis that $\boldsymbol{\beta}^{\mathrm{pl}} = \sum_s \gamma_s \mathbf{d}_s \otimes \mathbf{m}_s$, which leads to

$$
\begin{aligned}
\boldsymbol{\alpha} &= \sum_s \nabla \times (\gamma_s \mathbf{d}_s \otimes \mathbf{m}_s) = \sum_s \nabla \times (\mathbf{d}_s \otimes (\gamma_s \mathbf{m}_s)) \\
&= \sum_s \Big([(\nabla \mathbf{d}_s)\gamma_s \mathbf{m}_s \times]^\top + \nabla \times (\gamma_s \mathbf{m}_s) \otimes \mathbf{d}_s\Big) \\
&= \sum_s \Big((\gamma_s \nabla \times \mathbf{m}_s + \nabla \gamma_s \times \mathbf{m}_s) \otimes \mathbf{d}_s\Big) = \sum_s (\nabla \gamma_s \times \mathbf{m}_s) \otimes \mathbf{d}_s.
\end{aligned}
$$

by using the fact that $\nabla \mathbf{d}_s = \nabla \times \mathbf{m}_s = \mathbf{0}$, then we have the useful identity that

$$
\boldsymbol{\alpha} = \sum_s (\nabla \gamma_s \times \mathbf{m}_s) \otimes \mathbf{d}_s. \tag{2.39}
$$

Let Π_s denote **slip plane** s. Then, for any s, the vector $\mathbf{d}_s$ and

$$
\mathbf{l}_s \quad := \quad \mathbf{m}_s \times \mathbf{d}_s \tag{2.40}
$$

form an orthonormal basis for Γ_s. Since the vector $\nabla \gamma_s \times \mathbf{m}_s$ is orthogonal to $\mathbf{m}_s$, it can be expanded in terms of $\mathbf{d}_s$ and $\mathbf{l}_s$,

$$
\begin{aligned}
\nabla \gamma_s \times \mathbf{m}_s &= [\mathbf{l}_s \cdot (\nabla \gamma_s \times \mathbf{m}_s)]\mathbf{l}_s + [\mathbf{d}_s \cdot (\nabla \gamma_s \times \mathbf{m}_s)]\mathbf{d}_s \\
&= [(\mathbf{m}_s \times \mathbf{l}_s) \cdot \nabla \gamma_s]\mathbf{l}_s + [(\mathbf{m}_s \times \mathbf{d}_s) \cdot \nabla \gamma_s]\mathbf{d}_s \\
&= (-\mathbf{d}_s \cdot \nabla \gamma_s)\mathbf{l}_s + (\mathbf{l}_s \cdot \nabla \gamma_s)\mathbf{d}_s
\end{aligned}
$$

hence we can write $\boldsymbol{\alpha}$ in the form

$$
\boldsymbol{\alpha} = \sum_s \Big[(\mathbf{l}^\alpha \cdot \nabla \gamma^\alpha)\mathbf{d}^\alpha \otimes \mathbf{d}^\alpha + (-\mathbf{d}^\alpha \cdot \nabla \gamma^\alpha)\mathbf{l}^\alpha \otimes \mathbf{d}^\alpha\Big]. \tag{2.41}
$$

Within a continuum theory the geometric features of edge and screw dislocations are characterized by dyads of the form $\mathbf{l}_s \otimes \mathbf{d}_s$, when $\mathbf{l}_s \perp \mathbf{d}_s$ represents edge dislocations and $\mathbf{d}_s \otimes \mathbf{d}_s$ when $\mathbf{l}_s = \mathbf{d}_s$ represents screw dislocations, where $\mathbf{l}_s$ and $\mathbf{d}_s$ are unit vectors. The normal vector $\mathbf{d}_s$ can be postulated as the **Burgers direction** and $\mathbf{l}_s$ as the **line direction**. The canonical dislocation dyads for slip on s are therefore the edge and screw dyads as follows

$$
\mathbf{l}_s \otimes \mathbf{d}_s (\text{edge}) \quad \text{and} \quad \mathbf{d}_s \otimes \mathbf{d}_s (\text{screw}) \tag{2.42}
$$

Introducing the symbols $\vdash$ and $\odot$ for edge and screw dislocations, we can thus rewrite $\boldsymbol{\alpha}$ in the form

$$\boldsymbol{\alpha} \;=\; \sum_s (\rho_\vdash^s \mathbf{l}_s \otimes \mathbf{d}_s + \rho_\odot^s \mathbf{d}_s \otimes \mathbf{d}_s), \tag{2.43}$$

$$\rho_\vdash^s \;:=\; -\mathbf{d}_s \cdot \nabla \gamma_s, \quad \rho_\odot^s := \mathbf{l}_s \cdot \nabla \gamma_s. \tag{2.44}$$

We refer to $\rho_\vdash^\alpha$ and $\rho_\odot^\alpha$ as **edge** and **screw dislocation densities**. Thus we see that $\boldsymbol{\alpha}$ can be decomposed into distributions of edge and screw dislocations on the individual slip systems.

Note that the densities $\rho_\vdash^\alpha$ and $\rho_\odot^\alpha$ carry units of $[m^{-1}]$ and that they may be positive or negative.

The tangential gradient ∇^s on the slip plane Γ_s: Recall that Γ_s represents the slip plane s. The tensor

$$\mathbf{P}^s \;=\; \mathbf{1}_3 - \mathbf{m}_s \otimes \mathbf{m}_s \tag{2.45}$$

represents the **projection** onto Γ_s. Since $\{\mathbf{m}_s, \mathbf{d}_s, \mathbf{l}_s\}$ represents an orthonormal basis of all vectors in $\mathbb{R}^3$ implies that

$$\mathbf{d}_s \otimes \mathbf{d}_s + \mathbf{l}_s \otimes \mathbf{l}_s + \mathbf{m}_s \otimes \mathbf{m}_s \;=\; \mathbf{1}_3, \tag{2.46}$$

and hence by definition of $\mathbf{P}^s$ that

$$\mathbf{P}^s \;=\; \mathbf{d}_s \otimes \mathbf{d}_s + \mathbf{l}_s \otimes \mathbf{l}_s. \tag{2.47}$$

Given any scalar field φ,

$$\nabla^s \varphi \;:=\; \mathbf{P}^s \nabla \varphi \tag{2.48}$$

is the tangential gradient of φ on Γ^s. We have

$$\nabla^s \varphi \;=\; (\mathbf{d}_s \cdot \nabla \varphi)\mathbf{d}_s + (\mathbf{l}_s \cdot \nabla \varphi)\mathbf{l}_s, \tag{2.49}$$

and we may conclude for γ_s that

$$\nabla^s \gamma_s \;=\; \mathbf{P}^\alpha \nabla \gamma_s \;=\; -\rho_\vdash^s \mathbf{d}_s + \rho_\odot^s \mathbf{l}_s, \tag{2.50}$$

the dislocation densities $\rho_\vdash^s$ and $\rho_\odot^s$ therefore represent components of the tangential slip gradient $\nabla^s \gamma_s$ relative to the basis $\{\mathbf{d}_s, \mathbf{l}_s\}$ for the slip plane Γ_s. The field

$$\rho_{\text{net}}^s \;:=\; \sqrt{|\rho_\vdash^s|^2 + |\rho_\odot^s|^2} \;=\; |\nabla^s \gamma_s|. \tag{2.51}$$

represent the **net dislocation density** on Γ_s.

Terminology: The terms Burgers vector and dislocation density in this subsection are different from these terms used by material scientists as also has been mentioned by Gurtin et al. (2010). The term Burgers vector in this context in **continuum mechanics** signifies a vector of a given length, measured per unit area, and the notion of a dislocation density also represents a length measured per area, this in continuum mechanics both carry the dimension $[m^{-1}]$. In **materials science** the Burgers vector comes from the physical movement of a dislocation line and is the vector that represents the closure failure of a Burgers circuit around a single dislocation in a crystal lattice; its magnitude, denoted by b, is also referred to as the Burgers length, a definition that typically renders b and interatomic spacing. In materials science dislocation densities are measured in dislocations per unit area and hence carry the dimension $[m^{-2}]$. Each continuum-mechanical density, say ρ_{cm}, can be converted to a material-science density, say ρ_{ms}, via the transformation

$$\rho_{\mathrm{ms}} \;=\; b^{-1}\rho_{\mathrm{cm}}. \tag{2.52}$$

Concrete example can be found in Orowan equation, $\dot{\gamma}_s = \rho_{\mathrm{ms}}bv$, in this context refers to number of dislocations per unit area.

Furthermore, problems can also occur with plastic slip γ, since in physical meaning of material science the damage can be in all 0,1,2 and 3 dimension depended on problem setting as mentioned before but in continuum mechanics this quantity is considered only in volume. One has to be aware when combine this two perspective together.

Principle of virtual power and microforce balance

We come back to consider the kinematic quantities appearing in gradient theory for single crystal which in the work of Gurtin are the elastic strain rate $\dot{\boldsymbol{\varepsilon}}^{\mathrm{el}}$, the slip rates $\dot{\gamma}_s$, and their gradients $\nabla\dot{\gamma}_s$ that we have seen can be reformulated to the edge $\rho_\vdash^s$ and the screw $\rho_\odot^s$ dislocation densities later. The relevant stress-like quantities are then the stress $\boldsymbol{\sigma}$, a new scalar microforce π_s and a new vectorial microstress $\boldsymbol{\xi}_s$. Then the total internal power $P_{\mathrm{int}}(B)$ in the arbitrary sub-domain B in the body $\mathcal{B}$ is given by

$$P_{\mathrm{int}}(B) \;=\; \int_B \boldsymbol{\sigma} : \dot{\boldsymbol{\varepsilon}}^{\mathrm{el}}\mathrm{d}x + \sum_s \int_B (\pi_s\dot{\gamma}_s + \boldsymbol{\xi}_s \cdot \nabla\dot{\gamma}_s)\,\mathrm{d}x. \tag{2.53}$$

The external power $P_{\text{ext}}(B)$ has also the new term that involves a microtraction $\Xi_s(\mathbf{n})$ depending on the outward unit normal $\mathbf{n}$ and power-conjugate to $\dot{\gamma}_s$,

$$P_{\text{ext}}(B) \;=\; \int_B \mathbf{f} \cdot \dot{\mathbf{u}} \, \mathrm{d}x + \int_{\partial B} \mathbf{t} \cdot \dot{\mathbf{u}} \, \mathrm{d}s + \sum_s \int_{\partial B} \Xi_s(\mathbf{n}) \dot{\gamma}_s \, \mathrm{d}s. \tag{2.54}$$

From the decomposition of the gradient of dislocation (2.14) , we have a relation between the velocity $\dot{\mathbf{u}}$ and slip rate $\dot{\gamma}_s$ of the form,

$$\nabla \dot{\mathbf{u}} \;=\; \dot{\boldsymbol{\beta}}^{\text{el}} + \sum_s \dot{\gamma}_s M_s, \tag{2.55}$$

where $M_s = \mathbf{d}_s \otimes \mathbf{m}_s$ is the Schmidt tensor. The principle of virtual power is then simply the requirement that

$$P_{\text{int}}(B) \;=\; P_{\text{ext}}(B) \tag{2.56}$$

for all sub-domain B of $\mathcal{B}$ and all admissible kinematic rate quantities.

Next substitute (2.53) and (2.54) into the virtual power identity and set the velocity $\dot{\mathbf{u}} = \mathbf{0}$ then the following identity is obtained,

$$\sum_s \left[\int_B (\pi_s - \tau_s - \mathrm{div}\,\boldsymbol{\xi}_s) \dot{\gamma}_s \, \mathrm{d}x + \int_{\partial B} (\boldsymbol{\xi}_s \cdot \mathbf{n} - \Xi_s(\mathbf{n})) \dot{\gamma}_s \, \mathrm{d}s \right] \;=\; 0 \tag{2.57}$$

by using the integration by parts

$$\int_B \boldsymbol{\xi}_s \cdot \nabla \dot{\gamma}_s \, \mathrm{d}x \;=\; \int_{\partial B} \boldsymbol{\xi} \cdot \mathbf{n} \dot{\gamma}_s \, \mathrm{d}s - \int_B \mathrm{div}\,\boldsymbol{\xi}_s \dot{\gamma}_s \, \mathrm{d}x, \tag{2.58}$$

the relation between elastic rate $\dot{\boldsymbol{\varepsilon}}^{\text{el}}$ and slip rate $\dot{\gamma}_s$ from (2.55) for $\dot{\mathbf{u}} = \mathbf{0}$ such that

$$\dot{\boldsymbol{\varepsilon}}^{\text{el}} \;=\; \mathrm{sym}\,\dot{\boldsymbol{\beta}}^{\text{el}} \;=\; -\sum_s \dot{\gamma}_s \, \mathrm{sym}\,M_s, \tag{2.59}$$

and using symmetry property of $\boldsymbol{\sigma}$ for shear stress $\tau_s = \boldsymbol{\sigma} : M_s$.

Since B is arbitrary, then the following microforce balance equation is obtained

$$\tau_s \;=\; \pi_s - \mathrm{div}\,\boldsymbol{\xi}_s \tag{2.60}$$

and furthermore the microtraction condition on the boundary

$$\Xi_s(\mathbf{n}) \;=\; \boldsymbol{\xi}_s \cdot \mathbf{n}. \tag{2.61}$$

Free energy function, dissipation inequality and length scale

The free energy in the case of single-crystal strain-gradient plasticity is written in the separable form with the addition of defect energy ψ^d that depends on dislocation densities of edges $\boldsymbol{\rho}_\vdash = (\rho_\vdash^1, ..., \rho_\vdash^N)$ and screws $\boldsymbol{\rho}_\odot = (\rho_\odot^1, ..., \rho_\odot^N)$,

$$\psi(\boldsymbol{\varepsilon}^{\text{el}}, \boldsymbol{\rho}_\vdash, \boldsymbol{\rho}_\odot, \boldsymbol{\eta}) \;=\; \psi^{\text{el}}(\boldsymbol{\varepsilon}^{\text{el}}) + \psi^d(\boldsymbol{\rho}_\vdash, \boldsymbol{\rho}_\odot) + \psi^h(\boldsymbol{\eta}). \tag{2.62}$$

The local dissipation inequality takes the form

$$\dot{\psi} - \boldsymbol{\sigma} : \dot{\varepsilon}^{\text{el}} - \sum_s (\pi_s \dot{\gamma}_s + \boldsymbol{\xi}_s \cdot \nabla \dot{\gamma}_s) \;\leq\; 0. \tag{2.63}$$

The defect energies based on dislocation densities in Gurtin et al. (2007) work takes the form

$$\begin{aligned}
\psi^d(\boldsymbol{\rho}_\vdash, \boldsymbol{\rho}_\odot) &\;=\; \frac{1}{2} \sum_s |\rho_{\text{net}}^s|^2 \;=\; \frac{1}{2} \sum_s \left((\rho_\vdash^s)^2 + (\rho_\odot^s)^2 \right) \\
&\;=\; \frac{1}{2} \sum_s |\nabla^s \gamma_s|^2,
\end{aligned}$$

where $\nabla^s \gamma_s := (\mathbf{d}_s \cdot \nabla \gamma_s)\mathbf{d}_s + (\mathbf{l}_s \cdot \nabla \gamma_s)\mathbf{l}_s = -\rho_\vdash^s \mathbf{d}_s + \rho_\odot^s \mathbf{l}_s$ as in (2.49).

Remark: Gurtin (2002) has also proposed another form of defect energy that depends on the Burgers tensor $\boldsymbol{\alpha}$ instead of dislocation densities,

$$\psi^d(\boldsymbol{\alpha}) \;=\; \frac{1}{2}|\boldsymbol{\alpha}|^2. \tag{2.64}$$

Then with the substitution of the free energy the dissipation inequality reduced to

$$\sum_s \left((\boldsymbol{\xi}_s - \boldsymbol{\xi}_s^{\text{en}}) \cdot \nabla \dot{\gamma}_s + \pi_s \dot{\gamma}_s + g_s \dot{\eta}_s \right) \;\geq\; 0, \tag{2.65}$$

by using the fact that $\dot{\psi}^d = \sum_s \boldsymbol{\xi}_s^{\text{en}} \cdot \nabla \dot{\gamma}_s$ with

$$\boldsymbol{\xi}_s^{\text{en}} \;:=\; \frac{\partial \psi^d}{\partial(\nabla \gamma)} \;=\; -\rho_\vdash^s \mathbf{d}_s + \rho_\odot^s \mathbf{l}_s. \tag{2.66}$$

that represents the energetic component of the microstress.

For simplicity we define the dissipative microstress

$$\boldsymbol{\xi}_s^{\text{dis}} \;:=\; \boldsymbol{\xi}_s - \boldsymbol{\xi}_s^{\text{en}} \tag{2.67}$$

and introducing the generalized stress Σ_s and the generalized plastic strain P_s as same as in previous setting by

$$\Sigma_s := (\pi_s, \ell_e^{-1}\boldsymbol{\xi}_s^{\text{dis}}, g_s), \quad P_s := (\gamma_s, \ell_e\nabla\gamma_s, \eta_s), \tag{2.68}$$

where ℓ_e is an energetic length scale that evolved the size dependent behavior then the dissipation inequality can be rewritten in the compact form

$$\sum_s \Sigma_s \cdot \dot{P}_s \geq 0. \tag{2.69}$$

The yield function on the slip s is defined by

$$\phi(\Sigma_s) := |S_s^{\text{dis}}|_2 + g_s - S_0, \tag{2.70}$$

here S_0 denotes the initial yield stress, $S_s^{\text{dis}} = (\pi_s, \ell_e^{-1}\boldsymbol{\xi}_s)$ and $|S_s^{\text{dis}}|_2 := (|\pi_s|^2 + \ell_e^{-2}|\boldsymbol{\xi}_s^{\text{dis}}|^2)^{1/2}$.

The generalized strain rate and hardening rate are given by the normality relation

$$\dot{\gamma}_s = \lambda_s\frac{\partial\phi}{\partial\pi_s} = \lambda_s\frac{\pi_s}{|S_s^{\text{dis}}|_2}, \tag{2.71}$$

$$\nabla\dot{\gamma}_s = \lambda_s\frac{\partial\phi}{\partial\boldsymbol{\xi}_s^{\text{dis}}} = \lambda_s\frac{\ell_e^{-2}\xi_s^{\text{dis}}}{|S_s^{\text{dis}}|_2}, \tag{2.72}$$

$$\dot{\eta}_s = \lambda_s\frac{\partial\phi}{\partial g_s} = \lambda_s, \tag{2.73}$$

where $\lambda_s \geq 0$ is a scalar multiplier, together with the complementarity conditions

$$\phi(\Sigma_s) \leq 0, \quad \lambda_s \geq 0, \quad \lambda_s\phi(\Sigma_s) = 0. \tag{2.74}$$

Moreover, if we take the additional assumption for the normality relation of the pairs of strain rate

$$(\dot{\gamma}_s, \ell_e\nabla\dot{\gamma}_s) = \lambda_s\frac{\partial\phi}{\partial(\pi_s, \ell_e^{-1}\boldsymbol{\xi}_s)} = \lambda_s\frac{\partial\phi}{\partial S_s^{\text{dis}}} \tag{2.75}$$

then it follows

$$\lambda_s = \left((\dot{\gamma}_s)^2 + \ell_e^2|\nabla\dot{\lambda}_s|^2\right)^{1/2} =: d_s. \tag{2.76}$$

Here d_s can be viewed as the effective slip rate associated to the s slip system, then consider the flow at the yield surface such that $\phi = 0$, one gets $|S_s^{\text{dis}}|_2 = S_0 - g_s$ and the flow relations can be inverted, for $d \neq 0$, as

$$\pi_s = \frac{S_0 - g_s}{d_s} \dot{\gamma}_s, \tag{2.77}$$

$$\boldsymbol{\xi}_s^{\text{dis}} = \frac{S_0 - g_s}{d_s} \ell_e^2 \nabla \dot{\gamma}_s. \tag{2.78}$$

2.3 Higher-dimensional Continuum Dislocations Dynamics Theory

Only recently, Hochrainer and co-workers generalized the statistical approach of Groma towards systems of dislocations with arbitrary line orientation and line curvature introducing the higher-dimensional *Continuum Dislocation Dynamics* (hdCDD) theory Hochrainer (2006); Hochrainer et al. (2007); Sandfeld (2010a); Sandfeld et al. (2010). The key idea of hdCDD is based on mapping spatial, parameterized dislocation lines into a higher-dimensional configuration space, which contains the local line orientation as additional information. The continuum representation of lines in this configuration space requires the notion of a so-called generalized line direction **L** and generalized velocity **V** together with the dislocation density tensor of second order, $\boldsymbol{\alpha}^{\mathbb{II}}$, which is also defined in the configuration space. This density tensor contains the Kröner-Nye tensor as a special case but is furthermore able to describe the evolution of very general systems of curved dislocations with arbitrary orientation. In particular the common differentiation between GND and SSD density becomes dispensable. Similar to Kröner's or Groma's frameworks, this continuum theory again also describes only the kinematics, i.e. the evolution of dislocation density in a *given* velocity field. The additionally available information of hdCDD, e.g. line orientation and curvature, however, is crucial for determining dislocation interaction stresses and modeling physically-based boundary conditions in a realistic manner.

A complete dislocation based plasticity theory that based on hdCDD was however not yet firmly developed because the aim of the development of the theory was only trying to establish the mathematical framework needed to perform meaningful averages over systems of moving curved dislocations. The first attempt to investigate the full hdCDD based plasticity was proposed by Sandfeld et al. (2010). They considered the problem of micro-bending of a free-standing thin film by assuming the homogeneity of dislocation glides in the direction parallel to the film that can simplify the system to use only one representative slip plane per slip system for the simulation. This setting was limited to the given external stress and mean field stress that was derived explicitly in Zaiser et al. (2007); Nikitas (2008). To overcome the

limitation of homogeneous slip planes assumption, the relaxed system with discrete slip planes was introduced in Sandfeld et al. (2013) by using the Groma's continuum dislocations system and for a better explanation for dislocation loops in the recent work Sandfeld and Po (2015). For the system with hdCDD theory with discrete slip planes has not been studied before, therfore we propose here the framework to support the discrete slip planes. More details of the behaviour of hdCDD over a single slip, one can find in Chapter 4.

2.3.1 Dislocation Densities and Plastic Shear Strain

One aspect of continuum dislocation theories is that they consider averages of slip planes. Therefore, in any slip system s, we use a discrete set of 'crystallographic' slip planes of distance $\triangle s > 0$

$$\Gamma_{s,g} = \left\{ \mathbf{z}_g + \xi \mathbf{d}_s + \eta \mathbf{d}_s \times \mathbf{m}_s \colon (\xi, \eta) \in \mathbb{R}^2 \right\}, \tag{2.79}$$

where $\mathbf{z}_g \in \Gamma_{s,g}$ denotes the origin of the local (ξ, η) coordinate system which is aligned such that the Burgers vector $\mathbf{b}_s$ points into positive η direction and ξ points into the line direction of a positive edge dislocation; points in the slip plane are denoted by $\mathbf{r} \in \Gamma_{s,g}$. Each SP is expanded to a thin layer of width $h \leq \triangle s$ (collecting a small number of physical slip planes)

$$\mathcal{B}_{s,g} = \left\{ \mathbf{z} \in \mathcal{B} \colon \mathbf{z} = \mathbf{r}_g + \zeta \mathbf{m}_s \text{ with } \mathbf{r}_g \in \Gamma_{s,g} \text{ and } |\zeta| \leq h/2 \right\}. \tag{2.80}$$

In our model, the dislocation density in the slip system s is represented by the average $\rho_{s,g}$ in the layer $\mathcal{B}_{s,g}$.

Since the evolution of the dislocation density $\rho_{s,g}$ and Orowan's relation of the plastic shear strain are evaluated only in the crystallographic slip planes $\Gamma_{s,g}$, the continuum approach requires to extend the values to the body $\mathcal{B}$. For this purpose, we introduce the orthogonal projection $P_{s,g} \colon \mathcal{B} \longrightarrow \Gamma_{s,g}$, and for $\mathbf{r} \in \Gamma_{s,g} \backslash \mathcal{B}$ the plastic shear strain $\gamma_{s,g}$ is extended by constant continuation. We consider two cases:

Case 1: Direct representation of crystallographic SPs.
    We set

$$\gamma_s(\mathbf{r}) = \begin{cases} \gamma_{s,g}(\mathbf{r}) & \mathbf{r} \in \mathcal{B}_{s,g} \text{ for some } g, \\ 0 & \text{else}. \end{cases} \tag{2.81}$$

    The objective of Case 1 is, to analyze, how $\triangle s$ and h need to be chosen for our density-based micro-structure representation. This provides then benchmark data for Case 2.

Observation
surface slip traces
of a deformed crystal
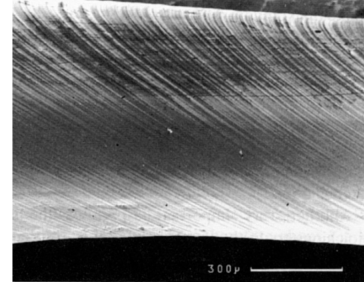
Physical model
the 'crystallographic'
slip planes (representing a small
number of physical slip planes)
are evenly spaced
with distance $\triangle s$
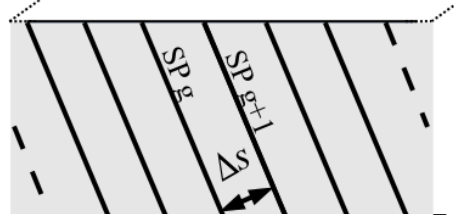
Numerical model
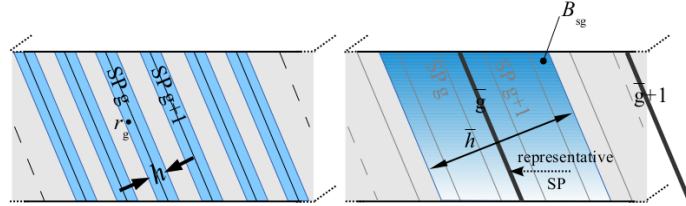
Case 1: direct representation   Case 2: averaged representation

Figure 2.7: The representation of discrete slip planes in one slip system in a crystal.

Case 2: Averaged representation of crystallographic SPs.

Alternatively, we average over multiple crystallographical SPs in order to arrive at a representation of, e.g., dislocation density or plastic strain in which they are distributed field quantities – not only within the SP but also in direction of the slip system normal. Therefore, we first collapse a number of crystallographic SPs that are contained within a region of width $\triangle \bar{s} \gg h$ into one *representative* SP by summing up the respective dislocation field variables over $\triangle \bar{s}$. The representative SPs are numbered by $\bar{g}$. All points $\mathbf{r}$ of this layer belong to the domain

$$\overline{\mathcal{B}}_{s,\overline{g}} = \left\{ \mathbf{z} \in \mathcal{B} \colon \mathbf{z} = \mathbf{r}_{\overline{g}} + \zeta \mathbf{m}_s \text{ with } \mathbf{r}_{\overline{g}} \in \Gamma_{s,\overline{g}} \text{ and } |\zeta| \leq \triangle \overline{s}/2 \right\} \qquad (2.82)$$

averaging over representative slip planes. The domains $\overline{\mathcal{B}}_{s,\overline{g}}$ are non-overlapping with $\bigcup_{\overline{g}} \overline{\mathcal{B}}_{s,\overline{g}} = \mathcal{B}$. For the plastic shear strain in $\overline{\mathcal{B}}_{s,\overline{g}}$ we define the average

$$\overline{\gamma}_{s,\overline{g}} = \frac{\triangle s}{\triangle \overline{s}} \sum_{\Gamma_{s,g} \subset \overline{\mathcal{B}}_{s,\overline{g}}} \gamma_{s,g} \,. \qquad (2.83)$$

At points between the representative slip planes

$$\mathbf{r} = \frac{\triangle \overline{s} - \zeta}{\triangle \overline{s}} P_{s,\overline{g}}\mathbf{r} + \frac{\zeta}{\triangle \overline{s}} P_{s,\overline{g}+1}\mathbf{r}\,, \qquad \zeta \in [0, \triangle s]$$

we define the plastic shear strain in the body $\mathcal{B}$ by linear interpolation

$$\gamma_s(\mathbf{r}) = \frac{\triangle \overline{s} - \zeta}{\triangle \overline{s}} \overline{\gamma}_{s,\overline{g}}(P_{s,\overline{g}}\mathbf{r}) + \frac{\zeta}{\triangle \overline{s}} \overline{\gamma}_{s,\overline{g}+1}(P_{s,\overline{g}+1}\mathbf{r})\,. \tag{2.84}$$

2.3.2 A hdCDD theory of Curved Dislocations

The tensor $\boldsymbol{\alpha}^{\mathbb{II}}$ is defined on the configuration space $\Gamma_{s,g} \times S^1$, where $S^1 = \mathbb{R}/2\pi \equiv [0, 2\pi)$ is the orientation space. In the following, $\mathbf{r} = (\eta, \xi)$ is a point in the slip plane and $(\mathbf{r}, \varphi)$ denotes a point in $\Gamma_{s,g} \times S^1$. The dislocation density on $\Gamma_{s,g}$ must be understood as a volume density. If we want to obtain the total line length in the SP, we have to integrate $\rho_{s,g}^{\mathcal{B}}$ over $\mathcal{B}_{s,g}$.

Let $\mathbf{l}_s(\varphi) = \cos\varphi\,\mathbf{d}_s + \sin\varphi\,\mathbf{d}_s \times \mathbf{m}_s$ define the canonical spatial line direction and $\mathbf{L}_{s,g}(\mathbf{r}, \varphi) = (\mathbf{l}_s, k_{s,g})^\top$ define the generalized line direction in the higher-order configuration space, with $k_{s,g}$ the average line curvature (i.e. one over the bending radius of the line). The dislocation density tensor of second order then takes the form

$$\boldsymbol{\alpha}_{s,g}^{\mathbb{II}}(\mathbf{r}, \varphi) = \rho_{s,g}(\mathbf{r}, \varphi)\mathbf{L}_{s,g}(\mathbf{r}, \varphi) \otimes \mathbf{b}_s\,, \tag{2.85}$$

where we again assume that the slip plane coordinate system $\eta - \xi$ is aligned such, that the Burgers vector $\mathbf{b}_s$ points into positive η direction. The evolution equation for this tensor has the form

$$\partial_t \boldsymbol{\alpha}_{s,g}^{\mathbb{II}}(\mathbf{r}, \varphi) = -\hat{\nabla} \times \left(\mathbf{V}_{s,g}(\mathbf{r}, \varphi) \times \boldsymbol{\alpha}_{s,g}^{\mathbb{II}}(\mathbf{r}, \varphi) \right)\,, \tag{2.86}$$

where the vector $\mathbf{V}_{s,g} = (-v_{s,g}\partial_\varphi\mathbf{l}_s, -\mathbf{L}_{s,g} \cdot \hat{\nabla}v_{s,g})$ denotes the generalized velocity in configuration space, which is perpendicular to the generalized line direction and $\hat{\nabla} := (\partial_\eta, \partial_\xi, \partial_\varphi)$. For detailed information on derivations and implications of these equations refer to Hochrainer et al. (2007); Sandfeld et al. (2010). One can observe that from a formal point of view the Kröner-Nye framework with equations (2.4) and (2.6) looks very similar to the higher-dimensional Hochrainer framework with equations (2.85) and (2.86) if $\mathbf{l}_s$ and $\mathbf{v}_s$ were exchanged with their higher-dimensional counterparts. In fact, one can retrieve the Kröner-Nye tensor for the slip plane s from the density function $\rho_{s,g}(\mathbf{r}, \varphi)$ in a straightforward manner as

$$\boldsymbol{\alpha}_{s,g}(\mathbf{r}) = \int_0^{2\pi} \rho_{s,g}(\mathbf{r}, \varphi)\mathbf{l}_s(\varphi) \otimes \mathbf{b}_s\,\mathrm{d}\varphi\,, \quad \mathbf{l}_s(\varphi) = \cos\varphi\,\mathbf{d}_s + \sin\varphi\,\mathbf{d}_s \times \mathbf{m}_s\,.$$

Other classical measures can be derived from hdCDD variables as well. For instance the total scalar density is given by

$$\rho_{s,g}^{\text{tot}}(\mathbf{r}) \;=\; \int_0^{2\pi} \rho_{s,g}(\mathbf{r}, \varphi)\, \mathrm{d}\varphi\,, \tag{2.87}$$

and the two GND densities contained in the components $(\boldsymbol{\alpha}_{s,g})_{11}$ and $(\boldsymbol{\alpha}_{s,g})_{12}$ (e.g. the GND density of edge and screw dislocations) derive as

$$\boldsymbol{\kappa}_{s,g}(\mathbf{r}) = \int_0^{2\pi} \rho_{s,g}(\mathbf{r}, \varphi)\mathbf{l}_s(\varphi)\, \mathrm{d}\varphi\,, \qquad \boldsymbol{\kappa}_{s,g}^{\perp}(\mathbf{r}) = \int_0^{2\pi} \rho_{s,g}(\mathbf{r}, \varphi)\mathbf{l}_s'(\varphi)\, \mathrm{d}\varphi\,, \tag{2.88}$$

where $\mathbf{l}_s'(\varphi) = -\sin\varphi\, \mathbf{d}_s + \cos\varphi\, \mathbf{d}_s \times \mathbf{m}_s$ is the orthogonal line direction. Subsequently, we will not state the point of evaluation $(\mathbf{r})$ or $(\mathbf{r}, \varphi)$ for ease of readability if the meaning is clear from the context. The physical interpretation of the tensorial evolution equation (2.86) might become more obvious if one replaces the evolution equation for $\boldsymbol{\alpha}_{s,g}^{\mathrm{II}}$ by a system of two coupled scalar evolution equations for the dislocation density $\rho_{s,g}$ and the so-called curvature density $q_{s,g} = \rho_{s,g}k_{s,g}$:

$$\partial_t \rho_{s,g} \;=\; -\hat{\nabla} \cdot (\rho_{s,g}\mathbf{V}_{s,g}) + q_{s,g}v_{s,g}\,, \tag{2.89a}$$

$$\partial_t q_{s,g} \;=\; -\hat{\nabla} \cdot (q_{s,g}\mathbf{V}_{s,g}) - \rho_{s,g}\Big(\mathbf{L}_{s,g} \cdot \hat{\nabla}(\mathbf{L}_{s,g} \cdot \hat{\nabla}v_{s,g})\Big)\,. \tag{2.89b}$$

The first of these two equations gives upon integration over the sub-volume $\mathcal{B}_{s,g}$ and all orientations S the total line length in the respective sub-volume, whereas integrating the second equation over $\mathcal{B}_{s,g}$ and S yields the number of closed dislocation loops as multiple of 2π. This set of equations is complemented by boundary conditions which define, whether a dislocation can leave the crystal (free surface) or not (impenetrable surface). In the latter case, the density flux through the boundary is set to zero, e.g. $\rho_{s,g}\mathbf{v}_{s,g} \cdot \mathbf{n}_s = 0$, where $\mathbf{n}_s$ is the outward unit normal at the boundary point under consideration.

The plastic shear strain $\gamma_{s,g}$ can be obtained similar as before by using the Orowan relation and integrating over the orientation space:

$$\partial_t \gamma_s \;=\; b_{s,g} \int_0^{2\pi} \rho_{s,g}v_{s,g}\mathrm{d}\varphi\,. \tag{2.90}$$

2.3.3 The Dislocation Velocity

All continuum dislocation models mentioned in the previous section have in common that they are 'kinematic' theories in the sense that all of them take the dislocation

velocity $v_{s,g}$ as a constitutive ingredient, based on which one then predicts the flux of density. Hence, in Kröner's, Groma's and Hochrainer's theories alike (although based on very different assumptions) the 'dynamics', i.e. stresses from dislocation interactions are *not* a priori included in these theories and need to be determined separately. How to derive physically meaningful dislocation interaction stress components is a topic that we will not further elaborate here; details about rigorous analysis of some dislocation systems in a continuum framework can be found in Zaiser et al. (2001); Groma et al. (2003); Sandfeld et al. (2013); Schulz et al. (2014). Subsequently, we base the dynamics of our dislocation systems on the following assumptions for the velocity function:

1. The scalar velocity $v_{s,g}$ in $\Gamma_{s,g}$ is assumed to depend linearly on the stresses acting on dislocations.

2. The velocity function can be decomposed into several types of stresses that can be sorted into two fundamentally different classes: those stresses obtained from the solution of the elastic BVP as outlined in section 5.1.1 together with the projection of the resolved stress, $\tau_{s,g} = \mathbf{M}_s : \boldsymbol{\sigma}$ and those stresses governing short-range elastic dislocation interactions, $\tau_{s,g}^{\mathrm{b}}$, $\tau_{s,g}^{\mathrm{lt}}$ and $\tau_{s,g}^{\mathrm{y}}$, which are the back stress, line tension and yield stress, respectively.

3. We assume that dislocations move only if the yield stress was overcome by the sum of all other contributions which we denote by $\tau^0 = \tau_{s,g} - \tau_{s,g}^{\mathrm{b}} - \tau_{s,g}^{\mathrm{lt}}$. The signs follows from the definitions of the stresses stated below.

With these assumptions the velocity function then takes the form

$$v_{s,g} = \begin{cases} \frac{b_s}{B} \operatorname{sgn}(\tau_{s,g}^0)(|\tau_{s,g}^0| - \tau_{s,g}^{\mathrm{y}}) & \text{if } |\tau_{s,g}^0| > \tau_{s,g}^{\mathrm{y}}, \\ \\ 0 & \text{otherwise,} \end{cases} \tag{2.91}$$

where B is the drag coefficient. The stress $\tau_{s,g}$ from the solution of the elastic BVP contains besides the stresses due to the prescribed boundary conditions also the contribution from the eigenstrain, which governs the long-range interaction between dislocations. For further details and a study of the elastic long range interaction refer to e.g. Sandfeld et al. (2013). The back stress is an approximation for the repelling forces between parallel dislocations with the same line direction. It is required due to the fact, that the resolution of the dislocation problem (the mesh width) is generally much higher than the resolution of the elastic BVP. For details see e.g. Groma et al. (2003); Sandfeld et al. (2011); Schulz et al. (2014). For a system of curved dislocations no back stress formulation has been benchmarked before. Hence,

we adapt a formulation which was suggested and implemented in the related works Hochrainer (2006); Sandfeld (2010a). The back stress then can be written as

$$\tau_{s,g}^{\mathrm{b}} = \frac{D\mu b_s}{\rho_{s,g}^{\mathrm{tot}}} \nabla \cdot \boldsymbol{\kappa}_{s,g}^{\perp} ,$$

which means, that the back stress at $\mathbf{r}$ in direction of $\mathbf{l}_s(\varphi)$ is proportional to the gradient of GNDs perpendicular to the line direction $\mathbf{l}_s$. Here, D is a constant taken to be of magnitude 1.

The line tension $\tau_{s,g}^{\mathrm{lt}}$ describes the self-interaction of a dislocation loop, e.g. a loop subjected to no other stress would contract due to the line tension. If we use a constant line tension approximation that is independent of the line orientation the line tension reads

$$\tau_{s,g}^{\mathrm{lt}} = \frac{T_s}{b_s} \frac{q_{s,g}}{\rho_{s,g}}$$

where T_s is the coefficient describing the strength of the interaction; it can be set to $T_s = \mu b_s^2$. Finally, the yield function is governed by a Taylor-type term for the form

$$\tau_{s,g}^{\mathrm{y}} = a\mu b_s \sqrt{\rho_{s,g}^{\mathrm{tot}}} \tag{2.92}$$

with a constant $a \in [0.2, 0.4]$, see Groma et al. (2003).

3 | Analysis and numerical approximation of the hdCDD system

The purpose of this chapter is to provide mathematical tools to analyze and to construct numerical methods for the system of equations (2.89) that come from the higher-dimensional Continuum Dislocation Dynamics theory. We first restate the problem here again and formulate definitions of the problem in a more precise mathematical setting. For the well-posedness result of the system, we follow the framework described in Ern et al. (2007) which is summarized in the Section 3.1 and 3.2. Then we finish the chapter with the investigation of one of the numerical methods used for hd-CDD system, i.e., the explicit Runge-Kutta Discontinuous Galerkin methods with third order in time by following the framework of Burman et al. (2010).

Consider the evolution equations for the dislocation density $\rho_{s,g}$ and the curvature density $q_{s,g}$

$$
\begin{aligned}
\partial_t \rho_{s,g} &= -\hat{\nabla} \cdot (\rho_{s,g} \mathbf{V}_{s,g}) + q_{s,g} v_{s,g} , & \text{(3.1a)} \\
\partial_t q_{s,g} &= -\hat{\nabla} \cdot (q_{s,g} \mathbf{V}_{s,g}) - \rho_{s,g} \left(\mathbf{L}_{s,g} \cdot \hat{\nabla}(\mathbf{L}_{s,g} \cdot \hat{\nabla} v_{s,g}) \right) , & \text{(3.1b)}
\end{aligned}
$$

with the general velocity $\mathbf{V}_{s,g}$ and the general line direction $\mathbf{L}_{s,g}$ in the higher-order configuration space given by

$$
\begin{aligned}
\mathbf{V}_{s,g}(\mathbf{r}, \varphi) &:= (-v_{s,g} \partial_\varphi \mathbf{l}_s, -\mathbf{L}_{s,g} \cdot \hat{\nabla} v_{s,g}), & \text{(3.2)} \\
\mathbf{L}_{s,g}(\mathbf{r}, \varphi) &:= (\mathbf{l}_s, k_{s,g})^\top, & \text{(3.3)}
\end{aligned}
$$

where $\mathbf{l}_s(\varphi) := (\cos\varphi, \sin\varphi)$ is the canonical spatial line direction and $k_{s,g}$ is the average line curvature with the constitutive relation

$$
q_{s,g} = \rho_{s,g} k_{s,g}. \tag{3.4}
$$

To make notations simpler, later in this chapter the slip system s and representative slip g indices will not be written since the system will be considered on a specific

single plane. In the setting of hdCDD in chapter 2, the given velocity v is assumed not to depend on the φ direction. With this assumption the evolution system can be reduced by first considering

$$
\begin{aligned}
\rho\Big(\mathbf{L} \cdot \hat{\nabla}(\mathbf{L} \cdot \hat{\nabla} v)\Big) &= \rho\Big((\mathbf{l}, k)^\top \cdot \hat{\nabla}\Big((\mathbf{l}, k)^\top \cdot (\nabla v, 0)^\top\Big)\Big) \\
&= \rho\Big((\mathbf{l}, k)^\top \cdot \hat{\nabla}(\mathbf{l} \cdot \nabla v)\Big) \\
&= \rho\Big(\mathbf{l} \cdot \nabla(\mathbf{l} \cdot \nabla v) + k\partial_\varphi(\mathbf{l} \cdot \nabla v)\Big) \\
&= \rho(\mathbf{l} \cdot \nabla(\mathbf{l} \cdot \nabla v)) + q(\mathbf{l}' \cdot \nabla v).
\end{aligned}
$$

Then the evolution system reduces to

$$
\begin{aligned}
\partial_t \rho &= -\hat{\nabla} \cdot (\rho \mathbf{V}) + qv, & \text{(3.5a)} \\
\partial_t q &= -\hat{\nabla} \cdot (q \mathbf{V}) - \rho(\mathbf{l} \cdot \nabla(\mathbf{l} \cdot \nabla v)) - q(\mathbf{l}' \cdot \nabla v). & \text{(3.5b)}
\end{aligned}
$$

To prepare this problem setting for a mathematical analysis, the system (3.5) is rewritten in a general form that later will be defined and called as the **Friedrich system**,

$$
\partial_t \mathbf{u} + \sum_{i=1}^{3} \partial_i(\mathbf{F}^i \mathbf{u}) + \mathbf{B}\mathbf{u} = \mathbf{0} \quad \text{in } \Omega \subset \mathbb{R}^2 \times S^1, \tag{3.6}
$$

where $(\partial_i)_{i=1,2,3} = (\partial_x, \partial_y, \partial_\varphi)^\top$, $\mathbf{u} = (\rho, q)^\top$ and

$$
\begin{aligned}
\mathbf{F}^1 &= \begin{bmatrix} v\sin\varphi & 0 \\ 0 & v\sin\varphi \end{bmatrix}, & \mathbf{F}^2 &= \begin{bmatrix} -v\cos\varphi & 0 \\ 0 & -v\cos\varphi \end{bmatrix}, \\
\mathbf{F}^3 &= \begin{bmatrix} -\mathbf{l} \cdot \nabla v & 0 \\ 0 & -\mathbf{l} \cdot \nabla v \end{bmatrix}, & \mathbf{B} &= \begin{bmatrix} 0 & -v \\ \mathbf{l} \cdot \nabla(\mathbf{l} \cdot \nabla v) & \mathbf{l}' \cdot \nabla v \end{bmatrix}.
\end{aligned}
$$

We can also rewrite (3.6) in an alternative form

$$
\partial_t \mathbf{u} + \sum_{i=1}^{3} \mathbf{F}^i \partial_i \mathbf{u} + \sum_{i=1}^{3} (\partial_i \mathbf{F}^i)\mathbf{u} + \mathbf{B}\mathbf{u} = \mathbf{0}. \tag{3.7}
$$

We define operators

$$
\mathbf{F} := \sum_{i=1}^{3} \mathbf{F}^i \partial_i, \quad \mathcal{X} := \sum_{i=1}^{3} \partial_i \mathbf{F}^i, \quad \widetilde{\mathbf{B}} := \mathcal{X} + \mathbf{B},
$$

i.e.

$$\mathcal{X} = \begin{bmatrix} -2\mathbf{l}' \cdot \nabla v & 0 \\ 0 & -2\mathbf{l}' \cdot \nabla v \end{bmatrix}, \quad \widetilde{\mathbf{B}} = \begin{bmatrix} 0 & -v \\ -2\mathbf{l}' \cdot \nabla v + \mathbf{l} \cdot \nabla (\mathbf{l} \cdot \nabla v) & -\mathbf{l}' \cdot \nabla v \end{bmatrix}.$$

Then we have

$$\partial_t \mathbf{u} + \mathbf{F}\mathbf{u} + \widetilde{\mathbf{B}}\mathbf{u} = \mathbf{0}. \tag{3.8}$$

3.1 Friedrichs' Operator

Let L be a Hilbert space equipped with the scalar product $(\cdot, \cdot)_L$ and the corresponding norm $\|\cdot\|_L$. Let $\mathcal{D}$ be a dense subspace of L. We assume that we have at hand two linear operators $\mathbf{T} : \mathcal{D} \to L$ and $\widetilde{\mathbf{T}} : \mathcal{D} \to L$.

Definition 3.1.1. (Friedrichs' operators) We say that $\mathbf{T}$ and $\widetilde{\mathbf{T}}$ are *Friedrichs' operators* if they are satisfied the following assumptions

$$\forall (u, v) \in \mathcal{D} \times \mathcal{D}, \qquad (\mathbf{T}u, v)_L = (u, \widetilde{\mathbf{T}}v)_L, \tag{T1}$$

$$\exists C \quad \text{s.t} \quad \forall u \in \mathcal{D}, \qquad \|(\mathbf{T} + \widetilde{\mathbf{T}})u\|_L \leq C\|u\|_L, \tag{T2}$$

$$\exists \mu_0 > 0 \quad \text{s.t} \quad \forall z \in L, \qquad ((\mathbf{T} + \widetilde{\mathbf{T}})z, z)_L \geq 2\mu_0 \|z\|_L^2. \tag{T3}$$

It cannot be seen immediately that this definition is well-defined because in (T3) it is not clear whether $\mathbf{T} + \widetilde{\mathbf{T}}$ can be extended to L. To show well-definedness of this definition, the following lemma is needed and in addition the self-adjoint property is shown for $\mathbf{T} + \widetilde{\mathbf{T}}$,

Lemma 3.1.2. Assume (T1) and (T2), then $\mathbf{T} + \widetilde{\mathbf{T}} \in \mathcal{L}(L; L)$ and is self-adjoint on L such that

$$\forall (u, v) \in L \times L, \qquad ((\mathbf{T} + \widetilde{\mathbf{T}})u, v)_L = (u, (\mathbf{T} + \widetilde{\mathbf{T}})v)_L. \tag{3.9}$$

Proof. $\mathbf{T} + \widetilde{\mathbf{T}} \in \mathcal{L}(L; L)$ is the consequence of the closure theorem [Kreyszig, Thm. 10.3-5] by using the density property of $\mathcal{D}$ and $\mathbf{T} + \widetilde{\mathbf{T}} \in \mathcal{L}(\mathcal{D}; L)$ from (T2). To prove the self-adjoint property, since $\mathcal{D}$ is dense in L then for any $u, v \in L$ there exist sequence in $\mathcal{D}$ such that $(u_n) \to u$ and $(v_n) \to v$. From (T1) we have

$$((\mathbf{T} + \widetilde{\mathbf{T}})u_n, v_n)_L = (u_n, (\mathbf{T} + \widetilde{\mathbf{T}})v_n)_L,$$

then letting $n \to \infty$ and using the property that $\mathbf{T} + \widetilde{\mathbf{T}} \in \mathcal{L}(L; L)$ shows that (3.9) is satisfied. $\square$

3.1.1 Examples

Friedrichs' System: Let Ω be a bounded, open, and connected Lipschitz domain in $\mathbb{R}^d$. Let m be a positive integer and set $L = [L^2(\Omega)]^m$ and $\mathcal{D} = [C_0^\infty(\Omega)]^m$. With this setting $\mathcal{D}$ is dense in L. A Friedrichs' system is formulated using $d+1$ $\mathbb{R}^{m,m}$-valued fields defined in the domain Ω, say $\mathbf{B}, \mathbf{F}^1, ..., \mathbf{F}^d$ with the assumptions that

$$\mathbf{B}, \mathbf{F}^i, \ i \in 1, ..., d \quad \text{and} \quad \sum_{i=1}^d \partial_i \mathbf{F}^i \in [L^\infty(\Omega)]^{m,m}, \tag{3.10a}$$

$$\mathbf{F}^i = (\mathbf{F}^i)^\top, \ i \in 1, ..., d \quad \text{a.e. in} \quad \Omega, \tag{3.10b}$$

$$\exists \mu_0 > 0, \quad \mathbf{B} + \mathbf{B}^\top - \sum_{k=1}^d \partial_i \mathbf{F}^i \geq \mu \mathbf{I}_m, \tag{3.10c}$$

where $\mathbf{I}_m$ denotes the identity matrix in $\mathbb{R}^{m,m}$. We define an operator $\mathbf{T}$ as follows:

$$\mathbf{T} : \mathcal{D} \to L, \ \mathbf{u} \mapsto \mathbf{B}\mathbf{u} + \sum_{i=1}^d \mathbf{F}^i \partial_i \mathbf{u}. \tag{3.11}$$

Then the formal adjoint of $\mathbf{T}$ is given by

$$\widetilde{\mathbf{T}} : \mathcal{D} \to L, \ \mathbf{u} \mapsto \left(\mathbf{B}^\top - \sum_{i=1}^d (\partial_i \mathbf{F}^i)\right)\mathbf{u} - \sum_{i=1}^d \mathbf{F}^i \partial_i \mathbf{u}. \tag{3.12}$$

Proposition 3.1.3. Assume (3.10), and let $\mathbf{T}$ and $\widetilde{\mathbf{T}}$ be defined by (3.11) and (3.12), respectively. Then $\mathbf{T}$ and $\widetilde{\mathbf{T}}$ are Friedrichs' operators.

Proof. We have to show that a Friedrichs' system satisfies properties (T1) – (T3).

T1: Let $\mathbf{u}, \mathbf{v} \in \mathcal{D}$, it follows that

$$
\begin{aligned}
(\mathbf{T}\mathbf{u}, \mathbf{v})_L &= (\mathbf{B}\mathbf{u} + \sum_{i=1}^d \mathbf{F}^i \partial_i \mathbf{u}, \mathbf{v})_L \\
&= (\mathbf{u}, \mathbf{B}^\top \mathbf{v}) + \sum_{i=1}^d (\partial_i(\mathbf{F}^i \mathbf{u}), \mathbf{v})_L - \sum_{i=1}^d ((\partial_i \mathbf{F}^i)\mathbf{u}, \mathbf{v})_L \\
&= (\mathbf{u}, \mathbf{B}^\top \mathbf{v}) - \sum_{i=1}^d (\mathbf{u}, (\partial_i \mathbf{F}^i)^\top \mathbf{v})_L \\
&\quad + \int_{\partial\Omega} \sum_{i=1}^d n_i(\mathbf{F}^i \mathbf{u}) \cdot \mathbf{v} \, da - \sum_{i=1}^d (\mathbf{u}, (\mathbf{F}^i)^\top \partial_i \mathbf{v})_L \\
&= (\mathbf{u}, \left(\mathbf{B}^\top - \sum_{i=1}^d (\partial_i \mathbf{F}^i) - \sum_{i=1}^d \mathbf{F}^i \partial_i\right) \mathbf{v})_L
\end{aligned}
$$

$$= (\mathbf{u}, \widetilde{\mathbf{T}}\mathbf{v})_L$$

by using integration by parts, the symmetry of $\mathbf{F}^i$ and $\mathbf{v} = \mathbf{0}$ on $\partial\Omega$.

T2: Observe that for $\mathbf{u} \in \mathcal{D}$,

$$(\mathbf{T} + \widetilde{\mathbf{T}})\mathbf{u} = \left(\mathbf{B} + \sum_{i=1}^{d} \mathbf{F}^i \partial_i + \mathbf{B}^\top - \sum_{i=1}^{d}(\partial_i \mathbf{F}^i) - \sum_{i=1}^{d} \mathbf{F}^i \partial_i\right)\mathbf{u}$$

$$= \left(\mathbf{B} + \mathbf{B}^\top - \sum_{i=1}^{d}(\partial_i \mathbf{F}^i)\right)\mathbf{u}.$$

Then

$$\|(\mathbf{T} + \widetilde{\mathbf{T}})\mathbf{u}\|_L^2 = \int_\Omega \left|\left(\mathbf{B} + \mathbf{B}^\top - \sum_{i=1}^{d}(\partial_i \mathbf{F}^i)\right)\mathbf{u}\right|^2 \mathrm{d}x$$

$$\leq \left(2\|\mathbf{B}\|_\infty^2 + \|\sum_{i=1}^{d}(\partial_i \mathbf{F}^i)\|_\infty^2\right) \int_\Omega |\mathbf{u}|^2 \, \mathrm{d}x$$

$$\leq C\|\mathbf{u}\|_L^2$$

since $\mathbf{B}$ and $\sum_{i=1}^{d}(\partial_i \mathbf{F}^i) \in [L_\infty(\Omega)]^{m,m}$.

T3: It follows from (3.10c) that

$$((\mathbf{T} + \widetilde{\mathbf{T}})\mathbf{u}, \mathbf{u})_L = \int_\Omega \left(\mathbf{B} + \mathbf{B}^\top - \sum_{k=1}^{d} \partial_i \mathbf{F}^i\right)\mathbf{u} \cdot \mathbf{u} \, \mathrm{d}x$$

$$\geq \mu \int_\Omega \mathbf{u} \cdot \mathbf{u} \, \mathrm{d}x = \mu\|\mathbf{u}\|_L^2.$$

$\square$

Symmetric First-Order Hyperbolic Systems: This class of systems can be transformed into Friedrichs' systems most directly. Consider the Friedrichs operator

$$\mathbf{T} : \mathbf{u} \mapsto \mathbf{B}\mathbf{u} + \sum_{i=1}^{d} \mathbf{F}^i \partial_i \mathbf{u}.$$

We call $\mathbf{T}$ *uniformly hyperbolic* on the domain Ω if there is a vector $\boldsymbol{\alpha} := (\alpha_1, ..., \alpha_m) \in \mathbb{R}^m$ such that $\sum_{i=1}^{d} \alpha_i \mathbf{F}^i$ is uniformly positive definite in $\overline{\Omega}$. Given $\beta \in \mathbb{R}$, the differential operator satisfied the identity

$$\mathbf{T}(\mathrm{e}^{\beta\boldsymbol{\alpha}\cdot\mathbf{x}}\mathbf{u}) = \mathbf{B}\mathrm{e}^{\beta\boldsymbol{\alpha}\cdot\mathbf{x}}\mathbf{u} + \sum_{i=1}^{d} \mathbf{F}^i \partial_i \mathbf{u} + \sum_{i=1}^{d}(\mathbf{F}^i \partial_i \mathrm{e}^{\beta\boldsymbol{\alpha}\cdot\mathbf{x}})\mathbf{u}$$

$$= \ e^{\beta \boldsymbol{\alpha} \cdot \mathbf{x}} (\mathbf{T} + \beta \sum_{i=1}^{d} (\alpha_i \mathbf{F}^i)) \mathbf{u}$$

the parameter β can be chosen sufficiently large to ensure that $\mathbf{T}^1 := \mathbf{T} + \beta \sum_{i=1}^{d}(\alpha_i \mathbf{F}^i)$ satisfies condition (T3). Thus, under the transformation $\mathbf{u} = e^{\beta \boldsymbol{\alpha} \cdot \mathbf{x}} \mathbf{v}$, the symmetric first-order hyperbolic system $\mathbf{Tv} = \mathbf{f}$ is equivalent to the Friedrichs system $\mathbf{T}^1 \mathbf{v} = e^{-\beta \boldsymbol{\alpha} \cdot \mathbf{x}} \mathbf{f}$ with suitable boundary conditions which will be discussed later in the chapter. More details about this transformation can be found in Jensen (2004).

hdCDD System: It can be easily seen that the hdCDD system (3.8) is a symmetric first-order hyperbolic system. We are now ready to show that the hdCDD system can be transformed into the Friedrichs' system with a suitable domain Ω, condition for a given function v, suitable $\boldsymbol{\alpha} \in \mathbb{R}^d$ and $\beta > 0$ and then Friedrichs' operators can be defined by restating the hdCDD system (3.8) as following proposition.

Proposition 3.1.4. Let $\Omega = (0, T) \times \Gamma \times S^1$ where $0 < T < \infty$, Γ is a bounded, open, and connected Lipschitz domain in $\mathbb{R}^2$ and $S^1 := \mathbb{R}/2\pi\mathbb{Z}$. Set $L = [L^2(\Omega)]^2$ and $\mathcal{D} = [C_0^\infty(\Omega)]^2$. Let $v \in C^2(\overline{\Gamma}; \mathbb{R})$ and

$$\mathbf{F}^1(x, y, \varphi) \ = \ \begin{bmatrix} v \sin \varphi & 0 \\ 0 & v \sin \varphi \end{bmatrix}, \quad \mathbf{F}^2(x, y, \varphi) = \begin{bmatrix} -v \cos \varphi & 0 \\ 0 & -v \cos \varphi \end{bmatrix},$$

$$\mathbf{F}^3(x, y, \varphi) \ = \ \begin{bmatrix} -\mathbf{l} \cdot \nabla v & 0 \\ 0 & -\mathbf{l} \cdot \nabla v \end{bmatrix}, \quad \mathbf{B}(x, y, \varphi) = \begin{bmatrix} 0 & -v \\ -2\mathbf{l}' \cdot \nabla v + \mathbf{l} \cdot \nabla(\mathbf{l} \cdot \nabla v) & -\mathbf{l}' \cdot \nabla v \end{bmatrix},$$

with $\mathbf{l} = (\cos \varphi, \sin \varphi)$ are in $[L^\infty(\Gamma \times (0, 2\pi))]^{2 \times 2}$. Then the hdCDD system from (3.8)

$$\partial_t \mathbf{u} + \mathbf{Fu} + \mathbf{Bu} \ = \ \mathbf{0} \tag{3.13}$$

with $\mathbf{Fu} = \sum_{i=1}^{3} \mathbf{F}^i \partial_i \mathbf{u}$, can be transformed to a Friedrichs' system.

Proof. By following the transformation of symmetric first-order hyperbolic system into Friedrichs' system, we will show that there exist $\boldsymbol{\alpha} \in \mathbb{R}^4$ and $\beta > 0$ such that after scaling (3.10) is satisfied. Let $\boldsymbol{\alpha} = (1, 0, 0, 0)^\top$ and substitute $\mathbf{u} = e^{\beta \alpha \cdot \mathbf{x}} \mathbf{v}$ in (3.13) where $\mathbf{x} = (t, x, y, \varphi)^\top \in \Omega$. We have

$$\mathbf{I}_2 \partial_t \mathbf{v} + \mathbf{Fv} + (\mathbf{B} + \beta \mathbf{I}_2) \mathbf{v} \ = \ \mathbf{0}$$

where $\mathbf{I}_2$ is identity in $\mathbb{R}^{2 \times 2}$. Condition (3.10b) can easily be seen. (3.10a) follows by assumption that $v \in C^2(\Gamma)$ then we have $v, \partial_x v, \partial_y v, \partial_{xy} v, \partial_{xx} v, \partial_{yy} v$ are in $C^0(\overline{\Gamma})$ and thus $(\mathbf{B} + \beta \mathbf{I}_2)$, $\mathbf{F}^i$, $i = 1, 2, 3$, and $\sum_{i=1}^{3} \partial_i \mathbf{F}^i$ are in $[L^\infty(\Omega)]^{2 \times 2}$.

For (3.10c), we have to show that there exist $\mu, \beta > 0$ such that

$$\mathbf{B} + \mathbf{B}^\top + 2\beta\mathbf{I}_2 - \sum_{k=1}^{d} \partial_i \mathbf{F}^i \;\geq\; \mu\mathbf{I}_m.$$

With the symmetric property of $\mathbf{F}^i$ and $(\mathbf{B} + (\mathbf{B})^\top)$ for all $(x, y) \in \overline{\Gamma}$, we can find real eigenvalues λ_1, λ_2 of $(\mathbf{B} + \mathbf{B}^\top - \sum_{k=1}^{d} \partial_i \mathbf{F}^i)$ and choose $\beta > \max\{|\lambda_1|, |\lambda_2|\}$ to get the condition of $\mu = \beta - \max\{|\lambda_1|, |\lambda_2|\} > 0$. Then all of conditions of Friedrichs' systems has been fulfilled. $\qquad\square$

3.2 Well-posedness and Boundary Conditions

In this section we will investigate boundary conditions that can be used to define a subspace $V \subset L$ such that a Friedrichs' operator $\mathbf{T} : V \to L$ is bijective. Then for a given function $\mathbf{f} \in L$, there exists a unique solution $\mathbf{u} \in V$ such that $\mathbf{Tu} = \mathbf{f}$ and also similarly to a restricted subspace $V^* \subset L$ for $\widetilde{\mathbf{T}}$.

We will find the maximal domain for Friedrichs' operator $\mathbf{T} : \mathcal{D} \to L$ by extending the operator as in Ern et al. (2007). The first extension is from $\mathcal{D}$ to the closure of this dense space, say $W_0 := \overline{\mathcal{D}}^{\|\cdot\|_{W_0}}$, with respect to the graph norm $\|\cdot\|_{W_0} := \|\cdot\|_L + \|\mathbf{T}\cdot\|_L$. The operators $\mathbf{T}$ and $\widetilde{\mathbf{T}}$ now have the unique extension domain to W_0 which is the minimal domain in the terminology of (Aubin, 2000, Ch.5). The space W_0 and the property (T1) of Friedrichs' operator, we have the following identifications:

$$\mathcal{D} \subset W_0 \subset L \equiv L' \subset W_0' \subset \mathcal{D}' \tag{3.14}$$

where $\mathcal{D}'$ is the algebraic dual of $\mathcal{D}$ and L' and W_0' are topological duals. We now then abuse the notation by setting $\mathbf{T} = (\widetilde{\mathbf{T}})^* \in \mathcal{L}(L; W_0')$ and $\widetilde{\mathbf{T}} = \mathbf{T}^* \in \mathcal{L}(L; W_0')$. Since $L \subset W_0'$ where $(\cdot)^*$ represents the adjoint operator, the following space is make sense to be defined

$$W \;=\; \{v \in L; \mathbf{T}v \in L\} \;=\; \{v \in L; \widetilde{\mathbf{T}}v \in L\}, \tag{3.15}$$

and clearly $W_0 \subset W$. The space W, called *graph space* with graph norm $\|\cdot\|_W := \|\cdot\|_L + \|\mathbf{T}\cdot\|_L$, is the maximal domain of $\mathbf{T}$ and $\widetilde{\mathbf{T}}$ and can be shown to be a Hilbert space (Ern et al., 2007, Lem. 2.1).

3.2.1 Well-posedness

Now we have the extended operators $\mathbf{T}$ and $\widetilde{\mathbf{T}}$ in $\mathcal{L}(W; L)$. In this subsection, we will identify sufficient conditions on subspaces V and V^* in W such that the restricted

operators $\mathbf{T} : V \to L$ and $\widetilde{\mathbf{T}} : V^* \to L$ are isomorphisms. Let us first introduce the operator $\mathbf{D} \in \mathcal{L}(W; W')$ such that for all $(u, v) \in W \times W$

$$\langle \mathbf{D}u, v \rangle_{W',W} \;\; = \;\; (\mathbf{T}u, v)_L - (u, \widetilde{\mathbf{T}}v)_L, \tag{3.16}$$

with the following property.

Property 3.2.1. Assume (T1) and (T2), then $\mathbf{D}$ is self-adjoint operator, i.e., for all $(u, v) \in W \times W$,

$$\langle \mathbf{D}u, v \rangle_{W',W} \;\; = \;\; \langle \mathbf{D}v, u \rangle_{W',W}. \tag{3.17}$$

Proof.

$$
\begin{aligned}
\langle \mathbf{D}u, v \rangle_{W',W} - \langle \mathbf{D}v, u \rangle_{W',W} \;\; &= \;\; \Big((\mathbf{T}u, v)_L - (u, \widetilde{\mathbf{T}}v)_L \Big) - \Big((\mathbf{T}v, u)_L + (v, \widetilde{\mathbf{T}}u)_L \Big) \\
&= \;\; ((\mathbf{T} + \widetilde{\mathbf{T}})u, v)_L - ((\mathbf{T} + \widetilde{\mathbf{T}})v, u)_L \;\; = \;\; 0.
\end{aligned}
$$

by using the self-adjoint property of $\mathbf{T} + \widetilde{\mathbf{T}}$ on L from Lemma 3.1.2. □

Moreover it can be shown that Ker $\mathbf{D} = W_0$ (Ern et al., 2007, Lemma 2.4) and therefore one can think of $\mathbf{D}$ as a boundary operator compared to an integration by parts as from the definition of $\mathbf{D}$, we have

$$(\mathbf{T}u, v)_L \;\; = \;\; (u, \widetilde{\mathbf{T}}v)_L + \langle \mathbf{D}u, v \rangle_{W',W}.$$

Now we are ready to state two key assumptions to define subspaces V and V^* in W by the following:

$$V \subset \{w \in W; \langle \mathbf{D}w, w \rangle_{W',W} \geq 0\}, \quad V^* \subset \{w \in W; \langle \mathbf{D}w, w \rangle_{W',W} \leq 0\}, \tag{V1}$$

$$V = \mathbf{D}(V^*)^\perp, \quad V^* = \mathbf{D}(V)^\perp. \tag{V2}$$

These two assumptions lead to the important consequence for the L-coercivity of Friedrichs' operator as the following lemma.

Lemma 3.2.2. Let $\mathbf{T}, \widetilde{\mathbf{T}}$ are Friedrichs' operators and $V, V^* \subset W$ that satisfy (V1)– (V2). Then $\mathbf{T}$ is L-coercive on V and $\widetilde{\mathbf{T}}$ is L-coercive V^*.

Proof. From the definition of $\mathbf{D}$ in (3.16), it implies for all $w \in V \subset W$ that

$$
\begin{aligned}
(\mathbf{T}w, w)_L \;\; &= \;\; (\mathbf{T}w, w)_L - \frac{1}{2}\Big(\langle \mathbf{D}w, w \rangle_{W',W} - (\mathbf{T}w, w)_L + (\widetilde{\mathbf{T}}w, w)_L \Big) \\
&= \;\; \frac{1}{2}((\mathbf{T} + \widetilde{\mathbf{T}})w, w) + \frac{1}{2}\langle \mathbf{D}w, w \rangle_{W',W}
\end{aligned}
$$

$$\geq \quad \mu_0 \|w\|_L^2,$$

by using property (T3) for $(\mathbf{T} + \widetilde{\mathbf{T}})$ and $\langle \mathbf{D}w, w \rangle_{W',W} \geq 0$ from the assumption (V1) for $w \in V$. For L-coercivity of $\widetilde{\mathbf{T}}$ in V^*, the similar proof to $\mathbf{T}$ can be provided. $\square$

Then the well-posedness of Friedrichs' operator follows from the following theorem by using the existence and uniqueness properties from the inf-sup condition in Banach-Nečas-Babuška theorem (BNB), (Di Pietro and Ern, 2011, Thm. 1.1).

Theorem 3.2.3. (Ern et al., 2007, Thm. 3.1) Let $\mathbf{T}, \widetilde{\mathbf{T}}$ are Friedrichs' operators and V, V^* satisfy (V1)–(V2). Then the restricted operators $\mathbf{T} : V \to L$ and $\widetilde{\mathbf{T}} : V^* \to L$ are isomorphisms.

Corollary 3.2.4. Let $\mathbf{T}, \widetilde{\mathbf{T}}$ are Friedrichs' operators from Thm.3.2.3 and $f \in L$. Then the following problems are well-posed:

$$\text{Find } u \in V \quad \text{such that} \quad \mathbf{T}u = f \quad \text{in} \quad L. \tag{3.18}$$

$$\text{Find } u^* \in V^* \quad \text{such that} \quad \widetilde{\mathbf{T}}u^* = f \quad \text{in} \quad L. \tag{3.19}$$

3.2.2 Boundary Conditions

In the assumptions (V1) and (V2), there are some freedom to design the subspace $V \subset \{w \in W; \langle \mathbf{D}w, w \rangle_{W',W} \geq 0\}$ and also for V^* by introducing a boundary operator, say $\mathbf{M}$, that for example the space V can be defined as the kernel of a combined boundary operator $\mathbf{D} - \mathbf{M}$. We state assumptions for an operator $\mathbf{M} \in \mathcal{L}(W; W')$ such that for $w \in W$,

$$\mathbf{M} \quad \text{is positive, i.e. } \langle \mathbf{M}w, w \rangle_{W',W} \geq 0, \tag{M1}$$

$$W = \text{Ker}(\mathbf{D} - \mathbf{M}) + \text{Ker}(\mathbf{D} + \mathbf{M}), \tag{M2}$$

and let $\mathbf{M}^* \in \mathcal{L}(W; W')$ denote the adjoint operator of $\mathbf{M}$ defined as follows: for all $u, v \in W$

$$\langle \mathbf{M}u, v \rangle_{W',W} = \langle \mathbf{M}^*v, u \rangle_{W',W}. \tag{3.20}$$

The important result from these assumptions is that the relation to the subspace V, V^* and the assumptions (V1)–(V2) as the following theorem.

Theorem 3.2.5. (Ern et al., 2007, Thm. 4.2) Assume that $\mathbf{M} \in \mathcal{L}(W; W')$ satisfies (M1)–(M2) and set

$$V = \text{Ker}(\mathbf{D} - \mathbf{M}), \tag{3.21}$$

$$V^* = \text{Ker}(\mathbf{D} + \mathbf{M}^*), \tag{3.22}$$

then V and V^* satisfy (V1)–(V2).

3.2.3 Weakly Enforced Boundary

We will later apply the discontinuous Galerkin method as numerical method, which need the weak formulation with weakly enforced boundary conditions. We consider the Friedrich's operator $\mathbf{T}$ by defining the bilinear form $a \in \mathcal{L}(W \times W; \mathbb{R})$,

$$a(\mathbf{u}, \mathbf{v}) \;=\; (\mathbf{T}\mathbf{u}, \mathbf{v})_L + \frac{1}{2}\langle (\mathbf{M} - \mathbf{D})\mathbf{u}, \mathbf{v} \rangle_{W',W}, \qquad (3.23)$$

with the following property.

Property 3.2.6. The corresponding bilinear form $a \in \mathcal{L}(W \times W; \mathbb{R})$ of the Friedrichs' operator $\mathbf{T}$ defined in (3.23) is L-coercive on W, i.e., there is $\mu_0 > 0$ for all $\mathbf{w} \in W$,

$$a(\mathbf{w}, \mathbf{w}) \;\geq\; \mu_0 \|\mathbf{w}\|_L^2 + \frac{1}{2}\langle \mathbf{M}\mathbf{w}, \mathbf{w} \rangle_{W',W}. \qquad (3.24)$$

Proof. With the definition of the boundary operator $\mathbf{D}$, it follows

$$
\begin{aligned}
a(\mathbf{w}, \mathbf{w}) \;&=\; (\mathbf{T}\mathbf{w}, \mathbf{w})_L - \frac{1}{2}\langle \mathbf{D}\mathbf{w}, \mathbf{w} \rangle_{W',W} + \frac{1}{2}\langle \mathbf{M}\mathbf{w}, \mathbf{w} \rangle_{W',W} \\
&=\; (\mathbf{T}\mathbf{w}, \mathbf{w})_L - \frac{1}{2}\Big((\mathbf{T}\mathbf{w}, \mathbf{w})_L - (\widetilde{\mathbf{T}}\mathbf{w}, \mathbf{w})_L \Big) + \frac{1}{2}\langle \mathbf{M}\mathbf{w}, \mathbf{w} \rangle_{W',W} \\
&=\; \frac{1}{2}((\mathbf{T} + \widetilde{\mathbf{T}})\mathbf{w}, \mathbf{w})_L + \frac{1}{2}\langle \mathbf{M}\mathbf{w}, \mathbf{w} \rangle_{W',W}
\end{aligned}
$$

and together with property (T3) of Friedrichs' operators then there is $\mu_0 > 0$ such that (3.24) holds. $\qquad \square$

The alternative formulation of (3.18) with weakly enforced boundary conditions is stated in the theorem belows.

Theorem 3.2.7. (Ern and Guermond, 2006, Thm.2.8) Let a bilinear $a(\cdot, \cdot)$ be defined in (3.23) and $\mathbf{f}$ be a given function in L. Then, there is a unique solution $\mathbf{u} \in W$ such that

$$a(\mathbf{u}, \mathbf{w}) \;=\; (\mathbf{f}, \mathbf{w})_L \qquad (3.25)$$

for all $\mathbf{w} \in W$. Moreover this solution $\mathbf{u}$ solves (3.18).

Proof. Since $\mathbf{T} \in \mathcal{L}(V; L)$ is isomorphic by theorem 3.2.3, there is a unique $\mathbf{u} \in V \subset W$ such that $\mathbf{T}\mathbf{u} = \mathbf{f}$. Moreover since $V = \mathrm{Ker}(\mathbf{D} - \mathbf{M})$, it follows that $\langle (\mathbf{M} - \mathbf{D})\mathbf{u}, \mathbf{w} \rangle_{W',W} = 0$ for all $\mathbf{w} \in W$. Then, we get the existence of $\mathbf{u} \in W$ that $a(\mathbf{u}, \mathbf{v}) = (\mathbf{f}, \mathbf{v})_L$ for all $\mathbf{w} \in W$ and this $\mathbf{u}$ solves (3.18). The uniqueness follows directly from L-coercivity of the bilinear form a in property 3.2.6. $\qquad \square$

3.2.4 Examples

Scalar hyperbolic equation: Let Ω be a bounded, open, and connected Lipschitz domain in $\mathbb{R}^d$ and $\mathbf{v}$ be a vector field in $\mathbb{R}^d$ such that $\mathbf{v} \in [L^\infty(\Omega)]^d$ and $\nabla \cdot \mathbf{v} \in L^\infty(\Omega)$. Define the inflow boundary $\partial\Omega^-$ and the outflow boundary $\partial\Omega^+$ as follows:

$$\partial\Omega^- = \{x \in \partial\Omega; \mathbf{v}(x) \cdot \mathbf{n}(x) < 0\}, \quad \partial\Omega^+ = \{x \in \partial\Omega; \mathbf{v}(x) \cdot \mathbf{n}(x) > 0\}. \quad (3.26)$$

Let $\mu \in L^\infty(\Omega)$ and assume that there exists $\mu_0 > 0$ such that

$$\mu(x) - \frac{1}{2}\nabla \cdot \mathbf{v}(x) \geq \mu_0 \geq 0 \quad \text{a.e. in} \quad \Omega. \quad (3.27)$$

Consider the advection-reaction equation for a given function $f \in L^2(\Omega)$

$$\mu u + \mathbf{v} \cdot \nabla u \;=\; f. \quad (3.28)$$

We can define Friedrichs' operators $\mathbf{T}$ and $\widetilde{\mathbf{T}}$ on $\mathcal{D} = C_0^1(\Omega)$ that is dense in $L = L^2(\Omega)$

$$\mathbf{T} = \mu + \mathbf{v} \cdot \nabla, \qquad \widetilde{\mathbf{T}} = \mu - \nabla \cdot \mathbf{v} - \mathbf{v} \cdot \nabla \quad (3.29)$$

together with the graph space

$$W \;=\; \{w \in L^2(\Omega); \quad \mathbf{v} \cdot \nabla w \in L^2(\Omega)\}. \quad (3.30)$$

We state the properties of W that will be used later from Ern and Guermond (2004) that

$$C^1(\overline{\Omega}) \quad \text{is dense in} \quad W, \quad (3.31)$$

$$\exists \psi^-, \psi^+ \in C^1(\overline{\Omega}) \quad \text{s.t.} \quad \psi^- + \psi^+ = 1 \,\text{on}\, \Omega, \quad \psi^-|_{\partial\Omega^+} = 0, \; \psi^+|_{\partial\Omega^-} = 0. \quad (3.32)$$

Then Friedrichs' operators have unique extensions and as before we abuse the notations for the extended operators $\mathbf{T}, \widetilde{\mathbf{T}} \in \mathcal{L}(W, L)$.

Moreover, the operator $\mathbf{D}$ has the following representation, for all $u, v \in W$

$$\langle \mathbf{D}u, v \rangle_{W',W} \;=\; \int_{\partial\Omega} uv(\mathbf{v} \cdot \mathbf{n}) \, \mathrm{d}a. \quad (3.33)$$

We observe that

$$\int_{\partial\Omega} uv(\mathbf{v} \cdot \mathbf{n})\mathrm{d}a \;=\; \int_\Omega \nabla \cdot (uv\mathbf{v})\mathrm{d}x$$

$$=\; \int_\Omega \Big((\nabla u \cdot \mathbf{v})v + (\nabla v \cdot \mathbf{v})u + uv\nabla \cdot \mathbf{v}\Big)\mathrm{d}x,$$

which shows that the operator $\mathbf{D}$ is well-defined in $\mathbf{W}$. For boundary conditions, set

$$V = \{w \in W; \quad w|_{\partial\Omega^-} = 0\}, \qquad V^* = \{w \in W; \quad w|_{\partial\Omega^+} = 0\} \qquad (3.34)$$

Property 3.2.8. Let V and V^* be defined in (3.34), then (V1)–(V2) hold.

Proof. For (V1), it is clear from the representation of $\mathbf{D}$ in (3.33) and definitions of $\partial\Omega^-$ and $\partial\Omega^+$. For (V2), we first show that $V = \mathbf{D}(V^*)^\perp$ by letting $v \in V$ and $v^* \in V^*$ then

$$\langle \mathbf{D}v^*, v \rangle_{W',W} \quad = \quad \int_{\partial\Omega} vv^*(\mathbf{v} \cdot \mathbf{n})\mathrm{d}a \quad = \quad 0, \qquad\qquad (3.35)$$

because $v|_{\partial\Omega^-} = 0$, $v^*|_{\partial\Omega^+} = 0$ and $\mathbf{v} \cdot \mathbf{n} = 0$ on $\partial\Omega \setminus (\partial\Omega^- \cup \partial\Omega^+)$, therefore $v \in \mathbf{D}(V^*)^\perp$ and $V \subset \mathbf{D}(V^*)^\perp$. Conversely, let $v \in \mathbf{D}(V^*)^\perp$ and $\psi^- \in C^1(\overline{\Omega})$ defined in (3.32). Then $\psi^- v \in V^*$ and

$$0 = \langle \mathbf{D}(\psi^- v), v \rangle_{W',W} = \int_{\partial\Omega} \psi^- v^2 (\mathbf{v} \cdot \mathbf{n})\,\mathrm{d}a = \int_{\partial\Omega^-} v^2 (\mathbf{v} \cdot \mathbf{n})\,\mathrm{d}a. \qquad (3.36)$$

This leads to $v|_{\partial\Omega^-} = 0$, which means $v \in V$ and then $\mathbf{D}(V^*)^\perp \subset V$. For the condition $V^* = \mathbf{D}(V)^\perp$ can also be proved similarly. $\qquad\square$

The boundary operators $\mathbf{M}$ can also be defined related to V such that for $u, v \in W$

$$\begin{aligned} \langle \mathbf{M}u, v \rangle_{W',W} \quad &= \quad \int_{\partial\Omega} uv|\mathbf{v} \cdot \mathbf{n}|\,\mathrm{d}a \\ &= \quad \int_{\partial\Omega^+} uv(\mathbf{v} \cdot \mathbf{n})\,\mathrm{d}a - \int_{\partial\Omega^-} uv(\mathbf{v} \cdot \mathbf{n})\,\mathrm{d}a \end{aligned}$$

and it follows that $\mathbf{M}^* = \mathbf{M}$.

Together with the definition of $\mathbf{D}$, we have

$$\langle (\mathbf{D} - \mathbf{M})u, v \rangle_{W',W} \quad = \quad 2\int_{\partial\Omega^-} uv(\mathbf{v} \cdot \mathbf{n})\,\mathrm{d}a \qquad\qquad (3.37)$$

$$\langle (\mathbf{D} + \mathbf{M}^*)u, v \rangle_{W',W} \quad = \quad 2\int_{\partial\Omega^+} uv(\mathbf{v} \cdot \mathbf{n})\,\mathrm{d}a \qquad\qquad (3.38)$$

and it can be shown that $V = \mathrm{Ker}(\mathbf{D} - \mathbf{M})$ and $V^* = \mathrm{Ker}(\mathbf{D} + \mathbf{M}^*)$.

Then the well-posed problem of scalar hyperbolic equations can be restated as follows: Find $u \in W$ such that for a given $f \in L$

$$\mu u + \mathbf{v} \cdot \nabla u \quad = \quad f \quad \text{in} \quad L, \qquad\qquad (3.39a)$$

$$(\mathbf{D} - \mathbf{M})u = 0 \quad \text{in} \quad W'. \tag{3.39b}$$

hdCDD System: From proposition 3.1.4, we obtain a Friedrichs' system by rescaling the hdCDD system. Then we can define Friedrichs' operators $\mathbf{T}$ and $\widetilde{\mathbf{T}}$ on $\mathcal{D}[C_0^1(\Omega)]^2$ which is dense in $L = [L^2(\Omega)]^2$ with $\Omega = (0, T) \times \Gamma \times S^1$, a sufficiently large $\beta > 0$ and for a given $v \in C^2(\overline{\Gamma})$,

$$\mathbf{T} = \mathbf{I}_2 \partial_t + \sum_{i=1}^{3} \mathbf{F}^i \partial_i + \mathbf{B} + \beta \mathbf{I}_2, \tag{3.40}$$

$$\widetilde{\mathbf{T}} = -\mathbf{I}_2 \partial_t - \sum_{i=1}^{3} \mathbf{F}^i \partial_i - \sum_{i=1}^{3} (\partial_i \mathbf{F}^i) + \mathbf{B}^\top + \beta \mathbf{I}_2, \tag{3.41}$$

together with the graph space

$$W = \{\mathbf{w} \in [L^2(\Omega)]^2; \ (\mathbf{I}_2 \partial_t + \sum_{i=1}^{3} \mathbf{F}^i \partial_i)\mathbf{w} \in [L^2(\Omega)]^2\}, \tag{3.42}$$

and as before we have the unique extended operators $\mathbf{T}, \widetilde{\mathbf{T}} \in \mathcal{L}(W, L)$.

From the integration by parts, we have the boundary operator $\mathbf{D}$ as follows, for all $\mathbf{u}, \mathbf{v} \in W$

$$
\begin{aligned}
\langle \mathbf{D}\mathbf{u}, \mathbf{v} \rangle_{W',W} &= \int_{\partial \Omega} \left(n_t \mathbf{I}_2 \mathbf{u} + \sum_{i=1}^{3} n_i \mathbf{F}^i \mathbf{u} \right) \cdot \mathbf{v} \, da \\
&= \int_{\partial \Omega} \left((n_t + n_x v \sin \varphi - n_y v \cos \varphi - n_\varphi (\mathbf{l} \cdot \nabla v)) \mathbf{I}_2 \mathbf{u} \right) \cdot \mathbf{v} \, da \\
&= \int_{\{0,T\} \times \Gamma \times S^1} n_t \mathbf{u} \cdot \mathbf{v} \, da \\
&\quad + \int_{(0,T) \times \partial \Gamma \times S^1} (n_x v \sin \varphi - n_y v \cos \varphi) \mathbf{u} \cdot \mathbf{v} \, da \\
&\quad - \int_{(0,T) \times \Gamma \times \{0,2\pi\}} n_\varphi (\mathbf{l} \cdot \nabla v) \mathbf{u} \cdot \mathbf{v} \, da \\
&= \int_{\partial \Omega \setminus \partial \Omega_{S^1}} \lambda(\mathbf{x})(\mathbf{u} \cdot \mathbf{v}) da
\end{aligned}
$$

where $\mathbf{n} = (n_t, n_x, n_y, n_\varphi)^\top$ is unit normal vector at $\mathbf{x} = (t, x, y, \varphi)^\top \in \partial \Omega$, $\partial \Omega_{S^1} := (0, T) \times \Gamma \times \{0, 2\pi\}$ and $\lambda(\mathbf{x}) = n_t + n_x v \sin \varphi - n_y v \cos \varphi$. We use the fact that the integration on $\partial \Omega_{S^1}$ vanishes, i.e. $\int_{\partial \Omega_{S^1}} n_\varphi (\mathbf{l} \cdot \nabla v) \mathbf{u} \cdot \mathbf{v} \, da = 0$ because of the periodic boundary conditions on S^1. To state more explicitly, here we have on the boundary in time direction $\mathbf{n} = (-1, 0, 0, 0)^\top$ at $t = 0$, $\mathbf{n} = (1, 0, 0, 0)^\top$ at $t = T$. Similar

to previous example, we define the inflow boundary $\partial\Omega^-$ and the outflow boundary $\partial\Omega^+$ as follows:

$$\partial\Omega^- = \{\mathbf{x} \in \partial\Omega \setminus \partial\Omega_{S^1}; \ \lambda(\mathbf{x}) < 0\}, \quad \partial\Omega^+ = \{\mathbf{x} \in \partial\Omega \setminus \partial\Omega_{S^1}; \ \lambda(\mathbf{x}) > 0\}, \quad (3.43)$$

and we also define the subspaces in W

$$V = \{\mathbf{w} \in W; \quad \mathbf{w}|_{\partial\Omega^-} = \mathbf{0}\}, \qquad V^* = \{\mathbf{w} \in W; \quad \mathbf{w}|_{\partial\Omega^+} = \mathbf{0}\} \quad (3.44)$$

The same argument with the proof in property 3.2.8 can be used to show that these V and V^* satisfy assumptions (V1)–(V2).

The boundary operators $\mathbf{M}$ can also be defined related to V such that for $\mathbf{u}, \mathbf{v} \in W$

$$\begin{aligned}
\langle \mathbf{Mu}, \mathbf{v} \rangle_{W',W} &= \int_{\partial\Omega \setminus \partial\Omega_{S^1}} |\lambda(\mathbf{x})| \mathbf{u} \cdot \mathbf{v} \, da \\
&= \int_{\partial\Omega^+} \lambda(\mathbf{x}) \mathbf{u} \cdot \mathbf{v} \, da - \int_{\partial\Omega^-} \lambda(\mathbf{x}) \mathbf{u} \cdot \mathbf{v} \, da
\end{aligned}$$

and then

$$\langle (\mathbf{D} - \mathbf{M})\mathbf{u}, \mathbf{v} \rangle_{W',W} = 2 \int_{\partial\Omega^-} \lambda(\mathbf{x}) \mathbf{u} \cdot \mathbf{v} \, da. \quad (3.45)$$

This defines the well-posedness of hdCDD system with zero on the inflow boundary including inflow in time domain at $t = 0$. To include initial value $\mathbf{g}$ with a suitable regularity, we have to consider the modified problem with additional function $\mathbf{u}_{\text{ini}} \in W$ such that $\mathbf{u}_{\text{ini}}(t = 0) = \mathbf{g}$: Find $\mathbf{u}_0 \in W$ such that

$$\begin{aligned}
\mathbf{T}(\mathbf{u}_0 + \mathbf{u}_{\text{ini}}) &= \mathbf{0} \quad \text{in} \quad L, & (3.46a) \\
(\mathbf{D} - \mathbf{M})\mathbf{u}_0 &= \mathbf{0} \quad \text{in} \quad W'. & (3.46b)
\end{aligned}$$

Then, $\mathbf{u}_0 + \mathbf{u}_{\text{ini}}$ is the solution for hdCDD problem with initial value $\mathbf{g}$. Therefore, we have the well-posedness result for the *open boundary* case of the hdCDD system. The *impenetrable boundary* case is more complicated due to the velocity v that depends nonlinearly on the dislocation density ρ so the well-posedness of this case is not covered in this thesis.

3.3 Explicit Runge-Kutta Discontinuous Galerkin Methods for hdCDD

The hdCDD system has been shown to be well-posed in the space-time setting. However, for the numerical treatment we would like to choose a method to solve this

problem separately in space and time by using the discontinuous Galerkin method in space and explicit Runge-Kutta methods in time, or in short explicit RKDG methods (see Cockburn and Shu (1991); Hesthaven and Warburton (2007)).

Our goal in this section is to analyze the convergence of explicit RKDG methods for the hdCDD system following the framework in Burman et al. (2010). In addition to the work of Burman et. al., we have the zero-order component $\mathbf{B}$ in the hdCDD system which needs some modification for the proof and specific parameters for hdCDD system will be also investigated here in this thesis.

We consider the hdCDD system (3.13) on $\Omega = (0,T) \times \widetilde{\Omega}$, where $\widetilde{\Omega} := \Gamma \times S^1$, together with boundary and initial conditions as follows:

Find $\mathbf{u} : (0,T) \times \widetilde{\Omega} \to \mathbb{R}^2$ solving

$$\partial_t \mathbf{u} + \mathbf{F}\mathbf{u} + \mathbf{B}\mathbf{u} = \mathbf{0} \quad \text{in } (0,T) \times \widetilde{\Omega}, \tag{3.47a}$$

$$\mathbf{u}(\cdot, t=0) = \mathbf{g} \quad \text{in } \widetilde{\Omega}, \tag{3.47b}$$

$$(\mathbf{M} - \mathbf{D})\mathbf{u} = \mathbf{0} \quad \text{on } (0,T) \times \partial\widetilde{\Omega}_{S^1} \tag{3.47c}$$

with periodic boundary conditions $\mathbf{u}(t,x,y,0) = \mathbf{u}(t,x,y,2\pi)$, $\partial\widetilde{\Omega}_{S^1} = \partial\Gamma \times S^1$ and given initial values $\mathbf{g} : \widetilde{\Omega} \to \mathbb{R}^2$.

Alternatively we can also write the system for space-time functional spaces as in (3.46). But this time with separating space and time, specifically we define spaces analog to the space-time hdCDD system, i.e., $\widetilde{L} = [L^2(\widetilde{\Omega})]^2$, a graph space

$$\widetilde{W} = \left\{ \mathbf{w} \in \widetilde{L}; \ \sum_{i=1}^{3} \mathbf{F}^i \partial_i \mathbf{w} \in \widetilde{L} \right\} \subset [H^1(\widetilde{\Omega})]^2, \tag{3.48}$$

and its subspace

$$\widetilde{V} = \left\{ \mathbf{w} \in \widetilde{W}; \quad \mathbf{w}|_{\partial\widetilde{\Omega}^-} = \mathbf{0} \right\}, \tag{3.49}$$

where $\partial\widetilde{\Omega}^- = \{\mathbf{x} \in \partial\widetilde{\Omega}_{S^1}; \ n_x v \sin\varphi - n_y v \cos\varphi < 0\}$, and similarly for $\widetilde{V}^*$ and $\partial\widetilde{\Omega}^+$.

Now we are interested in a smooth solution

$$\mathbf{u} \in C^0([0,T]; \widetilde{V}) \cap C^1([0,T]; \widetilde{L}), \tag{3.50}$$

and we can reformulate (3.47) to

$$\partial_t \mathbf{u}(t) + \mathbf{A}\mathbf{u}(t) = \mathbf{0} \quad \forall t \in [0,T], \tag{3.51}$$

with a initial value $\mathbf{u}(t=0) = \mathbf{g} \in \widetilde{V}$ and $\mathbf{A} = \mathbf{F} + \mathbf{B}$.

Introducing a corresponding bilinear form with weakly enforced boundary condition, i.e., for $(\mathbf{v}, \mathbf{w}) \in \widetilde{W} \times \widetilde{W}$,

$$a(\mathbf{v}, \mathbf{w}) \;=\; (\mathbf{F}\mathbf{v}, \mathbf{w})_{L^2} + (\mathbf{B}\mathbf{v}, \mathbf{w})_{L^2} + \frac{1}{2}((\mathbf{M} - \mathbf{D})\mathbf{v}, \mathbf{w})_{L^2, \partial\widetilde{\Omega}_{S^1}}. \tag{3.52}$$

Considering the following with the symmetry property of $\mathbf{F}^i$, integration by parts and the periodic boundary condition on S^1 yields

$$
\begin{aligned}
(\mathbf{F}\mathbf{v}, \mathbf{v})_{L^2} &\;=\; (\sum_{i=1}^{3} \partial_i(\mathbf{F}^i \mathbf{v}), \mathbf{v}) - (\boldsymbol{\mathcal{X}}\mathbf{v}, \mathbf{v})_{L^2}, \\
&\;=\; (\mathbf{D}\mathbf{v}, \mathbf{v})_{L^2, \partial\widetilde{\Omega}_{S^1}} - (\mathbf{v}, \mathbf{F}\mathbf{v})_{L^2} - (\boldsymbol{\mathcal{X}}\mathbf{v}, \mathbf{v})_{L^2},
\end{aligned}
$$

where $\boldsymbol{\mathcal{X}} = \sum_{i=1}^{3} \partial_i \mathbf{F}^i$, then we get

$$(\mathbf{F}\mathbf{v}, \mathbf{v})_{L^2} \;=\; \frac{1}{2}(\mathbf{D}\mathbf{v}, \mathbf{v})_{L^2, \widetilde{\Omega}_{S^1}} - \frac{1}{2}(\boldsymbol{\mathcal{X}}\mathbf{v}, \mathbf{v})_{L^2}. \tag{3.53}$$

Substituting this relation into (3.52), it leads to

$$a(\mathbf{v}, \mathbf{v}) \;=\; (\mathbf{B}\mathbf{v}, \mathbf{v})_{L^2} + \frac{1}{2}|\mathbf{v}|_{\mathbf{M}}^2 - \frac{1}{2}(\boldsymbol{\mathcal{X}}\mathbf{v}, \mathbf{v})_{L^2} \tag{3.54}$$

where

$$|\mathbf{v}|_{\mathbf{M}} \;:=\; (\mathbf{M}\mathbf{v}, \mathbf{v})_{L^2, \partial\widetilde{\Omega}_{S^1}}^{1/2} \tag{3.55}$$

denotes a seminorm by using the nonnegative property of the boundary operator $\mathbf{M}$.

3.3.1 Space semidiscretization

Let $\{\mathcal{T}_h\}_{h>0}$ be a family of simplicial meshes of $\widetilde{\Omega}$ where $h \leq 1$ denotes the maximal diameter of elements in $\mathcal{T}_h$. For simplicity, we assume that the meshes are affine and that $\widetilde{\Omega}$ is a polyhedron. Mesh faces are collected in the set $\mathcal{F}_h$ which is split into the set of interior faces, $\mathcal{F}_h^{\text{int}}$, and boundary faces, $\mathcal{F}_h^{\text{ext}}$. For $K \in \mathcal{T}_h$ and for $f \in \mathcal{F}_h$, $\|\cdot\|_{L^2, K}$ and $\|\cdot\|_{L^2, f}$, denote the $[L^2(K)]^2$ and $[L^2(f)]^2$ norms, respectively; and $\|\cdot\|_{L^2, \mathcal{F}_h}^2 := \sum_{f \in \mathcal{F}_h} \|\cdot\|_{L^2, f}^2$. We assume that meshes are kept fixed in time and also that the family $\{\mathcal{T}_h\}_{h>0}$ is quasi-uniform.

Let $p \geq 0$. We define spaces

$$
\begin{aligned}
W_h &\;=\; \{\mathbf{w}_h \in [L^2(\widetilde{\Omega})]^2; \forall K \in \mathcal{T}_h, \mathbf{w}_h|_K \in [\mathbb{P}_p]^2\}, \tag{3.56} \\
W(h) &\;=\; [H^1(\widetilde{\Omega})]^2 + W_h. \tag{3.57}
\end{aligned}
$$

The W_h space is a DG space consisting of discontinuous $\mathbb{R}^2$-valued piecewise polynomials of total degree $\leq p$, where in the case of $p = 0$ the DG method is equivalent

to the finite volume method. Let π_h denote the L^2-orthogonal projection onto W_h. To define the discrete operator, first we consider the system with linear operator $\mathbf{A}$ from (3.51) over the element K,

$$
\begin{aligned}
(\mathbf{A}\mathbf{w}, \mathbf{v})_{L^2, K} &= ((\mathbf{F} + \boldsymbol{\mathcal{X}})\mathbf{w}, \mathbf{v})_{L^2, K} + ((\mathbf{B} - \boldsymbol{\mathcal{X}})\mathbf{w}, \mathbf{v})_{L^2, K} \\
&= ((\sum_{i=1}^{3} \partial_i(\mathbf{F}^i \mathbf{w}), \mathbf{v})_{L^2, K} + ((\mathbf{B} - \boldsymbol{\mathcal{X}})\mathbf{w}, \mathbf{v})_{L^2, K} \\
&= -(\mathbf{w}, \mathbf{F}\mathbf{v})_{L^2, K} + ((\mathbf{B} - \boldsymbol{\mathcal{X}})\mathbf{w}, \mathbf{v})_{L^2, K} + \sum_{f \in \partial K} (\sum_{i=1}^{3} n_i^f \mathbf{F}^i \mathbf{w}, \mathbf{v})_{L^2, f},
\end{aligned}
$$

by using the integration by parts where $\mathbf{n}^f = (n_1^f, n_2^f, n_3^f)$ is the normal vector to face f. The DG method scheme starts by modifying this formulation to allow the boundary part to have interaction with nearby elements by introducing a numerical flux, say $\mathbf{F}_{K,f}^*$. We define the discrete linear operators $\mathbf{A}_h : W_h \to W_h$ such that for all $(\mathbf{w}_h, \mathbf{v}_h) \in W_h \times W_h$

$$
(\mathbf{A}_h \mathbf{w}_h, \mathbf{v}_h)_{L^2, K} = -(\mathbf{w}_h, \mathbf{F}\mathbf{v}_h)_{L^2, K} + ((\mathbf{B} - \boldsymbol{\mathcal{X}})\mathbf{w}_h, \mathbf{v}_h)_{L^2, K} + \sum_{f \in \partial K} (\mathbf{n}^f \cdot \mathbf{F}_{K,f}^{i*}(\mathbf{w}_h), \mathbf{v}_h)_{L^2, f},
$$

then with integration by parts and the symmetry of $\mathbf{F}^i$, we obtain

$$
\begin{aligned}
(\mathbf{A}_h \mathbf{w}_h, \mathbf{v}_h)_{L^2, K} &= (\mathbf{F}\mathbf{w}_h, \mathbf{v}_h)_{L^2, K} + (\mathbf{B}\mathbf{w}_h, \mathbf{v}_h)_{L^2, K} \\
&\quad - \sum_{f \in \partial K} (\sum_{i=1}^{3} n_i^f \mathbf{F}^i \mathbf{w}_h - \mathbf{n}^f \cdot \mathbf{F}_{K,f}^{i*}(\mathbf{w}_h), \mathbf{v}_h)_{L^2, f}.
\end{aligned}
$$

The numerical upwind flux is defined as follows

$$
\mathbf{n}^f \cdot \mathbf{F}_{K,f}^*(\mathbf{w}_h) = \sum_{i=1}^{3} n_i^f \{\!\{\mathbf{F}^i \mathbf{w}_h\}\!\} + \frac{C_f}{2}[\![\mathbf{w}_h]\!], \tag{3.58}
$$

where for a fixed common interior face f between cells K and K_f, we define the average and the jump along a normal $\mathbf{n}_f$ oriented from K to K_f as

$$
\{\!\{\mathbf{v}_h\}\!\} = \frac{\mathbf{v}_h|_K + \mathbf{v}_h|_{K_f}}{2}, \qquad [\![\mathbf{v}_h]\!] := \mathbf{v}_h|_K - \mathbf{v}_h|_{K_f},
$$

respectively and the normal velocity $C_f = |\mathbf{V} \cdot \mathbf{n}^f|$, where $\mathbf{V} = (-v\partial_\varphi \mathbf{l}, -\mathbf{L} \cdot \hat{\nabla} v)$ is the general velocity of hdCDD defined in (3.2). Then we have

$$
(\mathbf{A}_h \mathbf{w}_h, \mathbf{v}_h)_{L^2} = \sum_{K \in \mathcal{T}_h} (\mathbf{A}_h \mathbf{w}_h, \mathbf{v}_h)_{L^2, K}
$$

$$= \sum_{K \in \mathcal{T}_h} \Big[(\mathbf{F}\mathbf{w}_h, \mathbf{v}_h)_{L^2,K} + (\mathbf{B}\mathbf{w}_h, \mathbf{v}_h)_{L^2,K} \Big]$$

$$- \sum_{K \in \mathcal{T}_h} \Big[\sum_{f \in \partial K} (\sum_{i=1}^{3} n_i^f \mathbf{F}^i \mathbf{w}_h - \mathbf{n}^f \cdot \mathbf{F}^*_{K,f}(\mathbf{w}_h), \mathbf{v}_h)_{L^2,f} \Big],$$

by considering on a fixed face $f = \partial K \cap \partial K_f \in \mathcal{F}^{int}$, we have $\mathbf{n}^{f,K} = -\mathbf{n}^{f,K_f}$, then

$$(\sum_{i=1}^{3} n_i^{f,K} \mathbf{F}^i \mathbf{w}_h - \mathbf{n}^{f,K} \cdot \mathbf{F}^{i*}_{K,f}(\mathbf{w}_h), \mathbf{v}_h|_K)_{L^2,f} + (\sum_{i=1}^{3} n_i^{f,K_f} \mathbf{F}^i \mathbf{w}_h - \mathbf{n}^{f,K_f} \cdot \mathbf{F}^{i*}_{K_f,f}(\mathbf{w}_h), \mathbf{v}_h|_{K_f})_{L^2,f}$$

$$= \sum_{i=1}^{3} \Big[\frac{n_i^K}{2}(\mathbf{F}^i \mathbf{w}_h|_K - \mathbf{F}^i \mathbf{w}_h|_{K_f}, \mathbf{v}_h|_K)_{L^2,f} + \frac{n_i^{K_f}}{2}(\mathbf{F}^i \mathbf{w}_h|_{K_f} - \mathbf{F}^i \mathbf{w}_h|_K, \mathbf{v}_h|_{K_f})_{L^2,f} \Big]$$

$$- \frac{C_f}{2}(\mathbf{w}_h|_K - \mathbf{w}_h|_{K_f}), \mathbf{v}_h|_K)_{L^2,f} - \frac{C_f}{2}(\mathbf{w}_h|_{K_f} - \mathbf{w}_h|_K, \mathbf{v}_h|_{K_f})_{L^2,f}$$

$$= \sum_{i=1}^{3} n_i^K ([[\mathbf{F}^i \mathbf{w}_h]], \{\{\mathbf{v}_h\}\})_{L^2,f} - \frac{C_f}{2}([[\mathbf{w}_h]], [[\mathbf{v}_h]])_{L^2,f}.$$

Finally, the discrete operator $\mathbf{A}_h$ can be written as

$$(\mathbf{A}_h \mathbf{w}_h, \mathbf{v}_h)_{L^2} = \sum_{K \in \mathcal{T}_h} \Big[(\mathbf{F}\mathbf{w}_h, \mathbf{v}_h)_{L^2,K} + (\mathbf{B}\mathbf{w}_h, \mathbf{v}_h)_{L,K} \Big] \tag{3.59}$$

$$- \sum_{f \in \mathcal{F}_h^{int}} \Big[\sum_{i=1}^{3} n_i^f ([[\mathbf{F}^i \mathbf{w}_h]], \{\{\mathbf{v}_h\}\})_{L^2,f} - \frac{C_f}{2}([[\mathbf{w}_h]], [[\mathbf{v}_h]])_{L^2,f} \Big]$$

$$+ \sum_{f \in \mathcal{F}_h^{ext}} \frac{1}{2}((\mathbf{M} - \mathbf{D})\mathbf{w}_h, \mathbf{v}_h)_{L^2,f},$$

$$= (\mathbf{A}_h^{dg} \mathbf{w}_h, \mathbf{v}_h)_{L^2} + (\mathbf{S}_h^{dg} \mathbf{w}_h, \mathbf{v}_h)_{L^2},$$

where

$$(\mathbf{A}_h^{dg} \mathbf{w}_h, \mathbf{v}_h)_{L^2} = \sum_{K \in \mathcal{T}_h} \Big[(\mathbf{F}\mathbf{w}_h, \mathbf{v}_h)_{L^2,K} + (\mathbf{B}\mathbf{w}_h, \mathbf{v}_h)_{L^2,K} \Big] \tag{3.60}$$

$$+ \sum_{f \in \mathcal{F}_h^{ext}} \frac{1}{2}((\mathbf{M} - \mathbf{D})\mathbf{w}_h, \mathbf{v}_h)_{L^2,f}, - \sum_{f \in \mathcal{F}_h^{int}} (\sum_{i=1}^{3} n_i^f [[\mathbf{F}^i \mathbf{w}_h]], \{\{\mathbf{v}_h\}\})_{L^2,f}$$

$$(\mathbf{S}_h^{dg} \mathbf{w}_h, \mathbf{v}_h)_{L^2} = \sum_{f \in \mathcal{F}_h^{int}} (\frac{C_f}{2}[[\mathbf{w}_h]], [[\mathbf{v}_h]])_{L^2,f}. \tag{3.61}$$

We can now define the discrete DG operator for the bilinear form a from (3.52), such that

$$a_h(\mathbf{w}_h, \mathbf{v}_h) = a_h^{dg}(\mathbf{w}_h, \mathbf{v}_h) + s_h^{dg}(\mathbf{w}_h, \mathbf{v}_h), \tag{3.62}$$

where

$$a_h^{\mathrm{dg}}(\mathbf{w}_h, \mathbf{v}_h) = (\mathbf{A}_h^{\mathrm{dg}}\mathbf{w}_h, \mathbf{v}_h)_{L^2}, \quad s_h^{\mathrm{dg}}(\mathbf{w}_h, \mathbf{v}_h) = (\mathbf{S}_h^{\mathrm{dg}}\mathbf{w}_h, \mathbf{v}_h)_{L^2}. \tag{3.63}$$

Moreover we define

$$\sigma \; := \; \max_{i=1,2,3} \|\mathbf{F}^i\|_{[L^\infty(\widetilde{\Omega})]^{2\times 2}}. \tag{3.64}$$

Then, it follows

$$C_f \mathbf{I}_2 = |\mathbf{V} \cdot \mathbf{n}^f|\mathbf{I}_2 = \sum_{i=1}^{3} |n_i^f \mathbf{F}^i| \le 3\sigma \mathbf{I}_2, \tag{3.65}$$

and with a fixed face $f \in \mathcal{F}_h^{\mathrm{ext}}$, we have for $\mathbf{v}, \mathbf{w} \in [L^2(f)]^2$

$$
|((\mathbf{M} - \mathbf{D})\mathbf{v}, \mathbf{w})_{L^2,f}| \;=\; \begin{cases} 0, & f \subset \partial\widetilde{\Omega} \setminus \partial\widetilde{\Omega}^- \\ |2(\mathbf{D}\mathbf{v}, \mathbf{w})_{L^2,f}|, & f \subset \partial\widetilde{\Omega}^- \end{cases},
$$

$$
\le \; |2(\sum_{i=1}^{3} n_i^f \mathbf{F}^i \mathbf{v}, \mathbf{w})_{L^2,f}|,
$$

then by using Cauchy-Schwarz inequality,

$$|((\mathbf{M} - \mathbf{D})\mathbf{v}, \mathbf{w})_{L^2,f}| \;\le\; 6\sigma \|\mathbf{v}\|_{L^2,f} \|\mathbf{w}\|_{L^2,f}. \tag{3.66}$$

We now state the following key properties.

Property 3.3.1. Let a_h be the bilinear operator defined in (3.62). Then the following assumptions hold

(DG1) the identity for a bilinear a_h^{dg} such that for all $\mathbf{v}_h \in V_h$

$$a_h^{\mathrm{dg}}(\mathbf{v}_h, \mathbf{v}_h) \;=\; \frac{1}{2}|\mathbf{v}_h|_{\mathbf{M}}^2 - \frac{1}{2}(\boldsymbol{\mathcal{X}}\mathbf{v}_h, \mathbf{v}_h)_{L^2} + (\mathbf{B}\mathbf{v}_h, \mathbf{v}_h)_{L^2}, \tag{3.67}$$

and then it follows

$$(\mathbf{A}_h \mathbf{v}_h, \mathbf{v}_h)_{L^2} \;=\; |\mathbf{v}_h|_S^2 - \frac{1}{2}(\boldsymbol{\mathcal{X}}\mathbf{v}_h, \mathbf{v}_h)_{L^2} + (\mathbf{B}\mathbf{v}_h, \mathbf{v}_h)_{L^2}, \tag{3.68}$$

where

$$|\mathbf{v}|_S \;:=\; \left(s_h^{\mathrm{dg}}(\mathbf{v}, \mathbf{v}) + \frac{1}{2}|\mathbf{v}|_M^2 \right)^{1/2}; \tag{3.69}$$

(DG2) the strong solution $\mathbf{u}$ satisfies for all $t \in (0, T)$,

$$\partial_t \pi_h \mathbf{u} + \mathbf{A}_h^{\mathrm{dg}}\mathbf{u} = \mathbf{0}, \quad \text{and} \quad \mathbf{S}_h^{\mathrm{dg}}\mathbf{u} = \mathbf{0}; \tag{3.70}$$

(DG3) there is c_s such that for all $\mathbf{v}_h \in V_h$,

$$|\mathbf{v}_h|_S \leq c_s^{1/2}\sigma^{1/2}h^{-1/2}\|\mathbf{v}_h\|_{L^2}, \tag{3.71}$$

and there is c'_s such that for all $\mathbf{v} \in [H^{p+1}(\widetilde{\Omega})]^2$,

$$|\mathbf{v} - \pi_h\mathbf{v}_h|_S \leq c_s'^{1/2}\sigma^{1/2}h^{p+1/2}\|\mathbf{v}\|_{H^{p+1}}; \tag{3.72}$$

(DG4) there is c_L such that for all $\mathbf{v} \in V(h)$,

$$\|\mathbf{A}_h\mathbf{v}\|_{L^2} \leq \sigma\|\nabla_h\mathbf{v}\|_{L^2} + c_B\|\mathbf{v}\|_{L^2} + c_L\sigma^{1/2}h^{-1/2}|\mathbf{v}|_S, \tag{3.73}$$

where ∇_h denotes the broken gradient of $\mathbf{v}$.

Proof. (DG1): Consider similarly to (3.53), we obtain

$$(\mathbf{F}\mathbf{v}_h, \mathbf{v}_h)_{L^2,K} = \frac{1}{2}(\mathbf{D}\mathbf{v}_h, \mathbf{v}_h)_{L^2,K} - \frac{1}{2}(\boldsymbol{\mathcal{X}}\mathbf{v}_h, \mathbf{v}_h)_{L^2,K}, \tag{3.74}$$

then

$$\sum_{K\in\mathcal{T}_h}(\mathbf{F}\mathbf{v}_h, \mathbf{v}_h)_{L^2,K} = -\frac{1}{2}(\boldsymbol{\mathcal{X}}\mathbf{v}_h, \mathbf{v}_h)_{L^2,K} + \sum_{f\in\mathcal{F}_h^{\text{ext}}}\frac{1}{2}(\mathbf{D}\mathbf{v}_h, \mathbf{v}_h)_{L^2,K}$$

$$+ \sum_{f\in\mathcal{F}_h^{\text{int}}}(\sum_{i=1}^3 n_i^f[[\mathbf{F}^i\mathbf{v}_h]], \{\{\mathbf{v}_h\}\})_{L^2,f}.$$

If we substitute this in (3.60) then (3.67) holds and (3.68) follows directly from the definition of $|\cdot|_S$.

(DG2): For the strong solution, we have $\mathbf{u}$ from (3.50), then $[[\mathbf{u}]] = [[\mathbf{F}^i\mathbf{u}]] = \mathbf{0}$. It follows that for all $\mathbf{v}_h \in V_h$

$$(\mathbf{S}_h^{\text{dg}}\mathbf{u}, \mathbf{v}_h)_{L^2} = \sum_{f\in\mathcal{F}_h^{\text{int}}}(\frac{C_f}{2}[[\mathbf{u}]], [[\mathbf{v}_h]])_{L^2,f} = 0$$

and

$$(\mathbf{A}_h^{\text{dg}}\mathbf{u}, \mathbf{v}_h)_{L^2} = \sum_{K\in\mathcal{T}_h}\left[(\mathbf{F}\mathbf{u}, \mathbf{v}_h)_{L^2,K} + (\mathbf{B}\mathbf{u}, \mathbf{v}_h)_{L^2,K}\right]$$

$$+ \sum_{f\in\mathcal{F}_h^{\text{ext}}}\frac{1}{2}((\mathbf{M}-\mathbf{D})\mathbf{u}, \mathbf{v}_h)_{L^2,f}, - \sum_{f\in\mathcal{F}_h^{\text{int}}}(\sum_{i=1}^3 n_i^f[[\mathbf{F}^i\mathbf{u}]], \{\{\mathbf{v}_h\}\})_{L^2,f}$$

$$= (\mathbf{A}\mathbf{u}, \mathbf{v}_h)_{L^2} = -(\partial_t\mathbf{u}, \mathbf{v}_h)_{L^2}$$

$$= -\partial_t(\pi_h\mathbf{u}, \mathbf{v}_h)_{L^2}$$

then (3.70) holds.

(DG3): From the assumption on mesh discretization that $\mathcal{T}_h$ is shape-regular then there is a constant c such that for all $K \in \mathcal{T}_h$ and for all $f \in \partial K$

$$\|\mathbf{v}_h\|_{L^2,f} \;\leq\; c h_K^{-1/2} \|\mathbf{v}_h\|_{L^2,K}. \tag{3.75}$$

Then,

$$
\begin{aligned}
|\mathbf{v}_h|_S^2 \;&=\; \sum_{f \in \mathcal{F}_h^{\mathrm{int}}} \left(\frac{C_f}{2}[[\mathbf{v}_h]], [[\mathbf{v}_h]]\right)_{L^2,f} + \sum_{f \in \mathcal{F}_h^{\mathrm{ext}}} \frac{1}{2}(\mathbf{M}\mathbf{v}_h, \mathbf{v}_h)_{L^2,f}, \\
&\leq\; \frac{C_f}{2} \sum_{f \in \mathcal{F}_h^{\mathrm{int}}} \|(\mathbf{v}_h|_K - \mathbf{v}_h|_{K_f})\|_{L^2,f}^2 + \frac{3\sigma}{2} \sum_{f \in \mathcal{F}_h^{\mathrm{ext}}} \|\mathbf{v}_h\|_{L^2,f}^2, \\
&\leq\; 3\sigma \sum_{K \in \mathcal{T}_h} \sum_{f \in \partial K} \|\mathbf{v}_h\|_{L^2,f}^2 \;\leq\; 12c^2\sigma \sum_{K \in \mathcal{T}_h} h_K^{-1} \|\mathbf{v}_h\|_{L^2,K}^2 \\
&\leq\; 12c^2\sigma h^{-1} \|\mathbf{v}_h\|_{L^2}^2,
\end{aligned}
$$

and (3.71) follows. For (3.72), it follows from the optimality of L^2-orthogonal projection on $K \in \mathcal{T}_h$ that for $\mathbf{v} \in [H^{p+1}(K)]^2$ then there exists c_1 such that

$$\|\mathbf{v} - \pi_h \mathbf{v}_h\|_{L^2,K} \;\leq\; c_1 h_K^{p+1} \|\mathbf{v}\|_{H^{p+1},K} \tag{3.76}$$

and the proof proceeds as previously for (3.71).

(DG4): We recall from (3.59),

$$
\begin{aligned}
(\mathbf{A}_h \mathbf{v}, \mathbf{w}_h)_{L^2} \;&=\; \sum_{K \in \mathcal{T}_h} \left[(\mathbf{F}\mathbf{v}, \mathbf{w}_h)_{L^2,K} + (\mathbf{B}\mathbf{v}, \mathbf{w}_h)_{L^2,K}\right] + \sum_{f \in \mathcal{F}_h^{\mathrm{ext}}} \frac{1}{2}((\mathbf{M}-\mathbf{D})\mathbf{v}, \mathbf{w}_h)_{L^2,f}, \\
&\quad - \sum_{f \in \mathcal{F}_h^{\mathrm{int}}} \left(\sum_{i=1}^3 n_i^f [[\mathbf{F}^i\mathbf{v}]], \{\{\mathbf{w}_h\}\}\right)_{L^2,f} + (\mathbf{S}_h^{\mathrm{dg}}\mathbf{v}, \mathbf{w}_h)_{L^2} \\
&\leq\; \sum_{K \in \mathcal{T}_h} \|\mathbf{F}\mathbf{v}\|_{L^2,K}\|\mathbf{w}_h\|_{L^2} + \|\mathbf{B}\mathbf{v}\|_{L^2}\|\mathbf{w}_h\|_{L^2} \\
&\quad + \sum_{f \in \mathcal{F}_h^{\mathrm{ext}}} \frac{1}{2}\|(\mathbf{M}-\mathbf{D})\mathbf{v}\|_{L^2,f}\|\mathbf{w}_h\|_{L^2,f} + \sum_{f \in \mathcal{F}_h^{\mathrm{int}}} \sum_{i=1}^3 \|n_i^f [[\mathbf{F}^i\mathbf{v}]]\|_{L^2,f}\|\mathbf{w}_h\|_{L^2,f} \\
&\quad + \sum_{f \in \mathcal{F}_h^{\mathrm{int}}} \frac{C_f}{2}|\mathbf{v}|_S\|[[\mathbf{w}_h]]\|_{L^2,f} \\
&\leq\; \sigma\|\nabla_h \mathbf{v}\|_{L^2}\|\mathbf{w}_h\|_{L^2} + \|\mathbf{B}\|_\infty\|\mathbf{v}\|_{L^2}\|\mathbf{w}_h\|_{L^2} \\
&\quad + ch^{-1/2}|\mathbf{v}|_S\|\mathbf{w}_h\|_{L^2} + ch^{-1/2}C_f|\mathbf{v}|_S\|\mathbf{w}_h\|_{L^2}.
\end{aligned}
$$

Then,

$$
\begin{aligned}
\|\mathbf{A}_h\mathbf{v}\|_{L^2} &= \sup_{\|\mathbf{w}_h\|_{L^2}\neq 0} \frac{|(\mathbf{A}_h\mathbf{v},\mathbf{w}_h)_{L^2}|}{\|\mathbf{w}_h\|_{L^2}} \\
&\leq \sigma\|\nabla_h\mathbf{v}\|_{L^2} + c_B\|\mathbf{v}\|_{L^2} + c_L\sigma^{1/2}h^{-1/2}|\mathbf{v}|_S.
\end{aligned}
$$

$\square$

Moreover we define the norm

$$
\begin{aligned}
\|\mathbf{w}\|_* &:= \sigma^{1/2}h^{1/2}\|\nabla_h\mathbf{w}\|_{L^2} + \sigma^{1/2}h^{-1/2}\|\mathbf{w}\|_{L^2} \\
&\quad + \sigma^{1/2}\|\mathbf{w}\|_{L^2,\mathcal{F}_h} + |\mathbf{w}|_S;
\end{aligned}
\tag{3.77}
$$

then it implies from (DG4) that for all $\mathbf{v} \in V(h)$,

$$
\|\mathbf{A}_h\mathbf{v}\|_{L^2} \leq c'_L\sigma^{1/2}h^{-1/2}\|\mathbf{v}\|_*,
\tag{3.78}
$$

with $c'_L = \max(1, c_L)$. Using inverse and trace inequalities, it is inferred that there is c_* s.t. for all $\mathbf{v}_h \in V_h$,

$$
\|\mathbf{v}_h\|_* \leq c_*\sigma^{1/2}h^{-1/2}\|\mathbf{v}_h\|_{L^2}.
\tag{3.79}
$$

Hence, letting $c_{L*} := c'_L c_*$, there holds for all $\mathbf{v}_h \in V_h$,

$$
\|\mathbf{A}_h\mathbf{v}_h\|_{L^2} \leq c_{L*}\sigma h^{-1/2}\|\mathbf{v}_h\|_{L^2}.
\tag{3.80}
$$

Furthermore, using (3.72) and usual approximation properties in finite element spaces, it is inferred that there is c'_* such that for all $\mathbf{v} \in [H^{p+1}(\widetilde{\Omega})]^2$,

$$
\|\mathbf{v} - \pi_h\mathbf{v}\|_* \leq c'_*\sigma^{1/2}h^{p+1/2}\|\mathbf{v}\|_{[H^{p+1}(\widetilde{\Omega})]^2}.
\tag{3.81}
$$

3.3.2 Analysis of explicit RK3 schemes

We consider the third-order Heun version of RK3, which is usually written as follows:

$$
\begin{aligned}
\mathbf{k}_1 &= -\mathbf{A}_h\mathbf{u}_h^n + \mathbf{f}_h^n, & (3.82) \\
\mathbf{k}_2 &= -\mathbf{A}_h(\mathbf{u}_h^n + \frac{\tau}{3}\mathbf{k}_1) + \mathbf{f}_h^{n+1/3}, & (3.83) \\
\mathbf{k}_3 &= -\mathbf{A}_h(\mathbf{u}_h^n + \frac{2\tau}{3}\mathbf{k}_2) + \mathbf{f}_h^{n+2/3}, & (3.84) \\
\mathbf{u}_h^{n+1} &= \mathbf{u}_h^n + \frac{\tau}{4}(\mathbf{k}_1 + 3\mathbf{k}_3). & (3.85)
\end{aligned}
$$

In our case for hdCDD system, we have in the homogeneous case such that $\mathbf{f} = \mathbf{0}$ then this can be rewritten as

$$\mathbf{u}_h^{n+1} \;=\; \mathbf{u}_h^n - \tau\mathbf{A}_h\mathbf{u}_h^n + \frac{\tau^2}{2}\mathbf{A}_h^2\mathbf{u}_h^n - \frac{\tau^3}{6}\mathbf{A}_h^3\mathbf{u}_h^n. \tag{3.86}$$

For the later use in the error analysis, we define the additional functions,

$$\mathbf{w} \;=\; \mathbf{u} + \tau\partial_t\mathbf{u}, \tag{3.87}$$

$$\mathbf{y} \;=\; \mathbf{u} + \tau\partial_t\mathbf{u} + \frac{1}{2}\tau^2\partial_t^2\mathbf{u}, \tag{3.88}$$

together with their discrete forms

$$\mathbf{w}_h^n \;=\; \mathbf{u}_h^n - \tau\mathbf{A}_h\mathbf{u}_h^n, \tag{3.89}$$

$$\mathbf{y}_h^n \;=\; \frac{1}{2}(\mathbf{u}_h^n + \mathbf{w}_h^n) - \frac{1}{2}\tau\mathbf{A}_h\mathbf{w}_h^n. \tag{3.90}$$

Then we can rewrite the RK3 scheme (3.86) as

$$\mathbf{u}_h^{n+1} \;=\; \frac{1}{3}(\mathbf{u}_h^n + \mathbf{w}_h^n + \mathbf{y}_h^n) - \frac{1}{3}\tau\mathbf{A}_h\mathbf{y}_h^n. \tag{3.91}$$

Moreover define

$$\xi_h^n = \mathbf{u}_h^n - \pi_h\mathbf{u}^n, \quad \zeta_h^n = \mathbf{w}_h^n - \pi_h\mathbf{w}^n, \quad \theta_h^n = \mathbf{y}_h^n - \pi_h\mathbf{y}^n, \tag{3.92}$$

$$\xi_\pi^n = \mathbf{u}^n - \pi_h\mathbf{u}^n, \quad \zeta_\pi^n = \mathbf{w}^n - \pi_h\mathbf{w}^n, \quad \theta_\pi^n = \mathbf{y}^n - \pi_h\mathbf{y}^n. \tag{3.93}$$

Lemma 3.3.2. With the RK3 scheme (3.89)–(3.91) together with $\mathbf{w}, \mathbf{y}$ defined in (3.87)–(3.88) and the error functions defined in (3.92)–(3.93), there holds

$$\zeta_h^n \;=\; \xi_h^n - \tau\mathbf{A}_h\xi_h^n + \tau\alpha_h^n, \tag{3.94}$$

$$\theta_h^n \;=\; \frac{1}{2}(\xi_h^n + \zeta_h^n) - \frac{1}{2}\tau\mathbf{A}_h\zeta_h^n + \frac{1}{2}\tau\beta_h^n, \tag{3.95}$$

$$\xi_h^{n+1} \;=\; \frac{1}{3}(\xi_h^n + \zeta_h^n + \theta_h^n) - \frac{1}{3}\tau\mathbf{A}_h\theta_h^n + \frac{1}{3}\tau\gamma_h^n, \tag{3.96}$$

with

$$\alpha_h^n = \mathbf{A}_h\xi_\pi^n, \quad \beta_h^n = \mathbf{A}_h\zeta_\pi^n, \quad \gamma_h^n = \mathbf{A}_h\theta_\pi^n - \pi_h\eta^n, \tag{3.97}$$

where

$$\eta^n \;=\; \tau^{-1}\int_{t_n}^{t_{n+1}} \frac{1}{2}(t_{n+1} - t)^3\partial_t^4\mathbf{u}\, \mathrm{d}t. \tag{3.98}$$

Proof. Recall from (DG2) that $\partial_t \pi_h \mathbf{u} + \mathbf{A}_h \mathbf{u} = \mathbf{0}$, it follows for $\mathbf{w}^n$ in (3.87)

$$\pi_h \mathbf{w}^n = \pi_h \mathbf{u}^n + \tau \pi_h \partial_t \mathbf{u}^n = \pi_h \mathbf{u}^n - \tau \mathbf{A}_h \mathbf{u}^n. \tag{3.99}$$

We subtract this from (3.89)

$$
\begin{aligned}
\mathbf{w}_h^n - \pi_h \mathbf{w}^n &= (\mathbf{u}_h^n - \pi_h \mathbf{u}) - \tau \mathbf{A}_h \mathbf{u}_h^n + \tau \mathbf{A}_h \mathbf{u}^n, \\
&= (\mathbf{u}_h^n - \pi_h \mathbf{u}) - \tau \mathbf{A}_h (\mathbf{u}_h^n - \pi_h \mathbf{u}^n) + \tau \mathbf{A}_h (\mathbf{u}^n - \pi_h \mathbf{u}^n), \\
&= \xi_h^n - \tau \mathbf{A}_h \xi_h^n + \tau \alpha_h^n,
\end{aligned}
$$

then (3.94) follows.

For (3.95), we start with the projection of $\mathbf{y}^n$

$$
\begin{aligned}
\pi_h \mathbf{y}^n &= \pi_h \mathbf{u}^n + \tau \pi_h \partial_t \mathbf{u}^n + \frac{1}{2}\tau^2 \pi_h \partial_t^2 \mathbf{u}^n, \\
&= \pi_h \mathbf{w}^n + \frac{1}{2}\tau \partial_t (\tau \pi_h \partial_t \mathbf{u}^n), \\
&= \pi_h \mathbf{w}^n + \frac{1}{2}\tau \mathbf{A}_h (\tau \partial_t \mathbf{u}^n), \\
&= \frac{1}{2}(\pi_h \mathbf{w}^n + \pi_h \mathbf{u}^n) - \frac{1}{2}\tau \mathbf{A}_h \mathbf{u}^n - \frac{1}{2}\tau \mathbf{A}_h (\mathbf{w}^n - \mathbf{u}^n),
\end{aligned}
$$

by using (DG2), (3.87) and (3.99) then

$$\pi_h \mathbf{y}^n = \frac{1}{2}(\pi_h \mathbf{w}^n + \pi_h \mathbf{u}^n) - \frac{1}{2}\tau \mathbf{A}_h \mathbf{w}^n. \tag{3.100}$$

Subtract this from (3.90), we get

$$
\begin{aligned}
\mathbf{y}_h^n - \pi_h \mathbf{y}^n &= \frac{1}{2}(\mathbf{u}_h^n - \pi_h \mathbf{u}^n) + \frac{1}{2}(\mathbf{w}_h^n - \pi_h \mathbf{w}^n) - \frac{1}{2}\tau \mathbf{A}_h (\mathbf{w}_h^n - \mathbf{w}^n), \\
&= \frac{1}{2}\xi_h^n + \frac{1}{2}\zeta_h^n - \frac{1}{2}\tau \mathbf{A}_h (\mathbf{w}_h^n - \pi_h \mathbf{w}^n) + \frac{1}{2}\tau \mathbf{A}_h (\mathbf{w}^n - \pi_h \mathbf{w}^n), \\
&= \frac{1}{2}\xi_h^n + \frac{1}{2}\zeta_h^n - \frac{1}{2}\tau \mathbf{A}_h \zeta_h^n + \frac{1}{2}\tau \mathbf{A}_h \zeta_\pi^n,
\end{aligned}
$$

then (3.95) holds.

Next for (3.96), we start with Taylor's expansion,

$$\mathbf{u}^{n+1} = \mathbf{u}^n + \tau \partial_t \mathbf{u}^n + \frac{\tau^2}{2}\partial_t^2 \mathbf{u}^n + \frac{\tau^3}{6}\partial_t^3 \mathbf{u}^n + \int_{t_n}^{t_{n+1}} \frac{(t_{n+1} - t)^3}{6}\partial_t^4 \mathbf{u} \, dt, \tag{3.101}$$

then by using $\eta^n = \tau^{-1} \int_{t_n}^{t_{n+1}} \frac{1}{2}(t_{n+1} - t)^3 \partial_t^4 \mathbf{u} \, dt$ its projection follows,

$$\pi_h \mathbf{u}^{n+1} = \pi_h \mathbf{y}^n + \frac{\tau^3}{6}\pi_h \partial_t^3 \mathbf{u}^n + \frac{\tau}{3}\pi_h \eta^n,$$

$$
= \frac{1}{3}\pi_h \mathbf{y}^n + \frac{2}{3}\pi_h \mathbf{y}^n + \frac{\tau}{3}\partial_t(\frac{\tau^2}{2}\pi_h \partial_t^2 \mathbf{u}^n) + \frac{\tau}{3}\pi_h \eta^n,
$$

$$
= \frac{1}{3}\pi_h \mathbf{y}^n + \frac{2}{3}\pi_h \mathbf{y}^n + \frac{\tau}{3}\mathbf{A}_h(\frac{\tau^2}{2}\partial_t^2 \mathbf{u}^n) + \frac{\tau}{3}\pi_h \eta^n,
$$

$$
= \frac{1}{3}(\pi_h \mathbf{y}^n + \pi_h \mathbf{w}^n + \pi_h \mathbf{u}^n) - \frac{\tau}{3}\mathbf{A}_h \mathbf{w}^n - \frac{\tau}{3}\mathbf{A}_h(\mathbf{y}^n - \mathbf{w}^n) + \frac{\tau}{3}\pi_h \eta^n,
$$

then

$$
\pi_h \mathbf{u}^{n+1} = \frac{1}{3}(\pi_h \mathbf{y}^n + \pi_h \mathbf{w}^n + \pi_h \mathbf{u}^n) - \frac{\tau}{3}\mathbf{A}_h \mathbf{y}^n + \frac{\tau}{3}\pi_h \eta^n. \tag{3.102}
$$

As previously, we subtract this from (3.91) then (3.96) holds. $\qquad\square$

Energy identity and stability

We derive an energy identity that will later be used for stability estimation.

Lemma 3.3.3 (energy identity). The following identity holds

$$
\frac{1}{2}\|\xi_h^{n+1}\|_{L^2}^2 - \frac{1}{2}\|\xi_h^n\|_{L^2}^2 + \frac{\tau}{2}|\xi_h^n|_S^2 + \frac{\tau}{6}|\zeta_h^n|_S^2 + \frac{\tau}{3}|\theta_h^n|_S^2 + \frac{1}{6}\|\theta_h^n - \zeta_h^n\|_{L^2}^2 \tag{3.103}
$$

$$
= \frac{\tau}{6}|\zeta_h^n - \xi_h^n|_S^2 + \frac{1}{2}\|\xi_h^{n+1} - \theta_h^n\|_{L^2}^2 + \boldsymbol{\mathcal{X}}_h^n + \mathbf{B}_h^n + \frac{\tau}{3}(\gamma_h^n, \theta_h^n)_{L^2}
$$

$$
+ \frac{\tau}{6}(\beta_h^n, \xi_h^n)_{L^2} + \frac{\tau}{3}(\alpha_h^n, \xi_h^n + \frac{1}{2}\zeta_h^n)_{L^2},
$$

where

$$
\boldsymbol{\mathcal{X}}_h^n := \frac{\tau}{6}(\boldsymbol{\mathcal{X}}\xi_h^n, \xi_h^n)_{L^2} + \frac{\tau}{6}(\boldsymbol{\mathcal{X}}\zeta_h^n, \xi_h^n)_{L^2} + \frac{\tau}{6}(\boldsymbol{\mathcal{X}}\theta_h^n, \theta_h^n)_{L^2},
$$

$$
\mathbf{B}_h^n := -\frac{\tau}{3}(\mathbf{B}\xi_h^n, \xi_h^n)_{L^2} - \frac{\tau}{3}(\mathbf{B}\theta_h^n, \theta_h^n)_{L^2} - \frac{\tau}{6}(\mathbf{B}\zeta_h^n, \xi_h^n)_{L^2} - \frac{\tau}{6}(\mathbf{B}\xi_h^n, \zeta_h^n)_{L^2}.
$$

Proof. First from (3.94), we have

$$
(\zeta_h^n, \xi_h^n)_{L^2} = (\xi_h^n, \xi_h^n)_{L^2} - \tau(\mathbf{A}_h \xi_h^n, \xi_h^n)_{L^2} + \tau(\alpha_h^n, \xi_h^n)_{L^2},
$$

then

$$
\|\xi_h^n\|_{L^2}^2 = (\zeta_h^n, \xi_h^n)_{L^2} + \tau(\mathbf{A}_h \xi_h^n, \xi_h^n)_{L^2} - \tau(\alpha_h^n, \xi_h^n)_{L^2}. \tag{3.104}
$$

Next from (3.95), we have

$$
2(\theta_h^n, \zeta_h^n)_{L^2} = ((\xi_h^n + \zeta_h^n), \zeta_h^n)_{L^2} - \tau(\mathbf{A}_h \zeta_h^n, \zeta_h^n)_{L^2} + \tau(\beta_h^n, \zeta_h^n)_{L^2},
$$

and on the other hand

$$
2(\theta_h^n, \zeta_h^n)_{L^2} = \|\theta_h^n\|_{L^2}^2 - \|\theta_h^n - \zeta_h^n\|_{L^2}^2 + \|\zeta_h^n\|_{L^2}^2,
$$

then

$$\|\theta_h^n\|_{L^2}^2 \;=\; (\zeta_h^n, \xi_h^n)_{L^2} + \|\theta_h^n - \zeta_h^n\|_{L^2}^2 - \tau(\mathbf{A}_h \zeta_h^n, \zeta_h^n)_{L^2} + \tau(\beta_h^n, \zeta_h^n)_{L^2}. \quad (3.105)$$

Next rewrite (3.94) - (3.96) to

$$\theta_h^n \;=\; \zeta_h^n - \frac{\tau}{2}\mathbf{A}_h(\zeta_h^n - \xi_h^n) + \frac{\tau}{2}(\beta_h^n - \alpha_h^n) \qquad\qquad (3.106)$$

$$\xi_h^{n+1} \;=\; \theta_h^n - \frac{\tau}{3}\mathbf{A}_h(\theta_h^n - \zeta_h^n) + \frac{\tau}{3}(\gamma_h^n - \beta_h^n) \qquad\qquad (3.107)$$

then consider

$$
\begin{aligned}
\frac{1}{2}\|\xi_h^{n+1}\|_{L^2}^2 - \frac{1}{2}\|\xi_h^{n+1} - \theta_h^n\|_{L^2}^2 \;&=\; \frac{1}{2}(\xi^{n+1}, \xi^{n+1})_{L^2} - \frac{1}{2}(\xi_h^{n+1} - \theta_h^n, \xi_h^{n+1} - \theta_h^n)_{L^2} \\
&=\; (\xi_h^{n+1} - \frac{1}{2}\theta_h^n, \theta_h^n)_{L^2} \\
&=\; \frac{1}{2}\|\theta_h^n\|_{L^2}^2 + (\xi_h^{n+1} - \theta_h^n, \theta_h^n)_{L^2}
\end{aligned}
$$

then by using (3.107), we have

$$
\begin{aligned}
\frac{1}{2}\|\xi_h^{n+1}\|_{L^2}^2 - \frac{1}{2}\|\xi_h^{n+1} - \theta_h^n\|_{L^2}^2 \;=\;& \frac{1}{2}\|\theta_h^n\|_{L^2}^2 - \frac{1}{3}\tau(\mathbf{A}_h(\theta_h^n - \zeta_h^n), \theta_h^n)_{L^2} \quad (3.108) \\
&+ \frac{1}{3}\tau(\gamma_h^n - \beta_h^n, \theta_h^n)_{L^2},
\end{aligned}
$$

Next combine (3.104), (3.105) and (3.108), we have

$$
\begin{aligned}
&\frac{1}{2}\|\xi^{n+1}\|_{L^2}^2 - \frac{1}{2}\|\xi_h^{n+1} - \theta_h^n\|_{L^2}^2 - \frac{1}{2}\|\xi_h^n\|_{L^2}^2 \\
&= -\frac{1}{2}\|\xi_h^n\|_{L^2}^2 + \frac{1}{2}\|\theta_h^n\|_{L^2}^2 - \frac{1}{3}\tau(\mathbf{A}_h(\theta_h^n - \zeta_h^n), \theta_h^n)_{L^2} + \frac{1}{3}\tau(\gamma_h^n - \beta_h^n, \theta_h^n)_{L^2} \\
&= \frac{1}{2}\|\theta_h^n - \zeta_h^n\|_{L^2}^2 - \frac{1}{3}\tau(\mathbf{A}_h(\theta_h^n - \zeta_h^n), \theta_h^n)_{L^2} + \frac{\tau}{3}\tau(\gamma_h^n - \beta_h^n, \theta_h^n)_{L^2} \\
&\quad - \frac{\tau}{2}(\mathbf{A}_h\xi_h^n, \xi_h^n)_{L^2} + \frac{\tau}{2}(\alpha_h^n, \xi_h^n)_{L^2} - \frac{\tau}{2}(\mathbf{A}_h\zeta_h^n, \zeta_h^n)_{L^2} + \frac{\tau}{2}(\beta_h^n, \zeta_h^n)_{L^2}
\end{aligned}
$$

then

$$\frac{1}{2}\|\xi^{n+1}\|_{L^2}^2 - \frac{1}{2}\|\xi_h^{n+1} - \theta_h^n\|_{L^2}^2 - \frac{1}{2}\|\xi_h^n\|_{L^2}^2 \;=\; R_1 + R_2, \qquad (3.109)$$

with

$$R_1 \;=\; \frac{1}{2}\|\theta_h^n - \zeta_h^n\|_{L^2}^2 + \frac{\tau}{3}(\mathbf{A}_h\zeta_h^n, \theta_h^n - \zeta_h^n)_{L^2}, \qquad\qquad (3.110)$$

$$
\begin{aligned}
R_2 \;=\;& -\frac{\tau}{3}(\mathbf{A}_h\theta_h^n, \theta_h^n)_{L^2} - \frac{\tau}{6}(\mathbf{A}_h\zeta_h^n, \zeta_h^n)_{L^2} - \frac{\tau}{2}(\mathbf{A}_h\xi_h^n, \xi_h^n)_{L^2} \qquad (3.111) \\
&+ \frac{\tau}{3}\tau(\gamma_h^n, \theta_h^n)_{L^2} - \frac{\tau}{3}\tau(\beta_h^n, \theta_h^n)_{L^2} + \frac{\tau}{2}(\alpha_h^n, \xi_h^n)_{L^2} + \frac{\tau}{2}(\beta_h^n, \zeta_h^n)_{L^2}.
\end{aligned}
$$

Furthermore,

$$
\begin{aligned}
R_1 &= \frac{1}{2}(\theta_h^n - \zeta_h^n, \theta_h^n - \zeta_h^n + \frac{2\tau}{3}\mathbf{A}_h\zeta_h^n)_{L^2}, \\
&= \frac{1}{2}(\theta_h^n - \zeta_h^n, -\frac{1}{3}(\theta_h^n - \zeta_h^n) + \frac{2\tau}{3}(\mathbf{A}_h\xi_h^n + \beta_h^n - \alpha_h^n))_{L^2} \\
&= \frac{1}{3}(\theta_h^n - \zeta_h^n, (\xi_h^n - \zeta_h^n + \tau\beta_h^n))_{L^2} - \frac{1}{6}\|\theta_h^n - \zeta_h^n\|_{L^2}^2 \\
&= \frac{1}{3}(\theta_h^n - \zeta_h^n, \xi_h^n - \zeta_h^n)_{L^2} + \frac{\tau}{3}(\theta_h^n - \zeta_h^n, \beta_h^n)_{L^2} - \frac{1}{6}\|\theta_h^n - \zeta_h^n\|_{L^2}^2 \\
&= \frac{1}{3}(-\frac{\tau}{2}\mathbf{A}_h(\zeta_h^n - \xi_h^n) + \frac{\tau}{2}(\beta_h^n - \alpha_h^n), \xi_h^n - \zeta_h^n)_{L^2} \\
&\quad + \frac{\tau}{3}(\theta_h^n, \beta_h^n)_{L^2} - \frac{\tau}{3}(\zeta_h^n, \beta_h^n)_{L^2} - \frac{1}{6}\|\theta_h^n - \zeta_h^n\|_{L^2}^2 \\
&= \frac{\tau}{6}(\mathbf{A}_h(\xi_h^n - \zeta_h^n), \xi_h^n - \zeta_h^n)_{L^2} + \frac{\tau}{6}(\beta_h^n - \alpha_h^n, \xi_h^n - \zeta_h^n)_{L^2} \\
&\quad + \frac{\tau}{3}(\theta_h^n, \beta_h^n)_{L^2} - \frac{\tau}{3}(\zeta_h^n, \beta_h^n)_{L^2} - \frac{1}{6}\|\theta_h^n - \zeta_h^n\|_{L^2}^2
\end{aligned}
$$

by using (3.106) and (3.94), then we get

$$
\begin{aligned}
R_1 &= \frac{\tau}{6}(\mathbf{A}_h(\xi_h^n - \zeta_h^n), \xi_h^n - \zeta_h^n)_{L^2} + \frac{\tau}{3}(\alpha_h^n, \xi_h^n + \frac{1}{2}\zeta_h^n)_{L^2} - \frac{\tau}{2}(\alpha_h^n, \xi_h^n) \quad (3.112) \\
&\quad + \frac{\tau}{6}(\beta_h^n, \xi_h^n) + \frac{\tau}{3}(\theta_h^n, \beta_h^n)_{L^2} - \frac{\tau}{2}(\zeta_h^n, \beta_h^n)_{L^2} - \frac{1}{6}\|\theta_h^n - \zeta_h^n\|_{L^2}^2,
\end{aligned}
$$

Finally, we substitute R_1 and R_2 together with (3.68) from the (DG1) property that $(\mathbf{A}_h\cdot, \cdot)_{L^2} = |\cdot|_S^2 - \frac{1}{2}(\boldsymbol{\mathcal{X}}\cdot, \cdot)_{L^2} + (\mathbf{B}\cdot, \cdot)_L$, back in (3.109) then the assertion (3.103) holds. □

With the conditions that we have provided then the results of stability and convergence of the RK3-DG scheme for hdCDD can be achieved as in Burman et al. (2010) as the following results.

Lemma 3.3.4. (Burman et al., 2010, Lem.4.3)(stability) There exists a constant $c_\tau(C_S^{-1}, C_{L^*}^{-1}) > 0$ for the CFL condition that

$$
\tau \leq \frac{c_\tau h}{\sigma}, \tag{3.113}
$$

and a constant $C > 0$ such that the following property holds,

$$
\begin{aligned}
&\frac{1}{2}\|\xi_h^{n+1}\|_{L^2}^2 - \|\xi_h^n\|_{L^2}^2 + \frac{\tau}{48}|\xi_h^n|_S^2 + \frac{\tau}{12}|\zeta_h^n|_S^2 + \frac{\tau}{48}|\theta_h^n|_S^2 \quad (3.114) \\
&\qquad \leq C\tau(\tau^6 + \|\xi_\pi^n\|_*^2 + \|\zeta_\pi^n\|_*^2 + \|\theta_\pi^n\|_*^2 + \|\xi_h^n\|_{L^2}^2).
\end{aligned}
$$

Theorem 3.3.5. (Burman et al., 2010, Thm. 4.1) Assume that $\mathbf{u} \in C^4((0,T); L) \cap C^2((0,T); [H^{p+1}(\Omega)]^2)$ together with the CFL condition (3.113) then there holds,

$$
\|\mathbf{u}^N - \mathbf{u}_h^N\|_{L^2} + \Big(\sum_{n=0}^{N-1} \frac{1}{48}\tau|\mathbf{u}_h^n|_S^2 + \frac{1}{12}\tau|\mathbf{w}_h^n|_S^2 + \frac{1}{48}\tau|\mathbf{y}_h^n|_S^2 \Big)^{1/2} \tag{3.115}
$$
$$
\leq C(\tau^3 + h^{p+1/2}).
$$

4 | hdCDD Over a Single Slip

In this chapter we will discuss behaviors of the hd-CDD system over a single slip from the modeling perspective and numerical experiments. We will discuss the limitation of both the theory of hd-CDD and our standard dG method proposed in the previous chapter. The main problem for the numerical methods come from the additional dimension of line orientation that have a drawback with a large number of degrees of freedom for the dG discretization. Moreover with our proposed model of embedded slip planes in the elastic body, a standard mesh discretization will also cause a problem for mesh distribution for the parallel treatment of the numerical implementation. To overcome these two problems in the numerical method in the same time, a new type of basis functions called Finite Volume Fourier elements(FVF) is introduced. We will also discuss some of the simplified Continuum Dislocation Dynamics (sCDD) theories which are proposed to approximate the hd-CDD system by reducing the information from the line orientation dimension. Again for simplicity of presentation in this chapter, we skip the slip system index s and representative slip g.

4.1 Continuum Dislocation Dynamics

The hdCDD system (2.89) investigated in the previous chapter is not exactly written in the original form proposed by Hochrainer (2006). The original system was written with another pair of variables, i.e., dislocation density $\rho : \Gamma \times S^1 \times \mathbb{R}$ and curvature $k : \Gamma \times S^1 \times \mathbb{R}$ as the following: find $\rho = \rho(\mathbf{x}, \varphi, t)$ and $k = k(\mathbf{x}, \varphi, t)$ for a given velocity $v = v(\mathbf{x}, \varphi, t)$, by solving a system of equations:

$$\partial_t \rho = -\hat{\nabla} \cdot (\rho \mathbf{V}) + \rho v k \tag{4.1a}$$

$$\partial_t k = -\mathbf{L} \cdot \hat{\nabla}(\mathbf{L} \cdot \hat{\nabla} v) - \mathbf{V} \cdot \hat{\nabla} k - k^2 v, \tag{4.1b}$$

with the initial values ρ_0 and k_0.

However, this formulation is still only the special case of the full system that is defined on the full manifold $\mathcal{M} \subset \mathbb{R}^3$ and the line orientation space S^2 which is the

positions on the surface of unit sphere which is better explained in the recent work of Hochrainer (2015).
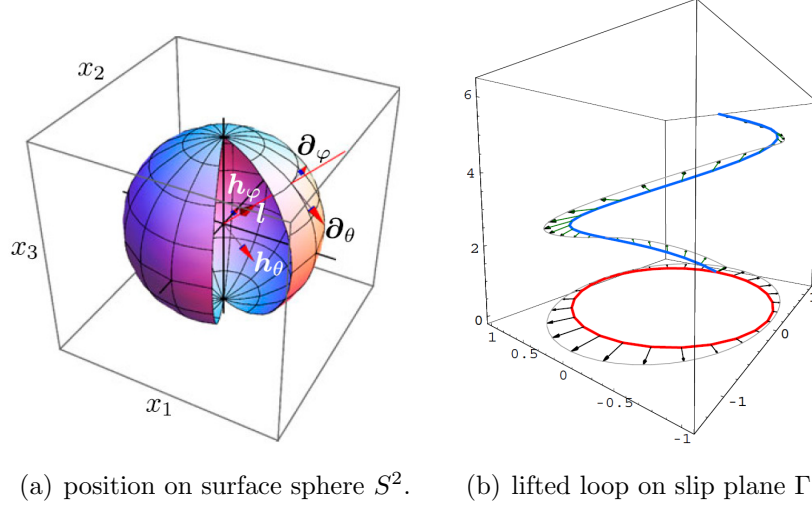
(a) position on surface sphere S^2.   (b) lifted loop on slip plane Γ.

Figure 4.1: (a): shows the manifold in $\mathbb{R}^3$ as the surface of sphere and the possible coordinate of orientation $(\varphi, \theta) \in S^2$, Hochrainer (2015); (b): shows the lifted loop as the dislocation loop on slip plane represented in higher-dimensional space $\Gamma \times S^1$, Hochrainer (2006)

For the special case the full manifold $\mathcal{M} \subset \mathbb{R}^3$ is dropped to the slip plane surface $\Gamma \subset \mathbb{R}^2$ and the line orientation on Γ is also reduced automatically to S^1. This simplification reduced the arbitrary dislocation line loop in $\mathbb{R}^3$ to the dislocation loop on the slip plane that can have representation with line orientation space as the lifted loop of dislocation as shown in Figure 4.1.

We show here that our formulation with curvature density q is equivalent to the original formulation.

Proposition 4.1.1. The equation system (4.1) has a following equivalent form:

$$\partial_t \rho = -\hat{\nabla} \cdot (\rho \mathbf{V}) + qv , \tag{4.2a}$$

$$\partial_t q = -\hat{\nabla} \cdot (q \mathbf{V}) - \rho\left(\mathbf{L} \cdot \hat{\nabla}(\mathbf{L} \cdot \hat{\nabla}v)\right) , \tag{4.2b}$$

where $q = \rho k$.

Proof. We have

$$
\begin{aligned}
\partial_t(\rho k) &= \rho\partial_t k + k\partial_t\rho \\
&= \rho\left(-\mathbf{L} \cdot \hat{\nabla}(\mathbf{L} \cdot \hat{\nabla}v) - \mathbf{V} \cdot \hat{\nabla}k - k^2 v\right) + k\left(-\hat{\nabla} \cdot (\rho \mathbf{V}) + \rho v k\right) \\
&= -\left(\rho\mathbf{V} \cdot \hat{\nabla}k + k\hat{\nabla} \cdot (\rho \mathbf{V})\right) - \rho\left(\mathbf{L} \cdot \hat{\nabla}(\mathbf{L} \cdot \hat{\nabla}v)\right) \\
&= -\hat{\nabla} \cdot (\rho k \mathbf{V}) - \rho\left(\mathbf{L} \cdot \hat{\nabla}(\mathbf{L} \cdot \hat{\nabla}v)\right)
\end{aligned}
$$

by using $\hat{\nabla} \cdot (\rho k \mathbf{V}) = \rho \mathbf{V} \cdot \hat{\nabla} k + k \hat{\nabla} \cdot (\rho \mathbf{V})$. $\qquad\qquad$ □

4.1.1 Physical Condition

With the physical condition that dislocation lines do not end inside the crystal, this leads to the equation

$$\hat{\nabla} \cdot (\rho \mathbf{L}(k)) \;\; = \;\; 0. \tag{4.3}$$

We have a proof for the special case for $v \equiv$ constant that the physical condition (4.3) can be derived from the equation (4.1).

Theorem 4.1.2. The evolution equations system

$$\partial_t \rho(x, \varphi, t) \;\; = \;\; v\mathbf{l}'(\varphi) \cdot \nabla \rho(x, \varphi, t) + vk(x, \varphi, t)\rho(x, \varphi, t) \,, \tag{4.4a}$$

$$\partial_t k(x, \varphi, t) \;\; = \;\; -vk(x, \varphi, t)^2 + v\mathbf{l}'(\varphi) \cdot \nabla k(x, \varphi, t) \,, \tag{4.4b}$$

with $\mathbf{l}(\varphi) = (\cos(\varphi), \sin(\varphi), \; \mathbf{l}'(\varphi) = \partial_\varphi \mathbf{l}(\varphi), \; v \equiv$ constant, and together with the initial condition

$$\rho_0 \;\; := \;\; \rho(x, \varphi, 0) \,,$$

$$k_0 \;\; := \;\; k(x, \varphi, 0)$$

such that

$$\hat{\nabla} \cdot (\rho_0 \mathbf{L}(k_0)) \;\; = \;\; 0.$$

Then the physical condition (4.3) holds for all $t \geq 0$.

Proof. We have

$$
\begin{aligned}
\partial_t(\rho(x, \varphi, t)k(x, \varphi, t)) \;\; &= \;\; k(x, \varphi, t)\partial_t \rho(x, \varphi, t) + \rho(x, \varphi, t)\partial_t k(x, \varphi, t) \\
&= \;\; k(x, \varphi, t)\Big(v\mathbf{l}'(\varphi) \cdot \nabla \rho(x, \varphi, t) + vk(x, \varphi, t)\rho(x, \varphi, t)\Big) \\
&\quad + \rho(x, \varphi, t)\Big(-vk(x, \varphi, t)^2 + v\mathbf{l}'(\varphi) \cdot \nabla k(x, \varphi, t)\Big) \\
&= \;\; vk(x, \varphi, t)\mathbf{l}'(\varphi) \cdot \nabla \rho(x, \varphi, t) + v\rho(x, \varphi, t)\mathbf{l}'(\varphi) \cdot \nabla k(x, \varphi, t) \\
&= \;\; v\nabla \cdot \Big(k(x, \varphi, t)\rho(x, \varphi, t)\mathbf{l}'(\varphi)\Big).
\end{aligned}
$$

Consider

$$d(x, \varphi, t) \;\; = \;\; \mathbf{l}(\varphi) \cdot \nabla \rho(x, \varphi, t) + \partial_\varphi(k(x, \varphi, t)\rho(x, \varphi, t))$$

Then, we have

$$d(x, \varphi, t) - d(x, \varphi, 0) \quad = \quad \int_0^t \partial_t d(x, \varphi, s) ds$$

with

$$
\begin{aligned}
\partial_t d(x, \varphi, t) \quad &= \quad \partial_t \Big(\mathbf{l}(\varphi) \cdot \nabla \rho(x, \varphi, t) \Big) + \partial_\varphi \Big(k(x, \varphi, t) \rho(x, \varphi, t) \Big) \\
&= \quad \mathbf{l}(\varphi) \cdot \nabla \partial_t \rho(x, \varphi, t) + \partial_\varphi \partial_t (k(x, \varphi, t) \rho(x, \varphi, t)) \\
&= \quad v \mathbf{l}(\varphi) \cdot \nabla \Big(\mathbf{l}'(\varphi) \cdot \nabla \rho(x, \varphi, t) + k(x, \varphi, t) \rho(x, \varphi, t) \Big) \\
&\quad + v \partial_\varphi \nabla \cdot \Big(k(x, \varphi, t) \rho(x, \varphi, t) \mathbf{l}'(\varphi) \Big) \\
&= \quad v \nabla \cdot \Big(k(x, \varphi, t) \rho(x, \varphi, t) \mathbf{l}(\varphi) \Big) \\
&\quad + v \partial_\varphi \nabla \cdot \Big(k(x, \varphi, t) \rho(x, \varphi, t) \mathbf{l}'(\varphi) \Big) \\
&= \quad v \nabla \cdot \Big[\partial_\varphi \Big(k(x, \varphi, t) \rho(x, \varphi, t) \Big) \mathbf{l}'(\varphi) \Big] \\
&= \quad v \nabla \cdot \Big(d(x, \varphi, t) \mathbf{l}'(\varphi) \Big)
\end{aligned}
$$

using

$$\mathbf{l}(\varphi) \cdot \nabla \Big(\mathbf{l}'(\varphi) \cdot \nabla \rho(x, \varphi, t) \Big) \quad = \quad \Delta \rho(x, \varphi, t) \mathbf{l}(\varphi) \cdot \mathbf{l}'(\varphi) \quad = \quad 0$$

and

$$
\begin{aligned}
\mathbf{l}'(\varphi) \cdot \nabla d(x, \varphi, t) \quad &= \quad \mathbf{l}'(\varphi) \cdot \nabla \Big(\mathbf{l}(\varphi) \cdot \nabla \rho(x, \varphi, t) \Big) + \mathbf{l}'(\varphi) \cdot \nabla \partial_\varphi \Big(k(x, \varphi, t) \rho(x, \varphi, t) \Big) \\
&= \quad 0 + \nabla \cdot \Big[\partial_\varphi \Big(k(x, \varphi, t) \rho(x, \varphi, t) \Big) \mathbf{l}'(\varphi) \Big].
\end{aligned}
$$

Thus, d solves a linear evolution equation subject to the initial value $d(x, \varphi, 0) \equiv 0$ and therefore has the unique solution $d(x, \varphi, t) \equiv 0$. $\square$

4.1.2 Initial values and exact solution for a single loop

We have seen in Proposition 4.1.1 that the equation system in the form of (ρ, k) is equivalent to the form of (ρ, q). Then we can provide the initial values for one form and it can be transfered to another by using the relation $q = \rho k$.

Initial values

We use a Gaussian function to approximate the dislocation loop with the following initial value functions

$$\rho(\mathbf{x}, \varphi, 0) \quad = \quad R_0 \mathrm{e}^{-\frac{\sigma}{2} r_0(\mathbf{x}, \varphi)^2}, \tag{4.5a}$$

$$k(\mathbf{x}, \varphi, 0) \;=\; \frac{1}{R_0}, \tag{4.5b}$$

where $r_0(\mathbf{x}, \varphi) = |-R_0\mathbf{l}' + \mathbf{x}_0 - \mathbf{x}| = [(R_0 \sin \varphi + x_0 - x)^2 + (-R_0 \cos \varphi + y_0 - y)^2]^{1/2}$.
We confirm the physical condition by the following proposition.

Proposition 4.1.3. For the intitial functions $\rho_0 := \rho(\mathbf{x}, \varphi, 0)$ and $k_0 := k(\mathbf{x}, \varphi, 0)$ defined in (4.5), then we have the physical condition (4.3) for the initial condition such that

$$\hat{\nabla} \cdot (\rho_0 \mathbf{L}(k_0)) \;=\; 0.$$

Proof.

$$
\begin{aligned}
\hat{\nabla} \cdot (\rho_0 \mathbf{L}(k_0)) \;&=\; \hat{\nabla} \cdot (\rho_0 \mathbf{l}, \rho_0 k_0)^\top \\
&=\; \mathbf{l} \cdot \nabla \rho_0 + k_0 \partial_\varphi \rho_0 \\
&=\; -\frac{\sigma}{2}\rho_0' \mathbf{l} \cdot \nabla r_0^2 - k_0 \frac{\sigma}{2}\rho_0' \partial_\varphi r_0^2 \\
&=\; \sigma \rho_0 \mathbf{l} \cdot [-R_0\mathbf{l}' + \mathbf{x}_0 - \mathbf{x}] - k_0 \sigma \rho_0 [-R_0\mathbf{l}' + \mathbf{x}_0 - \mathbf{x}] \cdot (-R_0\mathbf{l}'') \\
&=\; \sigma \rho_0 \mathbf{l} \cdot [\mathbf{x}_0 - \mathbf{x}] - \sigma \rho_0 \mathbf{l} \cdot [\mathbf{x}_0 - \mathbf{x}] \\
&=\; 0
\end{aligned}
$$

since $\mathbf{l}'' = -\mathbf{l}, \quad \mathbf{l} \cdot \mathbf{l}' = 0$ and $\rho_0' = \rho_0$. $\qquad\square$

Exact solution of a single loop

Proposition 4.1.4. With initial functions (4.5) we have the exact solutions of ρ and k as follow,

$$
\begin{aligned}
\rho(\mathbf{x}, \varphi, t) \;&=\; R(t)\tilde{\rho}(r(t)) \;=\; R(t)e^{-\frac{\sigma}{2}r(\mathbf{x},\varphi,t)^2}, & (4.6a) \\
k(\mathbf{x}, \varphi, t) \;&=\; \frac{1}{R(t)}, & (4.6b)
\end{aligned}
$$

where $r(\mathbf{x}, \varphi, t) = |-R(t)\mathbf{l}' + \mathbf{x}_0 - \mathbf{x}|, \quad R(t) \;=\; R_0 + vt$.

Proof. We consider the evolution equation of ρ as

$$\partial_t \rho \;=\; v\mathbf{l}' \cdot \nabla \rho + \rho k v.$$

We have

$$
\begin{aligned}
\partial_t \rho(\mathbf{x}, \varphi, t) \;&=\; R(t)\partial_t \tilde{\rho}(r(t)) + \tilde{\rho}(r(t))\partial_t R(t) \\
&=\; -R(t)\left[\frac{\sigma}{2}\tilde{\rho}(r(t))\partial_t r^2\right] + \left(\tilde{\rho}(r(t))R(t)\right)\frac{\partial_t R(t)}{R(t)}
\end{aligned}
$$

$$
\begin{aligned}
&= \ R(t)\Big[\sigma\tilde{\rho}(r(t))[-R(t)\mathbf{l}' + \mathbf{x}_0 - \mathbf{x}] \cdot (v\mathbf{l}')\Big] + \rho v k \\
&= \ (v\mathbf{l}') \cdot \Big[R(t)\sigma\tilde{\rho}(r(t))[-R(t)\mathbf{l}' + \mathbf{x}_0 - \mathbf{x}]\Big] + \rho v k \\
&= \ v\mathbf{l}' \cdot \nabla\rho + \rho v k
\end{aligned}
$$

since

$$
\begin{aligned}
\nabla\rho(\mathbf{x}, \varphi, t) &= \ R(t)\nabla\tilde{\rho}(r(t)) \\
&= \ R(t)\Big[\sigma\tilde{\rho}(r(t))[-R(t)\mathbf{l}' + \mathbf{x}_0 - \mathbf{x}]\Big].
\end{aligned}
$$

Moreover we still have the physical condition (4.3) for all $t \geq 0$ by Theorem 4.1.2. $\quad\square$

Exact solution with compact support

We can define the exact solution in (4.6a) in a more general form by choosing

$$
\tilde{\rho}(\mathbf{x}, \varphi, t) \ = \ \mathrm{e}^{-g(r(\mathbf{x},\varphi,t)^2)}, \tag{4.7}
$$

where $g(\cdot)$ is a differentiable function that has positive derivative for positive arguments and $r(\cdot)$ is defined previously. Then we can follow proofs for initial values and exact solution by using the chain rule for $\tilde{\rho}$ such that

$$
\begin{aligned}
\partial_t\tilde{\rho}(\mathbf{x}, \varepsilon, t) &= \ -2\tilde{\rho}'g'r\partial_t r(\mathbf{x}, \varphi, t) \\
\nabla\tilde{\rho}(\mathbf{x}, \varepsilon, t) &= \ -2\tilde{\rho}'g'r\nabla r(\mathbf{x}, \varphi, t) \\
\partial_\varphi\tilde{\rho}(\mathbf{x}, \varepsilon, t) &= \ -2\tilde{\rho}'g'r\partial_\varphi r(\mathbf{x}, \varphi, t).
\end{aligned}
$$

By using this generalization idea with $g(x) = \frac{1}{1-x}$, we can now define compact support solutions

$$
\rho(\mathbf{x}, \varphi, t) \ = \ \begin{cases} R(t)\mathrm{e}^{-\frac{1}{1-r(\mathbf{x},\varphi,t)^2}}, & r(\mathbf{x}, \varphi, t) < 1 \\ 0, & \text{else} \end{cases} \tag{4.8a}
$$

$$
q(\mathbf{x}, \varphi, t) \ = \ \frac{\rho}{R(t)}. \tag{4.8b}
$$

4.2 Standard RKDG Scheme

We restate the hdCDD system (3.47) here again. We have $\Omega = (0, T) \times \widetilde{\Omega}$, where $\widetilde{\Omega} := \Gamma \times S^1$ together with boundary and initial conditions as follows:

Find $\mathbf{u} = (\rho, k) : (0, T) \times \widetilde{\Omega} \to \mathbb{R}^2$ by solving

$$
\begin{aligned}
\partial_t\mathbf{u} + \mathbf{F}\mathbf{u} + \mathbf{B}\mathbf{u} &= \ \mathbf{0} \quad \text{in } (0, T) \times \widetilde{\Omega}, \\
\mathbf{u}(\cdot, t = 0) &= \ \mathbf{g} \quad \text{in } \widetilde{\Omega},
\end{aligned}
$$

$$(\mathbf{M} - \mathbf{D})\mathbf{u} \;\; = \;\; \mathbf{0} \quad \text{on } (0, T) \times \partial \widetilde{\Omega}_{S^1}$$

with periodic boundary conditions $\mathbf{u}(t, x, y, 0) = \mathbf{u}(t, x, y, 2\pi)$, $\partial \widetilde{\Omega}_{S^1} = \partial \Gamma \times S^1$ and given initial values $\mathbf{g} : \widetilde{\Omega} \to \mathbb{R}^2$.

DG Scheme

Let $W_h = \{\mathbf{w}_h \in [L^2(\widetilde{\Omega})]^2; \forall K \in \mathcal{T}_h, \mathbf{w}_h|_K \in [\mathbb{P}_p]^2\}$ be the DG space with the mesh $\mathcal{T}_h$ from the previous chapter. We define the discrete linear operators $\mathbf{A}_h : W_h \to W_h$ such that for all $(\mathbf{w}_h, \mathbf{v}_h) \in W_h \times W_h$

$$(\mathbf{A}_h \mathbf{w}_h, \mathbf{v}_h)_{L^2, K} \;\; = \;\; (\mathbf{F} \mathbf{w}_h, \mathbf{v}_h)_{L^2, K} + (\mathbf{B} \mathbf{w}_h, \mathbf{v}_h)_{L^2, K} \tag{4.9}$$

$$- \sum_{f \in \partial K} \left(\sum_{i=1}^{3} n_i^f \mathbf{F}^i \mathbf{w}_h - \mathbf{n}^f \cdot \mathbf{F}_{K, f}^{i*}(\mathbf{w}_h), \mathbf{v}_h \right)_{L^2, f}$$

with the numerical upwind flux defined as follows

$$\mathbf{n}^f \cdot \mathbf{F}_{K, f}^{*}(\mathbf{w}_h) \;\; = \;\; \sum_{i=1}^{3} n_i^f \{\!\{ \mathbf{F}^i \mathbf{w}_h \}\!\} + \frac{C_f}{2} [\![\mathbf{w}_h]\!], \tag{4.10}$$

where for a fixed common interior face f between cells K and K_f, we define the average and the jump along a normal $\mathbf{n}^f$ oriented from K to K_f as

$$\{\!\{ \mathbf{v}_h \}\!\} = \frac{\mathbf{v}_h|_K + \mathbf{v}_h|_{K_f}}{2}, \qquad [\![\mathbf{v}_h]\!] := (\mathbf{v}_h|_K - \mathbf{v}_h|_{K_f}),$$

respectively and for the normal velocity $C_f = |\mathbf{V} \cdot \mathbf{n}^f|$ where $\mathbf{V} = (-v \partial_\varphi \mathbf{l}, -\mathbf{L} \cdot \hat{\nabla} v)$ is the general velocity of hdCDD defined in (3.2).

In this step, we prepare the space discretization for the time integration by defining matrices, i.e., for $\phi_1, ..., \phi_N$ being discontinuous finite element basis of W_h,

$$\begin{aligned} \mathbb{M} &= [(\phi_i, \phi_j)]_{i,j=1,...,N} & \in \mathbb{R}^{N \times N}, \\ \mathbb{A} &= [\mathbf{A}_h(\phi_i, \phi_j)]_{i=1,...,N} & \in \mathbb{R}^{N \times N}. \end{aligned}$$

denoting the mass matrix and the non-symmetric stiffness matrix, respectively. Then we have the equations for the dG-scheme as

$$\mathbb{M} \partial_t \underline{u} + \mathbb{A} \underline{u} \;\; = \;\; \underline{0}, \tag{4.11}$$

where $\underline{u}(t) = (u_i(t))_{i=1,\ldots,N}$ is the coefficient vector at time t of the solution with respect to the dG basis corresponding to the function

$$\mathbf{u}_h(t) = \sum_{i=1}^{N} u_i(t)\phi_i \in W_h.$$

Time Discretization (Runge-Kutta)

In the previous chapter, the convergence of RK3 has been shown. However for the implementation of the numerical methods, we provide the time integration from first order to fourth order as the following,

First order RK : it is also the same formula with the explicit Euler scheme which we have

$$\underline{u}^{n+1} \ = \ \underline{u}^n - \triangle t \mathbb{M}^{-1} \mathbb{A}(\underline{u}^n)$$

For higher order Runge-Kutta schemes we have the following equations:
Second order RK :

$$
\begin{aligned}
\underline{k}_1 &= -\triangle t \mathbb{M}^{-1}\mathbb{A}(\underline{u}^n), \\
\underline{k}_2 &= -\triangle t \mathbb{M}^{-1}\mathbb{A}(\underline{u}^n + \triangle t \underline{k}_1), \\
\underline{u}^{n+1} &= \underline{u}^n + \frac{1}{2}(\underline{k}_1 + \underline{k}_2).
\end{aligned}
$$

Third order RK :

$$
\begin{aligned}
\underline{k}_1 &= -\triangle t \mathbb{M}^{-1}\mathbb{A}(\underline{u}^n), \\
\underline{k}_2 &= -\triangle t \mathbb{M}^{-1}\mathbb{A}(\underline{u}^n + \frac{1}{3}\triangle t \underline{k}_1), \\
\underline{k}_3 &= -\triangle t \mathbb{M}^{-1}\mathbb{A}(\underline{u}^n + \frac{2}{3}\triangle t \underline{k}_2), \\
\underline{u}^{n+1} &= \underline{u}^n + \frac{1}{4}(\underline{k}_1 + 3\underline{k}_3)
\end{aligned}
$$

4th order RK :

$$
\begin{aligned}
\underline{k}_1 &= -\mathbb{M}^{-1}\mathbb{A}(\underline{u}^n), \\
\underline{k}_2 &= -\mathbb{M}^{-1}\mathbb{A}(\underline{u}^n + \frac{1}{2}\triangle t \underline{k}_1), \\
\underline{k}_3 &= -\mathbb{M}^{-1}\mathbb{A}(\underline{u}^n + \frac{1}{2}\triangle t \underline{k}_2), \\
\underline{k}_4 &= -\mathbb{M}^{-1}\mathbb{A}(\underline{u}^n + \triangle t \underline{k}_3), \\
\underline{u}^{n+1} &= \underline{u}^n + \frac{1}{6}\triangle t(\underline{k}_1 + 2\underline{k}_2 + 2\underline{k}_3 + \underline{k}_4).
\end{aligned}
$$

4.2.1 Numerical Results

We simulate the expanding loop of ρ by using the intitial function $\rho_0 = \rho(t = 0)$ in (4.6a) and the exact solution $k_0 = k(t = 0)$ in (4.6b). We consider the physical condition (4.3) and the convergence of our current scheme by comparing with the exact solution. For the variables in the model problem we set $\Omega = (0,1)^2 \times (0, 2\pi)$, $R_0 = 0.2$, $\sigma = 400$, $v = 1$, $T = 0.1$ and $\triangle t = 0.001$.

First we give the information about the number of unknowns for different polynomial order and level of refinement over the domain Ω with tetrahedral mesh as below.

level l	mesh width	cells	unknowns $\mathbb{P}^1$	unknowns $\mathbb{P}^2$
2	0.0125	1,536	6,144	15,360
3	0.0625	12,288	49,152	122,880
4	0.03125	98,304	393,216	983,040
5	0.015625	786,432	3,145,728	7,864,320

Result for DG$\mathbb{P}^1$+RK1.

level l	$\|\rho_0\|_{L_2}$	$\|\rho_h^l - \rho\|_{L_\infty}$	$\|\rho_h^l - \rho\|_{L_1}$	$\|\rho_h^l - \rho\|_{L_2}$	$\sup \lvert \int_K \operatorname{div} \rho_h^l \mathbf{L} \rvert$
2	0.1317	1.4570	0.042330	0.10800	0.0186200
3	0.1328	1.1820	0.016890	0.06072	0.0049710
4	0.1329	0.6670	0.007106	0.02973	0.0011870

Result for DG$\mathbb{P}^1$+RK4.

level l	$\|\rho_0\|_{L_2}$	$\|\rho_h^l - \rho\|_{L_\infty}$	$\|\rho_h^l - \rho\|_{L_1}$	$\|\rho_h^l - \rho\|_{L_2}$	$\sup \lvert \int_K \operatorname{div} \rho_h^l \mathbf{L} \rvert$
2	0.1317	1.4540	0.042270	0.10760	0.0184800
3	0.1328	1.1820	0.016940	0.06082	0.0049100
4	0.1329	0.6695	0.007189	0.03016	0.0011830
5	0.1329	0.4308	0.002580	0.01205	0.0002266

Result for DG$\mathbb{P}^2$+RK1.

level l	$\|\rho_0\|_{L_2}$	$\|\rho_h^l - \rho\|_{L_\infty}$	$\|\rho_h^l - \rho\|_{L_1}$	$\|\rho_h^l - \rho\|_{L_2}$	$\sup \lvert \int_K \operatorname{div} \rho_h^l \mathbf{L} \rvert$
2	0.1317	1.0330	0.0181600	0.057240	0.0271100
3	0.1328	0.5332	0.0059440	0.023210	0.0065610
4	0.1329	0.3146	0.0016640	0.007629	0.0010910

Result for DG$\mathbb{P}^2$+RK4.

level l	$\|\rho_0\|_{L_2}$	$\|\rho_h^l - \rho\|_{L_\infty}$	$\|\rho_h^l - \rho\|_{L_1}$	$\|\rho_h^l - \rho\|_{L_2}$	$\sup \lvert \int_K \operatorname{div} \rho_h^l \mathbf{L} \rvert$
2	0.1317	1.0330	0.0181600	0.057240	0.0271100
3	0.1328	0.5381	0.0059350	0.023480	0.0062580
4	0.1329	0.2737	0.0014990	0.007282	0.0010820
5	0.1329	0.1282	0.0003019	0.001796	0.0001659

As the numerical results for the L_2-norm, we obtain the linear convergence for $\text{DG}\mathbb{P}^1$ and quadratic convergence for $\text{DG}\mathbb{P}^2$. These are however slower than what we expected from the results of error analysis in Chapter 3 which should be in order of $k + \frac{1}{2}$, where k is order of polynomial of DG elements with a smooth solution.

Parallel Performance

We compare the parallel performance using the first order RK with $\triangle t = 0.001$, $T = 0.1$ and polynomial order 2.

level l	unknowns	cpus	time(h:m:s.ms)	times(based 1 cpu)
4	983,040	1	1:01:59.00	1.00
		5	9:22.16	6.62
		10	4:48.05	12.91
		20	2:30.40	17.68
		40	1:18.60	47.32
		80	0:40.91	90.90

For level 5, we have stability problems of the scheme for $\triangle t = 0.001$, therefore we change the time step to $\triangle t = 0.0001$ with the same $T = 0.1$. This result with totally 1000 time steps.

level l	unknowns	cpus	time(h:m:s.ms)
5	7,864,320	80	51:28.00

Alternativly, we use higher order RK with larger time step, then we try to use 4th order RK with $\triangle t = 0.001$. We can get a stable result within about 16 minutes on 80 processors. We plot ρ_h at $t = 0$ and $t = 0.1$ for mesh level 4 and 5 as follows,

(a) $\rho_h^4(t=0)$ (b) $\rho_h^4(t=0.1)$

(c) top view of $\rho_h^4(t=0)$ (d) top view of $\rho_h^4(t=0.1)$

Figure 4.2: Plots of ρ_h^4 at $t=0$ and $t=0.1$ for mesh level 4.

(a) $\rho_h^5(t=0)$ (b) $\rho_h^5(t=0.1)$

(c) top view of $\rho_h^5(t=0)$ (d) top view of $\rho_h^5(t=0.1)$
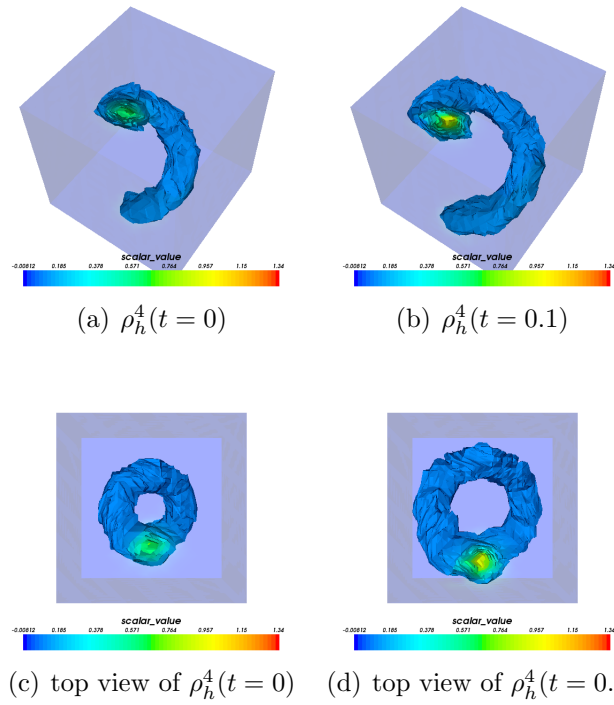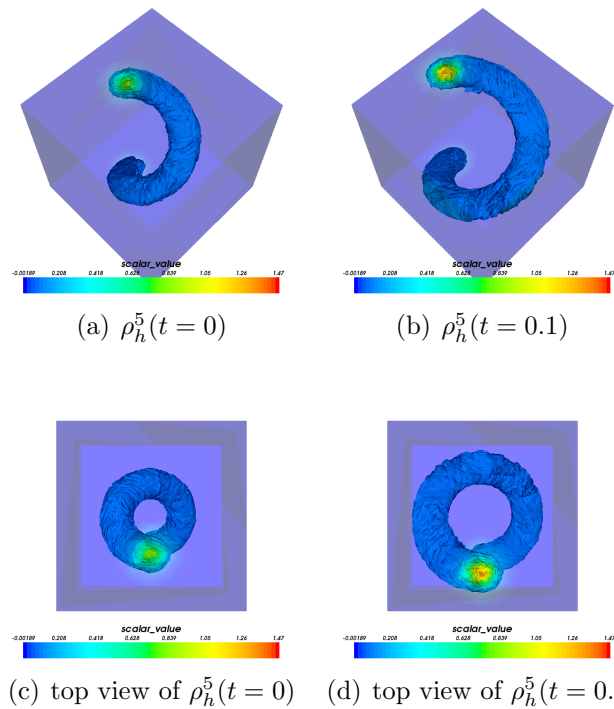
Figure 4.3: Plots of ρ_h^5 at $t=0$ and $t=0.1$ for mesh level 5.

In the next step for the elasto-plasticity model, this simulation of hdCDD has to provide the required information for the elasticity problem, see Chapter 2.

(a) ρ_h (b) ρ_{tot} (c) plastic slip γ
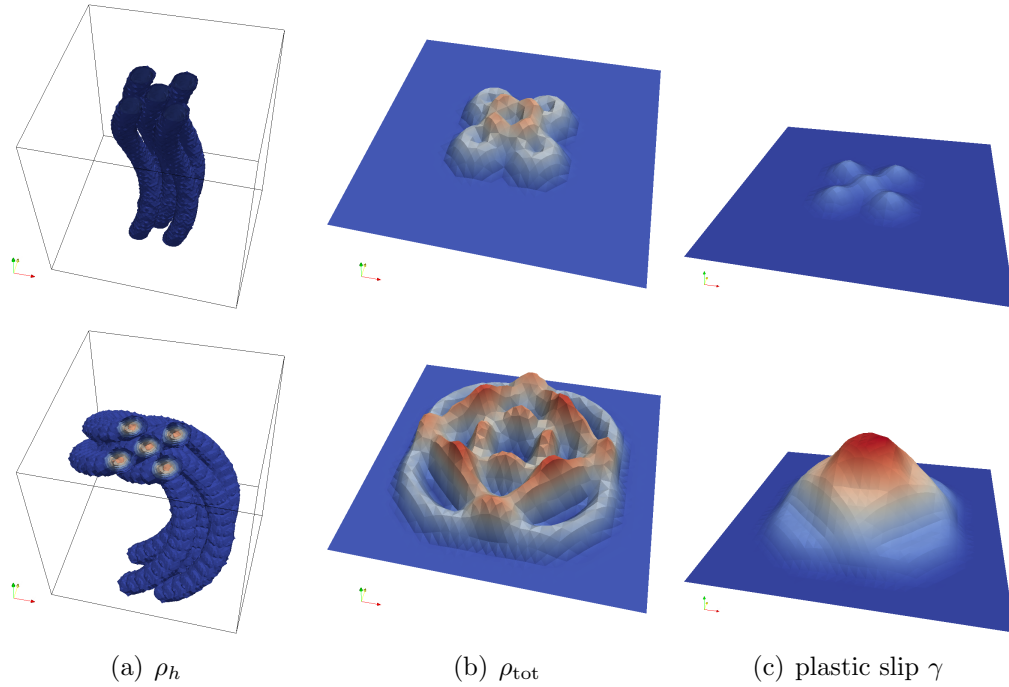
Figure 4.4: Plots of evolution of multi-loops for dislocation density has been shown in (a); (b) shows the total dislocation density; and (c) shows the plastic slip that can be seen as the accumulated number of dislocations passed through each area of slip plane.

The Figure 4.4 shows the total dislocation densitiy $\rho^{\text{tot}} = \int_0^{2\pi} \rho(\varphi)\,\mathrm{d}\varphi$ that influence the velocity of dislocations itself and the plastic slip γ computed from Orowan's equation that is needed later to compute plastic distorsion $\boldsymbol{\beta}^{\text{pl}}$ where the exact solution with compact support (4.8a) of hdCDD has been used as initial values for the simulation to avoid overlap of each loop. These procedures on the parallel setting are however not a trivial task due to the communication needed for the integration over one direction of the line orientation φ. This can be more complex with the system of muli-slip planes on the full elasto-plasticity setting. To overcome this problem a new type of basis function for the DG scheme will be used as can be seen in the next section.

4.3 Finite Volume Fourier Element

The motivation for developing and using a new basis family for DG schemes can be started by considering the problem of mesh distribution in Figure 4.5 for the embedded slip planes over the elastic body in order to provide the parallel computation. As we have seen before that the hdCDD system introduces a additional dimension for the line orientation which is not shown here. The slip planes are constructed in such a way they lines on faces of the discretized elements of the elastic body. Then after distribute sub-domain for elastic problem, this can cause a very tricky method to treat the line orientation dimension for the slip planes.

(a) Elasticbody with
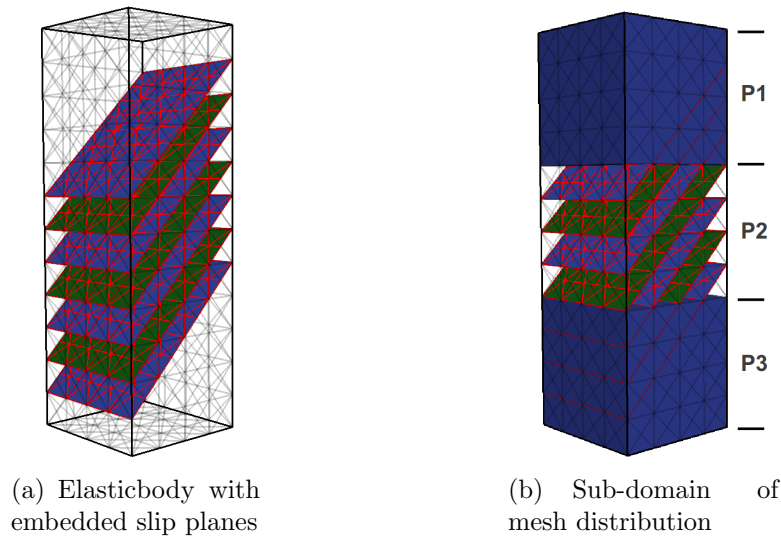embedded slip planes

(b) Sub-domain of
mesh distribution

Figure 4.5: (a): shows the multi-slip planes system over the elastic body with the
absence of the orientation dimension; (b): shows the area of sub-domains
that can be distributed to different processors

It would be a very good idea, if we can provide the basis functions in such a way that
we do not have to worry about the distribution and communication over the direction
φ. To achieve this we use the benefit of the DG methods that allows us to construct
discontinuous basis function on a more general element. We start by discretizing the
higher-dimensional domain $\Gamma \times [0, 2\pi]$ by triangular prisms as in Figure 4.6. Then
using the benefit of our problem that has the periodic boundary on φ direction by
using the Fourier basis over this direction together with polynomial function over
the triangle based of the element. The tensor product of the polynomial and Fourier
functions provide a new possibility for us to handle our problems. In this thesis only
the polynomial order 0 is considered, therefore we named this new basis functions
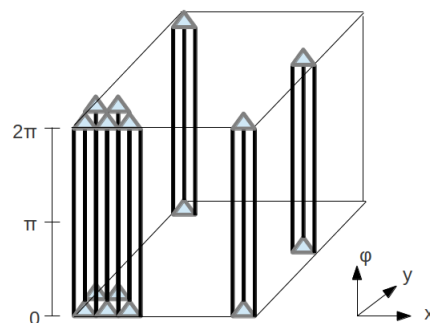over the triangular prism as *the Finite Volume Fourier Element*.

Figure 4.6: Mesh discretization with triangular prism.

Fourier basis Functions

We use the Fourier series such that for f is the periodic function over $[0, 2\pi)$ we have

$$f(\varphi) = \frac{1}{\sqrt{2}} a_0 + \sum_{n=1}^{\infty} a_n \sin(n\varphi) + \sum_{n=1}^{\infty} b_n \cos(n\varphi).$$

Together with the orthogonality properties

$$\int_0^{2\pi} \sin(n\varphi) \sin(m\varphi) d\varphi = \pi \delta_{mn}, \quad \int_0^{2\pi} \cos(n\varphi) \cos(m\varphi) d\varphi = \pi \delta_{mn}, \quad n, m \in \mathbb{Z}$$

$$\int_0^{2\pi} \sin(n\varphi) \cos(m\varphi) d\varphi = 0, \quad\quad\quad\quad\quad\quad\quad\quad\quad\quad n \neq m$$

$$\int_0^{2\pi} \sin(n\varphi) d\varphi = \int_0^{2\pi} \cos(n\varphi) d\varphi = 0, \quad\quad\quad\quad\quad n \neq 0.$$

We can then calculate coefficients a_0, a_n, b_n as

$$a_0 = \frac{1}{\sqrt{2}\pi} \int_0^{2\pi} f(\varphi) d\varphi,$$

$$a_n = \frac{1}{\pi} \int_0^{2\pi} f(\varphi) \sin(n\varphi) d\varphi,$$

$$b_n = \frac{1}{\pi} \int_0^{2\pi} f(\varphi) \cos(n\varphi) d\varphi.$$

This leads to the approximation of the periodic function f such that for a given $n_f \in \mathbb{N}$

$$f(\varphi) \approx \frac{1}{\sqrt{2}} a_0 + \sum_{n=1}^{n_f} a_n \sin(n\varphi) + \sum_{n=1}^{n_f} b_n \cos(n\varphi). \quad\quad (4.12)$$

Later we will use the set of trigonometric functions as Fourier basis functions

$$\begin{aligned} \mathcal{F} &= \{\frac{1}{\sqrt{2}}, \sin(n\varphi), \cos(n\varphi) \mid n = 1, ..., n_f, \varphi \in [0, 2\pi)\} \quad\quad (4.13) \\ &= \{\Psi_n \mid n = 1, ..., N_f\} \end{aligned}$$

with property

$$\int_0^{2\pi} \Psi_n(\varphi) \Psi_m(\varphi) d\varphi = \pi \delta_{mn},$$

where Ψ_i are re-numbering functions of trigonometric functions and $N_f = 2n_f + 1$.

4.3.1 Finite Volume Fourier Element

Finite Volume Fourier Shape Functions

We consider shape functions over the triangular prism by using the product of $\mathbb{P}^0$ polynomial and Fourier basis function as follows,

$$\hat{\phi}_n(\mathbf{x}, \varphi) \;=\; 1\Psi_n(\varphi)\,, \qquad \Psi_n \in \mathcal{F}, \quad \mathbf{x} \in \hat{T}, \varphi \in [0, 2\pi),$$

where Ψ_n, $n = 1, ..., N_f$ are Fourier basis functions defined in previous section. Moreover define the space

$$\mathbb{FVF}^n(\hat{K}) \;:=\; \operatorname{span}\{\hat{\phi}_n(\mathbf{x}, \varphi), \quad (\mathbf{x}, \varphi) \in \hat{K} := \hat{T} \times [0, 2\pi)\}. \qquad (4.14)$$

Interpolation

We approximate the function $u(\mathbf{x}, \varphi) : T \times [0, 2\pi) \to \mathbb{R}$ as

$$\begin{aligned}
u(\mathbf{x}, \varphi) &\approx \sum_n \alpha_n \phi_n(\mathbf{x}, \varphi), \\
&= \sum_n \alpha_n \Psi_n(\varphi),
\end{aligned}$$

then

$$\begin{aligned}
\int_T \int_0^{2\pi} u(\mathbf{x}, \varphi) \Psi_n(\varphi)\, \mathrm{d}\varphi \mathrm{d}\mathbf{x} &= \int_T \int_0^{2\pi} \left(\sum_m \alpha_m \Psi_m(\varphi)\right) \Psi_n(\varphi)\, \mathrm{d}\varphi \mathrm{d}\mathbf{x} \\
&= \alpha_n \int_T 1 d\mathbf{x} \int_0^{2\pi} \Psi_n(\varphi) \Psi_n(\varphi)\, \mathrm{d}\varphi \\
&= \alpha_n \pi |T|
\end{aligned}$$

where $|T|$ is the area of the triangle T. And so we have

$$\alpha_n \;=\; \frac{1}{\pi |T|} \int_T \int_0^{2\pi} u(\mathbf{x}, \varphi) \Psi_n(\varphi)\, \mathrm{d}\varphi \mathrm{d}\mathbf{x}.$$

DG Scheme

Define the discretized space

$$W_h^{\mathrm{FVF}} := \{\phi \in [L_2(\Gamma \times (0, 2\pi))]^2 \mid \forall K \in \mathcal{T}_h, \ \phi|_K \in [\mathbb{FVF}^n(K)]^2\},$$

where K is the physical triangular prism with $K = T \times [0, 2\pi]$, T a triangle in Γ.

Let $\mathbf{u}_h \in W_h^{\text{FVF}}$, then similar to (4.9) for a fixed $K \in \mathcal{T}_h$ by separate the integration over T and $[0, 2\pi]$ we have

$$
\int_T \left(\int_0^{2\pi} \partial_t \mathbf{u}_h^K \phi^K \, d\varphi \right) d\widetilde{\mathbf{x}} = \sum_{i=1}^3 \left[\int_T \left(\int_0^{2\pi} (\mathbf{F}^i \mathbf{u}_h^K) \partial_i \phi^K \, d\varphi \right) d\widetilde{\mathbf{x}} \right. \tag{4.15}
$$
$$
\left. - \int_{\partial T} \left(\int_0^{2\pi} n_i (\mathbf{F}^{*i} \mathbf{u}_h) \phi^K \, d\varphi \right) d\widetilde{\mathbf{a}} \right]
$$
$$
- \int_T \left(\int_0^{2\pi} (\mathbf{B} \mathbf{u}_h^K) \phi^K \, d\varphi \right) d\widetilde{\mathbf{x}},
$$

where $\widetilde{\mathbf{x}} = (\mathbf{x}, \varphi) \in T \times (0, 2\pi)$, $\widetilde{\mathbf{a}}$ is surface over this setting. We perform the integration in φ direction directly into the scheme, then it will left only the integration over triangle T that has to be done numerically. The matrix representations and the time integration can be performed similarly to the previous section.

4.3.2 Numerical Results

We again use the exact solutions with compact support of ρ and ρk with a given $v \equiv const$. We set for one loop solution with $R_0 = 0.15$, $\sigma^2 = 200$ and we have $\|\mathbf{u}(t = 0)\|_{L_2} = 1.115$. We first check the interpolation based on n_f by using fixed refinement level 5 for $\mathcal{T}$ with $\mathbf{u}_h$ is the interpolation of $\mathbf{u}$.

n_f	$\|\mathbf{u}_h - \mathbf{u}\|_{L_2}$	factor	DoFs
0	1.002e-00	-	8,192
5	4.517e-01	2.22	90,112
10	2.355e-01	1.93	172,032
15	2.164e-01	1.08	253,952
20	2.130e-01	1.02	335,872

We do further check the interpolation based on various levels by using fixed $n_f = 20$.

level	$\|\mathbf{u}_h - \mathbf{u}\|_{L_2}$	factor	DoFs
3	6.710e-01	-	20,992
4	3.942e-01	1.70	83,968
5	2.130e-01	1.85	335,872
6	1.139e-01	1.87	1,343,488
7	6.555e-02	1.74	5,373,952

Comparing with the FV scheme, $\|\mathbf{u}_h - \mathbf{u}\|_{L_2} = 3.060\text{e-}02$ for the interpolation at level 5 with 1,572,864 DoFs. The degrees of freedom have been reduced about 5 times, but however with a trade off of a less accurate approximation. The analysis of the convergence rate of this interpolation is still missing in this work. However, we observe that the convergence of the interpolation of FVF element with fixed $n_f = 20$ is almost linear.

Time Evolution

We now consider the time evolution by setting $R_0 = 0.15$, $\sigma^2 = 200$, $T = 0.2$ and $n_f = 20$ with $\|\mathbf{u}(t = 0.2)\|_{L_2} = 1.169$.

level	$\|\mathbf{u}_h - \mathbf{u}\|_{L_2}$	factor	time (h:m:s.ms)	proc. cores
3	1.068e-00	-	0:8.98	16
4	9.753e-01	1.09	0:33.16	16
5	8.243e-01	1.18	2:10.63	16
6	6.214e-01	1.33	8:45.53	16
7	4.283e-01	1.45	12:04.08	48

Comparing with the DG$\mathbb{P}^1$ scheme in previous section, $\|\mathbf{u}_h - \mathbf{u}\|_{L_2} = 8.989\text{e-}01$ for the result of simulation at level 5. For the convergence rate of the results, it is obviously slower than the rate of interpolation. Therefore, with the lacking of numerical analysis, we may approximate the convergence rate to be sub-optimal by using these numerical results.
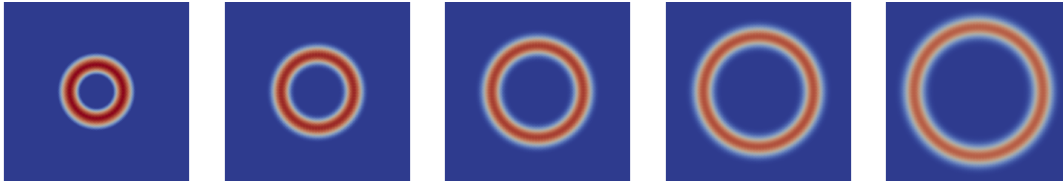
Figure 4.7: Evolution of $\rho^{tot} := \int_0^{2\pi} \rho(\varphi)\, d\varphi$ at level 7

Boundary Condition Results

Finally after comparing the simulation to show the convergent results of the numerical scheme, we are now ready to test it with boundary conditions.

We set $R_0 = 0.15$, $\sigma^2 = 200$, $T = 0.7$ and $n_f = 15$.
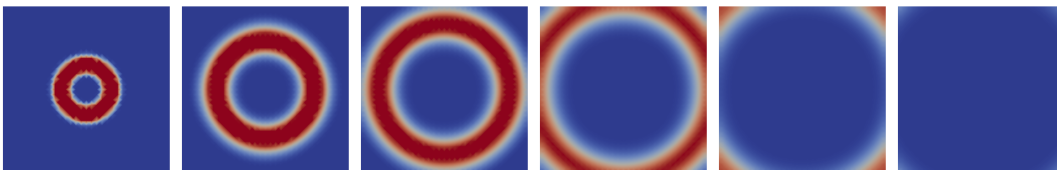
Open Boundary

Figure 4.8: Evolution of ρ^{tot} with open boundary condition in level 5.
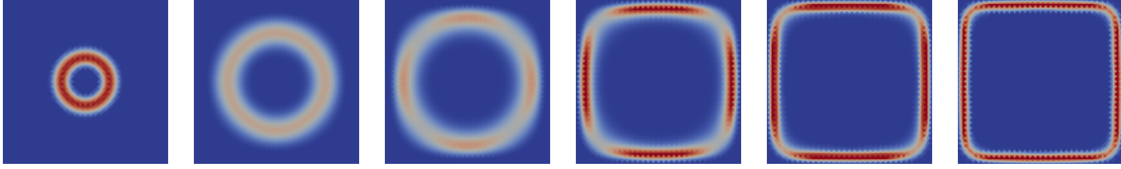
Impenetrable Boundary

Figure 4.9: Evolution of ρ^{tot} with impenetrable boundary condition at level 5.
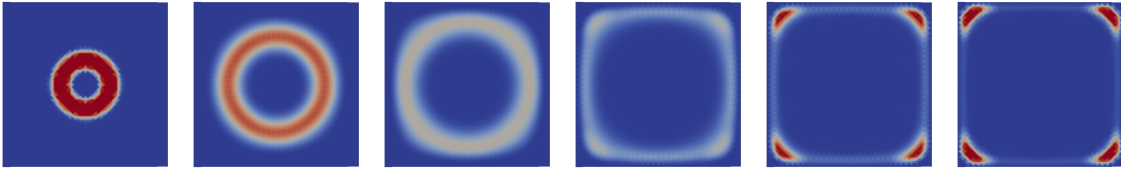

Figure 4.10: Evolution of q^{tot} with impenetrable boundary condition at level 5.

4.4 Simplified CDD Models

In previous section, the new type of DG basis has been proposed to reduce the degree of freedoms over a single slip plane. Another possiblility is to develop further theory that approximate the hdCDD system directly in the equation. The work has been already proposed by Hochrainer and coworkers (Hochrainer et al. (2009); Sandfeld et al. (2011); Hochrainer et al. (2013); Monavari et al. (2014); Hochrainer (2015)) after the achievement of the first numerical results carried out by Sandfeld (2010a); Sandfeld et al. (2011). Here, we give an example for the possibility to simplify the system by introducing additional constitutive equations to the system.

In order to give a clear presentation of the development of the sCDD system, we divide the derivation into several steps over the domain $\Gamma \in \mathbb{R}^2 \times \{0\}$, $\mathbf{b} = (1,0,0)^\top$ and the normal of the slip plane $\mathbf{m} = (0,0,1)^\top$.

Step 1: Full CDD

We start by considering the full system;

$$\partial_t \rho = -\hat{\nabla} \cdot (\rho \mathbf{V}) + qv, \tag{4.16a}$$

$$\partial_t q = -\hat{\nabla} \cdot (q \mathbf{V}) - \rho \Big(\mathbf{L} \cdot \hat{\nabla} (\mathbf{L} \cdot \hat{\nabla} v) \Big). \tag{4.16b}$$

Step 2: Apply assumption $\partial_\varphi v = 0$

We consider the system under an assumption that $\partial_\varphi v = 0$ then we can write these equations in more details as follows

$$
\begin{aligned}
\partial_t \rho &= -\nabla(\rho v \mathbf{l}^\perp) + \partial_\varphi(\rho \mathbf{l} \cdot \nabla v) + \rho k v \\
&= -\partial_x(\rho v \sin\varphi) + \partial_y(\rho v \cos\varphi) + \partial_\varphi\Big(\rho\cos\varphi \partial_x v + \rho\sin\varphi \partial_y v\Big) + qv
\end{aligned}
$$

and

$$
\begin{aligned}
\partial_t q &= -\nabla(\rho v \mathbf{l}^\perp) + \partial_\varphi(\rho \mathbf{l} \cdot \nabla v) - \rho(\mathbf{l} \cdot \nabla(\mathbf{l} \cdot \nabla v)) + q\mathbf{l}^\perp \cdot \nabla v) \\
&= -\partial_x(q v \sin\varphi) + \partial_y(q v \cos\varphi) + \partial_\varphi\Big(q\cos\varphi \partial_x v + q\sin\varphi \partial_y v\Big) \\
&\quad - \rho\Big(\cos^2\varphi \partial_x^2 v + 2\sin\varphi\cos\varphi \partial_x \partial_y v + \sin^2\varphi \partial_y^2 v\Big) + q\Big(\sin\varphi \partial_x v - \cos\varphi \partial_y v\Big) \\
&= -\partial_x(q v \sin\varphi) + \partial_y(q v \cos\varphi) + \partial_\varphi\Big(q\cos\varphi \partial_x v + q\sin\varphi \partial_y v\Big) \\
&\quad - \frac{\rho}{2}\Big((\partial_x^2 v + \partial_y^2 v) + \cos 2\varphi(\partial_x^2 v - \partial_y^2 v) + 2\sin 2\varphi \partial_x \partial_y v\Big) + q\Big(\sin\varphi \partial_x v - \cos\varphi \partial_y v\Big)
\end{aligned}
$$

by using identities

$$
\sin 2\varphi = 2\sin\varphi\cos\varphi, \qquad \cos 2\varphi = 2\cos^2\varphi - 1.
$$

Finally we have

$$
\begin{aligned}
\partial_t \rho &= -\partial_x(\rho v \sin\varphi) + \partial_y(\rho v \cos\varphi) + \partial_\varphi\Big(\rho\cos\varphi \partial_x v + \rho\sin\varphi \partial_y v\Big) + qv \\
\partial_t q &= -\partial_x(q v \sin\varphi) + \partial_y(q v \cos\varphi) + \partial_\varphi\Big(q\cos\varphi \partial_x v + q\sin\varphi \partial_y v\Big) \\
&\quad - \frac{\rho}{2}\Big((\partial_x^2 v + \partial_y^2 v) + \cos 2\varphi(\partial_x^2 v - \partial_y^2 v) + 2\sin 2\varphi \partial_x \partial_y v\Big) \\
&\quad + q\Big(\sin\varphi \partial_x v - \cos\varphi \partial_y v\Big)
\end{aligned}
$$

Step 3: Perform an integration on φ direction

We reduce the Full CDD to sCDD by doing the integration on φ direction, so we have

$$
\begin{aligned}
\partial_t \rho^t &= \int_0^{2\pi} \Big(-\partial_x(\rho v \sin\varphi) + \partial_y(\rho v \cos\varphi) + \partial_\varphi\Big(\rho\cos\varphi \partial_x v + \rho\sin\varphi \partial_y v\Big) + qv\Big) d\varphi \\
&= -\partial_x(v\rho_{s1}) + \partial_y(v\rho_{c1}) + q^t v \tag{4.17}
\end{aligned}
$$

and

$$
\partial_t q^t = \int_0^{2\pi} \Big[-\partial_x(q v \sin\varphi) + \partial_y(q v \cos\varphi) + \partial_\varphi\Big(q\cos\varphi \partial_x v + q\sin\varphi \partial_y v\Big)
$$

$$-\frac{\rho}{2}\Big((\partial_x^2 v + \partial_y^2 v) + \cos 2\varphi(\partial_x^2 v - \partial_y^2) + 2\sin 2\varphi \partial_x \partial_y v\Big) \tag{4.18}$$

$$+q\Big(\sin \varphi \partial_x v - \cos \varphi \partial_y v\Big)\Big] d\varphi$$

$$= \quad -\partial_x(vq_{s1}) + \partial_y(vq_{c1}) + q_{s1}\partial_x v - q_{c1}\partial_x v$$

$$-\frac{1}{2}\Big(\rho^t(\partial_x^2 v + \partial_y^2 v) + \rho_{c2}(\partial_x^2 v - \partial_y^2 v) + 2\rho_{s2}\partial_x \partial_y v\Big)$$

where

$$q_{c1} \quad := \quad \int_0^{2\pi} q \cos \varphi d\varphi, \qquad q_{s1} \quad := \quad \int_0^{2\pi} q \sin \varphi d\varphi,$$

$$\rho_{c1} \quad := \quad \int_0^{2\pi} \rho \cos \varphi d\varphi, \qquad \rho_{s1} \quad := \quad \int_0^{2\pi} \rho \sin \varphi d\varphi,$$

$$\rho_{c2} \quad := \quad \int_0^{2\pi} \rho \cos 2\varphi d\varphi, \qquad \rho_{s2} \quad := \quad \int_0^{2\pi} \rho \sin 2\varphi d\varphi.$$

We now have 6 new variables in addition to the equations of ρ and q then we need consititutive relations to be able to solve the problem.

Step 4: Constitutive Equations

Assumptions

Define a new angular variable $\varphi_G := \arctan(\rho_{s1}/\rho_{c1})$ and in particular with $\rho^G := \sqrt{\rho_{c1}^2 + \rho_{s1}^2}$ then it follows

$$\cos \varphi_G \quad = \quad \rho_{c1}/\rho_G, \quad \sin \varphi_G \quad = \quad \rho_{s1}/\rho_G$$

and this leads to

$$\rho_{c1} \quad = \quad \rho^G \cos \varphi_G, \quad \rho_{s1} \quad = \quad \rho^G \sin \varphi_G.$$

Then apply this idea further to approximate ρ_{c2} and ρ_{s2} with

$$\rho_{c2} \quad \approx \quad \rho^G \cos 2\varphi_G \quad = \quad \rho^G(2\cos^2 \varphi_G - 1) \quad = \quad \frac{2\rho_{c1}^2}{\rho_G} - \rho_G, \tag{4.19}$$

$$\rho_{s2} \quad \approx \quad \rho^G \sin 2\varphi_G \quad = \quad \rho^G(2\sin \varphi_G \cos \varphi_G) \quad = \quad \frac{2\rho_{c1}\rho_{s1}}{\rho^G}. \tag{4.20}$$

For the variables q_{c1} and q_{s1} we will use the approximation

$$q_{c1} \quad = \quad \int_0^{2\pi} \frac{\rho^2 k \cos \varphi}{\rho} d\varphi \tag{4.21}$$

$$= \quad \int_0^{2\pi} \frac{(\rho \cos \varphi)(\rho k)}{\rho} d\varphi$$

$$\approx \quad \frac{\int_0^{2\pi}(\rho\cos\varphi)d\varphi \int_0^{2\pi}(\rho k)d\varphi}{\int_0^{2\pi}\rho d\varphi}$$

$$= \quad \frac{\rho_{c1}q^t}{\rho^t}.$$

Similarly we have

$$q_{s1} \quad = \quad \int_0^{2\pi}\frac{\rho^2 k\sin\varphi}{\rho}d\varphi \qquad \approx \quad \frac{\rho_{s1}q^t}{\rho^t}. \tag{4.22}$$

With these estimations we can reduce the new variables from 6 to 2 variables, ρ_{c1} and ρ_{s1}. We will keep these two variables and find their evolution equations.

To complete the model we use the assumption from Sandfeld (2010b) that

$$\boldsymbol{\alpha} \quad = \quad \int_0^{2\pi}\rho\mathbf{l}\otimes\mathbf{b}d\varphi \quad = \quad (\rho_{c1},\rho_{s1},0)^\top\otimes\mathbf{b},$$

$$\partial_t\boldsymbol{\beta}^{pl} \quad = \quad -\int_0^{2\pi}\rho v(\mathbf{l}^\perp\times\mathbf{l})\otimes\mathbf{b}d\varphi \quad = \quad (\rho^t v\mathbf{m})\otimes\mathbf{b},$$

where $\mathbf{m}$ is the normal of slip plane and in this case we have $\mathbf{m} = (0,0,1)^\top$.

Together with the relationship

$$\boldsymbol{\alpha} \quad = \quad \nabla\times\boldsymbol{\beta}^{pl},$$

then we have

$$\partial_t\boldsymbol{\alpha} \quad = \quad (\partial_t\rho_{c1},\partial_t\rho_{s1},0)^\top\otimes\mathbf{b}$$

and

$$\partial_t\nabla\times\boldsymbol{\beta}^{pl} \quad = \quad \nabla\times\partial_t\boldsymbol{\beta}^{pl} \quad = \quad (\nabla\times\rho^t v\mathbf{m})\otimes\mathbf{b} \quad = \quad (\partial_y(\rho^t v),-\partial_x(\rho^t v),0)^\top\otimes\mathbf{b}.$$

Finally we obtain an additional evolution system for ρ_{c1} and ρ_{s1}

$$\partial_t\rho_{c1} \quad = \quad \partial_y(\rho^t v) \tag{4.23a}$$

$$\partial_t\rho_{s1} \quad = \quad -\partial_x(\rho^t v). \tag{4.23b}$$

Step 5: Finalize the sCDD system

We substitute the constitutive equations (4.19), (4.20), (4.21), (4.22) into (4.18) then we have

$$\partial_t q^t \quad = \quad -\partial_x(vq_{s1}) + \partial_y(vq_{c1}) + q_{s1}\partial_x v - q_{c1}\partial_x v \tag{4.24}$$

$$-\frac{1}{2}\Big(\rho^t(\partial_x^2 v + \partial_y^2 v) + \rho_{c2}(\partial_x^2 v - \partial_y^2) + 2\rho_{s2}\partial_x\partial_y v\Big)$$

$$= -v\partial_x(q_{s1}) + v\partial_y(q_{c1}) - \frac{1}{2}\Big(\rho^t(\partial_x^2 v + \partial_y^2 v) + \rho_{c2}(\partial_x^2 v - \partial_y^2) + 2\rho_{s2}\partial_x\partial_y v\Big)$$

$$= -v\partial_x(\frac{q^t\rho_{s1}}{\rho^t}) + v\partial_y(\frac{q^t\rho_{c1}}{\rho^t}) - \frac{1}{2}\Big(\rho^t(\partial_x^2 v + \partial_y^2 v) + (\frac{2\rho_{c1}^2}{\rho^G} - \rho^G)(\partial_x^2 v - \partial_y^2 v)\Big)$$

$$-2\frac{\rho_{c1}\rho_{s1}}{\rho^G}\partial_x\partial_y v.$$

Finally by combining this with (4.17), (4.23) we have the equations system for F-sCDD as follows

$$\partial_t \rho^t = -\partial_x(v\rho_{s1}) + \partial_y(v\rho_{c1}) + vq \tag{4.25a}$$

$$\partial_t \rho_{c1} = \partial_y(v\rho^t) \tag{4.25b}$$

$$\partial_t \rho_{s1} = -\partial_x(v\rho^t) \tag{4.25c}$$

$$\partial_t q^t = -v\partial_x(\frac{q^t\rho_{s1}}{\rho^t}) + v\partial_y(\frac{q^t\rho_{c1}}{\rho^t}) - \frac{1}{2}\Big(\rho^t(\partial_x^2 v + \partial_y^2 v) \tag{4.25d}$$

$$+ (\frac{2\rho_{c1}^2}{\rho^G} - \rho^G)(\partial_x^2 v - \partial_y^2 v)\Big) - 2\frac{\rho_{c1}\rho_{s1}}{\rho^G}\partial_x\partial_y v.$$

Moreover, we can further rewite this in a more compact form by introducing

$$\boldsymbol{\kappa} = (\rho_{c1}, \rho_{s1}, 0)^\top, \tag{4.26}$$

then (4.25b) and (4.25c) can be reformulated to

$$\partial_t \boldsymbol{\kappa} = \nabla \times (v\rho^t \mathbf{m}). \tag{4.27}$$

For the conservative form one should rewrite the evolution of q^t as

$$\partial_t q^t = -\partial_x(v\frac{q^t\rho_{s1}}{\rho^t}) + \partial_y(v\frac{q^t\rho_{c1}}{\rho^t}) + f(\rho^t, \rho_{c1}, \rho_{s1}, q^t) \tag{4.28}$$

where

$$f(\rho^t, \rho_{c1}, \rho_{s1}, q^t) = \frac{q^t\rho_{s1}}{\rho^t}\partial_x v - \frac{q^t\rho_{c1}}{\rho^t}\partial_y v - \frac{1}{2}\Big(\rho^t(\partial_x^2 v + \partial_y^2 v) + (\frac{2\rho_{c1}^2}{\rho^G} - \rho^G)(\partial_x^2 v - \partial_y^2 v)\Big)$$

$$-2\frac{\rho_{c1}\rho_{s1}}{\rho^G}\partial_x\partial_y v.$$

Conservative Form

In order to provide the system in the general framework, say nonlinear conservative form, we rewrite (4.25) in the form of equation

$$\partial_t \mathbf{u} + \sum_{i=1}^{2} \partial_i (\mathbf{F}^i(\mathbf{u})(\mathbf{u})) + \mathbf{b}(\mathbf{u}) = \mathbf{0} \quad \text{in } \mathbf{\Omega} \subset \mathbb{R}^2, \tag{4.29}$$

here $(\partial_i)_{i=1,2} = (\partial_x, \partial_y)^\top$, $\mathbf{u} = (\rho^t, \rho_{c1}, \rho_{s1}, q^t)^\top$. Then we have

$$\mathbf{F}^1(\mathbf{u}) = \begin{bmatrix} 0 & 0 & v & 0 \\ 0 & 0 & 0 & 0 \\ v & 0 & 0 & 0 \\ 0 & 0 & 0 & \frac{v\rho_{s1}}{\rho^t} \end{bmatrix}, \quad \mathbf{F}^2(\mathbf{u}) = \begin{bmatrix} 0 & -v & 0 & 0 \\ -v & 0 & 0 & 0 \\ 0 & 0 & 0 & 0 \\ 0 & 0 & 0 & -\frac{v\rho_{c1}}{\rho^t} \end{bmatrix}, \quad \mathbf{b}(\mathbf{u}) = \begin{pmatrix} -vq \\ 0 \\ 0 \\ -f(\mathbf{u}) \end{pmatrix}.$$

With this new simplified-CDD system that provides an approximation of hdCDD, the cost of numerical methods can be massively reduced by avoiding the computation on the additional orientation dimension by introducing two additional variables and resulting in a nonlinear system.

5 | 2D Coupled System

In this chapter we consider the fully coupled system for the 2D setting that already has been illustrated in Figure 2.7. The content in this chapter is quite self-contained, this means that the notation and explanation can be read separately from other chapters. The numerical scheme and the investigation of the implemented model will be provided and discussed for shear and tensile tests in terms of meaning in material science. The results in this chapter have already been published in Sandfeld et al. (2015).

5.1 A continuum model for single-crystal plasticity

Let the reference configuration $\mathcal{B}$ be a bounded Lipschitz domain in $\mathbb{R}^3$ and let $\partial_D \mathcal{B} \cup \partial_N \mathcal{B} = \partial \mathcal{B}$ be non-overlapping decompositions into Dirichlet boundary $\partial_D \mathcal{B}$ and Neumann boundary $\partial_N \mathcal{B}$. The position of a material point is denoted by $\mathbf{x}$ and the displacement of the body from its reference configuration by $\mathbf{u}(\mathbf{x}, t)$.

The deformation tensor $D\mathbf{u}$ is decomposed additively into elastic and plastic parts $\boldsymbol{\beta}^{\text{el}}$ and $\boldsymbol{\beta}^{\text{pl}}$ respectively,

$$D\mathbf{u} = \boldsymbol{\beta}^{\text{el}} + \boldsymbol{\beta}^{\text{pl}}. \tag{5.1}$$

Small deformations are assumed so that the infinitesimal strain $\boldsymbol{\varepsilon}$ is given by

$$\boldsymbol{\varepsilon} = \boldsymbol{\varepsilon}(\mathbf{u}) = \text{sym}(D\mathbf{u}). \tag{5.2}$$

Plastic slip is assumed to take place on N slip systems, each having a unit normal $\mathbf{m}_s$ and slip direction $\mathbf{d}_s = \frac{1}{b_s} \mathbf{b}_s$ on the s-th system, where $\mathbf{b}_s$ is the Burgers vector of length $b_s = |\mathbf{b}_s|$. As an example, the face-centered cubic (FCC) crystal has $N = 12$ slip systems. In special situations symmetry can be exploited and the case $N = 1$ or $N = 2$ can be considered over the crystal of thin film via shearing and bending situations.

The plastic shear strain in the slip system s is denoted by γ_s. In the single crystal, we assume that the plastic part of the displacement gradient is given by the sum over the contributions from all active slip systems

$$\boldsymbol{\beta}^{\mathrm{pl}} \;=\; \sum_s \gamma_s \mathbf{M}_s \tag{5.3}$$

where $\mathbf{M}_s \;=\; \frac{1}{b_s}\mathbf{b}_s \otimes \mathbf{m}_s \;=\; \mathbf{d}_s \otimes \mathbf{m}_s$ is the projection tensor accounting for the orientation of the slip system s.

Depending on the vector of plastic shear strains $\boldsymbol{\gamma} = (\gamma_1, ..., \gamma_N)^\top$, the plastic strain is given by

$$\boldsymbol{\varepsilon}^{\mathrm{pl}} = \boldsymbol{\varepsilon}^{\mathrm{pl}}(\boldsymbol{\gamma}) = \mathrm{sym}(\boldsymbol{\beta}^{\mathrm{pl}}) = \sum_s \gamma_s \mathbf{M}_s^{\mathrm{sym}} , \qquad \mathbf{M}_s^{\mathrm{sym}} = \mathrm{sym}\,\mathbf{M}_s . \tag{5.4}$$

This defines the elastic strain

$$\boldsymbol{\varepsilon}^{\mathrm{el}} \;=\; \boldsymbol{\varepsilon}^{\mathrm{el}}(\mathbf{u}, \boldsymbol{\gamma}) \;=\; \boldsymbol{\varepsilon}(\mathbf{u}) - \boldsymbol{\varepsilon}^{\mathrm{pl}}(\boldsymbol{\gamma}) . \tag{5.5}$$

5.1.1 Variational balance equations

The classical macroscopic equilibrium equation is given by

$$-\nabla \cdot \boldsymbol{\sigma} \;=\; \mathbf{f}_{\mathcal{B}} \quad \text{in } \mathcal{B}, \tag{5.6}$$

where $\boldsymbol{\sigma}$ is the Cauchy stress tensor with the constitutive relation

$$\boldsymbol{\sigma} = \mathbb{C} : \boldsymbol{\varepsilon}^{\mathrm{el}} = \mathbb{C} : (\boldsymbol{\varepsilon} - \boldsymbol{\varepsilon}^{\mathrm{pl}}) \tag{5.7}$$

and $\mathbb{C}$ is the elasticity tensor. The macroscopic boundary conditions are

$$\mathbf{u} = \mathbf{u}_{\mathrm{D}} \quad \text{on} \quad \partial_{\mathrm{D}}\mathcal{B}, \qquad \boldsymbol{\sigma}\mathbf{n} = \mathbf{t}_{\mathrm{N}} \quad \text{on} \quad \partial_{\mathrm{N}}\mathcal{B} . \tag{5.8}$$

Let $U = \big\{\mathbf{u} \in \mathrm{H}^1(\mathcal{B}, \mathbb{R}^3) \colon \mathbf{u} = \mathbf{0} \text{ on } \partial_{\mathrm{D}}\mathcal{B}\big\}$, and assume that $\mathbf{u}_{\mathrm{D}}$ extends to $\mathcal{B}$. Then, we have in weak form: find $\mathbf{u} \in \mathbf{u}_{\mathrm{D}} + U$ such that

$$\int_{\mathcal{B}} (\boldsymbol{\varepsilon}(\mathbf{u}) - \boldsymbol{\varepsilon}^{\mathrm{pl}}) : \mathbb{C} : \boldsymbol{\varepsilon}(\delta\mathbf{u}) \, \mathrm{d}\mathbf{x} = \int_{\mathcal{B}} \mathbf{f}_{\mathcal{B}} \cdot \delta\mathbf{u} \, \mathrm{d}\mathbf{x} + \int_{\partial_{\mathrm{N}}\mathcal{B}} \mathbf{t}_{\mathrm{N}} \cdot \delta\mathbf{u} \, \mathrm{d}\mathbf{a} , \; \delta\mathbf{u} \in U . \tag{5.9}$$

5.2 A numerical scheme for the reduced 2D system

For the numerical evaluation of the physical behavior of our model we consider a 2D reduction of the fully coupled system, where we assume to have a homogeneous distribution over the y direction and slip plane normals $\mathbf{m}_s$ in the $x - y$ plane. This

leads to $\partial_\eta \rho_{s,g} \equiv \partial_\eta q_{s,g} \equiv \partial_\eta v_{s,g} \equiv 0$ everywhere in the system. In this section we describe the discretization for a single slip plane in 1D, $\Gamma = \Gamma_{s,g} = \{\mathbf{z}_g + \xi \mathbf{d}_s : \xi \in \mathbb{R}\}$ where $\mathbf{z}_g$ is a given point defined where the slip plane located in the body; for simplicity we skip the indices s and g.

5.2.1 Reduced hdCDD over 1D slip plane

Rewriting (2.89) using $\partial_\eta \rho \equiv \partial_\eta q \equiv \partial_\eta v \equiv 0$ yields

$$\partial_t \rho = -\widetilde{\nabla} \cdot (\rho \widetilde{\mathbf{V}}) + qv, \tag{5.10a}$$

$$\partial_t q = -\widetilde{\nabla} \cdot (q \widetilde{\mathbf{V}}) - \rho \cos\varphi \partial_\xi \Big(\cos\varphi \partial_\xi v + k \partial_\varphi v \Big) \tag{5.10b}$$

$$- q \partial_\varphi \Big(\cos\varphi \partial_\xi v + k \partial_\varphi v \Big),$$

with $\widetilde{\nabla} = (\partial_\xi, \partial_\varphi)^\top$ and $\widetilde{\mathbf{V}} = (v \sin\varphi, \cos\varphi \partial_\xi v + k \partial_\varphi v)^\top$. Assuming that the velocity does not exhibit any angular anisotropy the system (5.10) reduces further to

$$\partial_t \rho = -\widetilde{\nabla} \cdot (\rho \widetilde{\mathbf{V}}) + qv, \tag{5.11a}$$

$$\partial_t q = -\widetilde{\nabla} \cdot (q \widetilde{\mathbf{V}}) - \rho (\cos\varphi)^2 \partial_\xi^2 v + q \sin\varphi \partial_\xi v. \tag{5.11b}$$

For the construction of a discontinuous Galerkin discretization we rewrite (5.11) in the equivalent form of a linear conservation law for $\mathbf{w} = (\rho, q)^\top$, i.e.,

$$\partial_t \mathbf{w} + \widetilde{\nabla} \cdot \mathbf{F}(\mathbf{w}) + \mathbf{B}\mathbf{w} = \mathbf{0} \quad \text{in } \Gamma \times S^1, \tag{5.12}$$

where $\widetilde{\nabla} \cdot \mathbf{F}(\mathbf{w}) = \partial_\xi (\mathbf{F}_1 \mathbf{w}) + \partial_\varphi (\mathbf{F}_2 \mathbf{w})$ with

$$\mathbf{F}_1 = \begin{bmatrix} v \sin\varphi & 0 \\ 0 & v \sin\varphi \end{bmatrix}, \quad \mathbf{F}_2 = \begin{bmatrix} -\cos\varphi \partial_\xi v & 0 \\ 0 & -\cos\varphi \partial_\xi v \end{bmatrix},$$

$$\mathbf{B} = \begin{bmatrix} 0 & -v \\ (\cos\varphi)^2 \partial_\xi^2 v & -\sin\varphi \partial_\xi v \end{bmatrix}$$

depending on the dislocation velocity v.

5.2.2 The RKDG method

The system (5.12) reads as follows: find $\mathbf{w} : \Gamma \times S^1 \times [0, T] \rightarrow \mathbb{R}^2$ solving

$$\partial_t \mathbf{w} + \mathbf{A}\mathbf{w} = \mathbf{0} \quad \text{in } \Gamma \times S^1 \tag{5.13}$$

subject to the initial condition $\mathbf{w}(\mathbf{r}, \varphi, 0) = \mathbf{w}_0(\mathbf{r}, \varphi)$, periodic boundary conditions $\mathbf{w}(\xi, \eta, 0, t) = \mathbf{w}(\xi, \eta, 2\pi, t)$ in φ, and where

$$\mathbf{A}\mathbf{w} = \widetilde{\nabla} \cdot \mathbf{F}(\mathbf{w}) + \mathbf{B}\mathbf{w} = \mathbf{F}_1 \partial_\xi \mathbf{w} + \mathbf{F}_2 \partial_\varphi \mathbf{w} + (\partial_\xi \mathbf{F}_1 + \partial_\varphi \mathbf{F}_2 + \mathbf{B})\mathbf{w}.$$

In the first step we derive a semi-discrete discontinuous Galerkin scheme. Let $\mathcal{T}_h = \{K\}$ be a triangulation of $\mathcal{B}$, and assume that this triangulation is aligned with the slip plane Γ, i.e., $\Gamma = \bigcup_{f \in \mathcal{F}_\Gamma} f$ with faces $f \in \mathcal{F}_\Gamma = \{\partial K \cap \Gamma \colon K \in \mathcal{T}_h\}$. Let $\mathcal{Z}_h$ be the set of all vertices of the triangulation. For a fixed face $\bar{f} = \mathrm{conv}\{\mathbf{z}_{j-1}, \mathbf{z}_j\}$ with $\mathbf{z}_{j-1}, \mathbf{z}_j \in \Gamma$ we observe

$$
\begin{aligned}
\mathbf{A}(\mathbf{w}, \boldsymbol{\phi})_{f \times S^1} &= \int_{f \times S^1} \left(\widetilde{\nabla} \cdot \mathbf{F}(\mathbf{w}) + \mathbf{B}\mathbf{w} \right) \cdot \boldsymbol{\phi} \, \mathrm{d}\xi \mathrm{d}\varphi \\
&= \int_{f \times S^1} \left(-\mathbf{F}(\mathbf{w}) \cdot \widetilde{\nabla} \boldsymbol{\phi} + \mathbf{B}\mathbf{w} \cdot \boldsymbol{\phi} \right) \mathrm{d}\xi \mathrm{d}\varphi + \int_{S^1} \widetilde{\mathbf{n}} \cdot \mathbf{F}(\mathbf{w}) \cdot \boldsymbol{\phi} \Big|_{\mathbf{z}_{j-1}}^{\mathbf{z}_j} \mathrm{d}\varphi
\end{aligned}
$$

for all smooth functions $\boldsymbol{\phi} \colon f \times S^1 \longrightarrow \mathbb{R}^2$. For the discretization we choose an ansatz space X_f on every face defining a discontinuous ansatz space $X_h = \{\boldsymbol{\phi}_h \in \mathrm{L}_2(\Gamma, \mathbb{R}^2) \colon \boldsymbol{\phi}_h|_f \in X_f\}$ and the numerical flux

$$\mathbf{F}^*_{f,e}(\boldsymbol{\phi}_h) = \{\{\mathbf{F}_f \boldsymbol{\phi}_h\}\}_{f,e} + \frac{C_f}{2} [[\boldsymbol{\phi}_h]]_{f,e} \widetilde{\mathbf{n}}$$

on the face intersections $e = \partial f \cap \partial f_e$ (which are single points in a 1D slip plane). Here, we choose the stabilization constant $C_f = |\widetilde{\mathbf{V}}|$, and the average and the jump along a normal $\widetilde{\mathbf{n}}$ oriented from f to f_e are given by

$$\{\{\mathbf{F}\mathbf{w}_h\}\}_{f,e} := \frac{1}{2}\left(\mathbf{F}\mathbf{w}_h|_f + \mathbf{F}\mathbf{w}_h|_{f_e}\right), \qquad [[\mathbf{w}_h]]_{f,e} := \mathbf{w}_f|_f - \mathbf{w}_f|_{f_e},$$

respectively. On the open boundary, we set $\mathbf{w}_h|_{f_e} = \mathbf{w}_h|_f$ and $\mathbf{w}_h|_{f_e} = -\mathbf{w}_h|_f$ for the impenetrable boundary. Now, defining locally

$$
\begin{aligned}
(\mathbf{A}_{f,h}\mathbf{w}_h, \boldsymbol{\phi}_h)_{f \times S^1} &= \int_{f \times S^1} \left(-\mathbf{F}(\mathbf{w}_h) \cdot \widetilde{\nabla} \boldsymbol{\phi}_h + \mathbf{B}\mathbf{w}_h \cdot \boldsymbol{\phi}_h \right) \mathrm{d}\xi \mathrm{d}\varphi \\
&\quad + \int_{S^1} \widetilde{\mathbf{n}} \cdot \mathbf{F}^*_{f,e}(\mathbf{w}_h) \cdot \boldsymbol{\phi}_h \Big|_{\mathbf{z}_{j-1}}^{\mathbf{z}_j} \mathrm{d}\varphi
\end{aligned}
$$

yields the discrete operator by $(\mathbf{A}_h \mathbf{w}_h, \boldsymbol{\phi}_h)_{\Gamma \times S^1} = \sum_f (\mathbf{A}_{f,h}\mathbf{w}_h, \boldsymbol{\phi}_h)_{f \times S^1}$. We choose a DG ansatz space with Fourier basis functions $X_f = \mathbb{P}_k \otimes \mathbb{F}_n$, where $\mathbb{P}_k = \mathrm{span}\{1, \xi, ..., \xi^k\}$ are polynomials, and the truncated Fourier space is given by

$$\mathbb{F}_n = \mathrm{span}\{1, \cos(\varphi), \sin(\varphi), ..., \cos(n\varphi), \sin(n\varphi)\}.$$

Thus, the components of $\mathbf{w}_h = (\rho_h, k_h)$ have the form

$$\rho_h(\xi, \varphi) = \sum_{l=0}^{k} \xi^l \left(a_{l0} + \sum_{m=1}^{n} \left(a_{lm} \cos(m\varphi) + b_{lm} \sin(m\varphi) \right) \right)$$

and similar for q_h. The Runge–Kutta time discretization is now obtained by the method of lines. Therefore, choosing a basis $\boldsymbol{\phi}^1, ... \boldsymbol{\phi}^N$ of X_h yields the matrix formulation

$$\underline{M} \partial_t \underline{u}(t) + \underline{A} \, \underline{u}(t) \;=\; 0 \tag{5.14}$$

with $\underline{M} = \left((\boldsymbol{\phi}^k, \boldsymbol{\phi}^m) \right)_{m,k}$ and $\underline{A} = \left(\mathbf{A}_h(\boldsymbol{\phi}^k, \boldsymbol{\phi}^m) \right)_{m,k}$. This yields for the time step from t_n to t_{n+1}

$$\underline{u}^{n+1} = \underline{u}^n - \triangle t \underline{M}^{-1} \underline{A} \Big(u^k - \frac{1}{2} \triangle t \underline{M}^{-1} \underline{A} \big(u^n - \frac{1}{3} \triangle t \underline{M}^{-1} \underline{A} \big(u^n - \frac{1}{4} \triangle t \underline{M}^{-1} \underline{A} \, u^n \big) \big) \Big)$$

for the classical explicit Runge–Kutta schemes of order 4 (see Hochbruck et al. (2015) for alternative time integration methods in combination with DG schemes).

5.2.3 Finite element discretization of the solid

Let $V_h = \left\{ \mathbf{v} \in \mathrm{H}^1(\mathcal{B})^2 \colon \mathbf{v}|_K \in \mathbb{P}_1(K) \text{ for } K \in \mathcal{T}_h \right\}$ be a standard finite element space for the displacements and set $V_h(\mathbf{u}_\mathrm{D}) = \left\{ \mathbf{v} \in V_h \colon \mathbf{v}(\mathbf{z}) = \mathbf{u}_\mathrm{D}(\mathbf{z}) \text{ for all nodal points } \mathbf{z} \in \mathcal{Z}_h \cap \partial_\mathrm{D}\mathcal{B} \right\}$. For $\mathbf{u} \in V_h$ the strain $\boldsymbol{\varepsilon}(\mathbf{u})$ and the stress $\boldsymbol{\sigma} = \mathbb{C} : \boldsymbol{\varepsilon}$ is piecewise constant in K. Now, the coupled algorithm is defined as follows:

S0) Select $\triangle t > 0$, $N \in \mathbb{N}$, set $n = 0$, set initial values for $\rho_{s,g}^0, q_{s,g}^0, \gamma_{s,g}^0$ on $\Gamma_{s,g}$.

S1) Set $t_n = n\triangle t$, $\mathbf{u}_{\mathrm{D}}^n = \mathbf{u}_{\mathrm{D}}(t_n)$, $\mathbf{f}_{\mathcal{B}}^n = \mathbf{f}_{\mathcal{B}}(t_n)$ and $\mathbf{g}_{\mathrm{N}}^n = \mathbf{g}_{\mathrm{N}}(t_n)$.

Compute γ_s^n in $\mathcal{B}$ from $\gamma_{s,g}^n$ in $\Gamma_{s,g}$ (depending on Case 1 or 2 in Sec. 2.3).

S2) Evaluate the plastic strain $\boldsymbol{\varepsilon}^{\mathrm{pl},n}|_K = \sum_s \gamma_s^n|_K \mathbf{M}_s^{\mathrm{sym}}$ and compute $\mathbf{u}^n \in V_h(\mathbf{u}_{\mathrm{D}}^n)$ with

$$\int_{\mathcal{B}} \boldsymbol{\varepsilon}(\mathbf{u}^n) : \mathbb{C} : \boldsymbol{\varepsilon}(\delta\mathbf{u})\,\mathrm{d}\mathbf{x} = \int_{\mathcal{B}} \boldsymbol{\varepsilon}^{\mathrm{pl},n} : \mathbb{C} : \boldsymbol{\varepsilon}(\delta\mathbf{u})\,\mathrm{d}\mathbf{x} + \int_{\mathcal{B}} \mathbf{f}_{\mathcal{B}} \cdot \delta\mathbf{u}\,\mathrm{d}\mathbf{x}$$
$$+ \int_{\partial_{\mathrm{N}}\mathcal{B}} \mathbf{g}_{\mathrm{N}} \cdot \delta\mathbf{u}\,\mathrm{d}\mathbf{a}\,, \quad \delta\mathbf{u} \in V_h(0)\,.$$

S3) On $f = K \cap K' \subset \Gamma_{s,g}$ set $\tau_{s,g}^n|_f = \frac{1}{2}\Big(\boldsymbol{\sigma}^n|_K + \boldsymbol{\sigma}^n|_{K'}\Big) : \mathbf{M}_s$ and compute velocities $v_{s,g}^n$ (eqn. (2.91)).

S4) Compute $(\rho_{s,g}^{n+1}, q_{s,g}^{n+1})$ independently on every $\Gamma_{s,g}$ by M explicit Runge–Kutta steps for (5.14) with step size $\triangle t/M$ and fixed velocity $v_{s,g}^n$.

S5) If $n < N$, set $n = n + 1$ and go to S1).

Since this scheme in step S4) is full explicit, the CFL condition requires sufficiently small time steps. Also the coupling with the boundary value problem S2) is explicit. In our numerical tests we choose the global time step $\triangle t$ and the local time step $\triangle t/M$ small enough to observe convergence by comparing the results with different mesh resolution h.

5.3 Numerical experiments

We evaluate our model for a single-crystal thin film with idealized passivated and non-passivated surfaces in a tensile test setting. This is a well established benchmark test for crystal plasticity models, see (e.g. Liu et al., 2011; Schwarz et al., 2005; Zaiser et al., 2007; Deshpande et al., 2005; Fredriksson and Gudmundson, 2005; Fertig and Baker, 2009)). The novelty of hdCDD, however, is that we can directly link the dislocation microstructure in almost DDD-like details to the macroscopic response. In the following, we study in particular the influence of the line curvature and two different physical boundary conditions in single- and multislip configurations. Additionally, we evaluate numerically effects due to averagings for Case 1 and 2. We note, that especially the line curvature is a physical parameter that does not occur in any other continuum models, which makes detailed comparisons difficult.
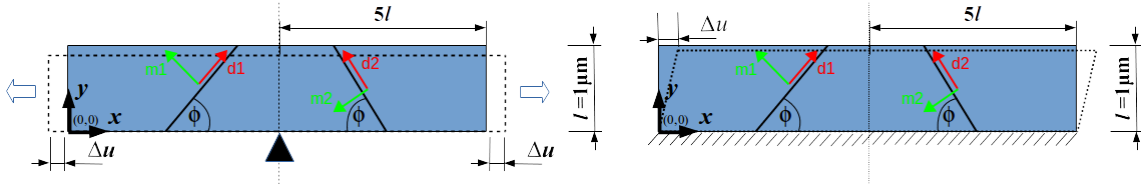
(a) Tensile test: Displacements are prescribed at left and right boundaries, top and bottom boundaries are free surfaces.

(b) Shear test: Displacements are prescribed at bottom and top boundaries, left and right boundaries are free surfaces.

Figure 5.1: Geometry and boundary conditions of the investigated model systems for the tensile test (Study 1 and Study 2) and the shear test (Study 3).

Geometry and slip system

We consider the configuration defined in Liu et al. (2011) for the investigation of the deformation behavior of a thin, single-crystalline Al film during tensile loading assuming plane strain. The film is represented by a 2-dimensional body $\mathcal{B} = (0, 10l) \times (0, l)$ with $l = 1$ µm. We consider one or two active slip systems ($N = 1$ or 2) with 1-dimensional (crystallographic) slip planes determined by

$$\mathbf{d}^1 = \cos\phi\ \mathbf{e}_1 + \sin\phi\ \mathbf{e}_2\,, \qquad \mathbf{m}^1 = -\sin\phi\ \mathbf{e}_1 + \cos\phi\ \mathbf{e}_2\,, \qquad (5.15a)$$

$$\mathbf{d}^2 = -\cos\phi\ \mathbf{e}_1 + \sin\phi\ \mathbf{e}_2\,, \qquad \mathbf{m}^2 = -\sin\phi\ \mathbf{e}_1 - \cos\phi\ \mathbf{e}_2 \qquad (5.15b)$$

with the angle $\phi = \pi/3$ between slip planes and the film surfaces. The distance between crystallographic slip planes is set to $\triangle s = 0.05, 0.1, 0.2$ µm, respectively. For the thickness of the crystallographic layer $\mathcal{B}_{s,g}$ we choose $h = 0.5\triangle s$. In Case 2, we set $\triangle \bar{s} = 0.2, 0.4$ µm. As material we use aluminum with a Young's modulus of $E = 7 \cdot 10^{10}$ Pa, Poisson ratio $\nu = 0.3$, Burgers vector size $b = 2.56 \cdot 10^{-10}$ m and drag coefficient $B = 2.0 \cdot 10^{-4}$ Pa·s.

5.3.1 Numerical aspects

We use two different finite element meshes: the mesh for the elastic problem consists of triangular linear finite elements with altogether $\approx 223\,000$ degrees of freedom (dofs), the hdCDD mesh consists of linear Fourier elements with, e.g. $\approx 262\,000$ dofs for Case 1 with $\triangle s = 100$ nm and $h = 50$ nm. For the time integration we used a step size of $\triangle t = 10^{-3}$µs with $M = 10$ 'micro-time steps' per macroscopic displacement increment, resulting in $6 \cdot 10^3$ micro-time steps for reaching the total strain of $\varepsilon^{\text{tot}} = 1.2\%$. For the shear test the same step size is used with a total number of $5 \cdot 10^3$ micro-time steps for obtaining the total strain of $\varepsilon^{\text{tot}} = 2.5\%$.

Boundary conditions

For the two different systems we introduce different boundary conditions for the elasticity problem:

(1) For the symmetric tensile test we consider prescribed boundary displacements along the left and right boundary face (at $x_1 = 0$ and $x_1 = 10l$, respectively). We increase the displacements with a constant rate $\dot{u}_{1,right} = -\dot{u}_{1,\text{left}} = 1.0$ m/s for $t \in [0, 0.06]$ µs. In order to avoid vertical translations we additionally fix the displacements at the point $(5l, 0)^\top$.

(2) For the shear test we consider prescribed boundary displacements along the upper surface at $x_2 = l$ and fixed displacements at the lower surface at $x_2 = 0$. The upper prescribed displacements are increased with a constant rate $\dot{u}_{1,\text{up}} = 1.0$ m/s for $t \in [0, 0.05]$ µs.

For both systems, also the boundary conditions for the dislocation problem w.r.t. dislocation fluxes have to be considered. In physical terms surfaces can either be open (dislocations can leave the film) or impenetrable (dislocations cannot leave the film). Open boundaries can simply be modeled by extrapolating the hdCDD field values. For impenetrable surfaces we require (i) that the flux of dislocation density normal to the surface vanishes and that (ii) dislocations directly at the surface must be straight and thus must have zero curvature. Numerically, we model the impenetrable flux boundary condition by introducing a numerical inflow defined as the negative outflow of density and curvature densities on the considered boundary.

Initial values

We construct consistent initial values which guarantee that, e.g., the solenoidality of $\boldsymbol{\alpha}^{\mathbb{II}}$ (i.e. $\operatorname{div} \boldsymbol{\alpha}^{\mathbb{II}} = 0$) is not violated and that the GND density comes out as a gradient of the plastic slip. This is done by superposition of N_d randomly distributed discrete dislocation loops in a 2D slip plane followed by an appropriate 'smearing-out' procedure as described in detail in Section 5.5.1. One-dimensional slip plane data are then obtained by integrating the CDD field values over the second, homogeneous direction (see Fig. 5.2). Depending on the used averaging, i.e. Case 1 or 2, we finally have to consider the distance of the representative slip planes.
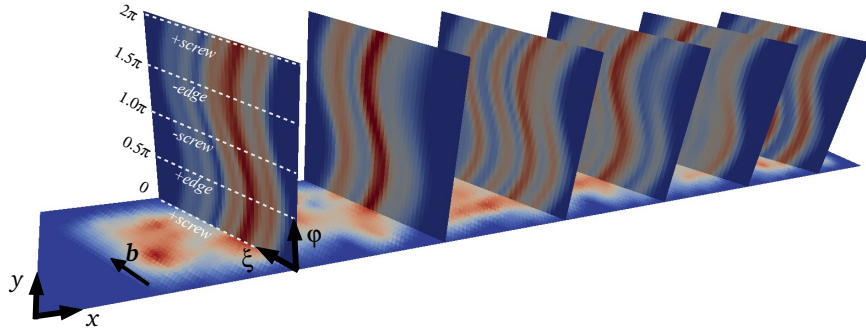
Figure 5.2: Visualization of the initial dislocation density in the higher-dimensional configuration space for a system with 25 representative slip planes, each of then containing 28 'smeared-out' randomly positioned loops. In vertical direction the variable $\varphi \in [0, 2\pi]$ is displayed for some of the 25 slip planes; the dashed white lines indicate the line orientation for screw and edge segments (compare Burgers vector direction in the spatial plane). Each of the wavy distributions corresponds to (a) dislocation loop(s). On the bottom plane the spatial projection of the total density ρ^{tot} is shown as spatial average as seen in 'Case 2'.

5.3.2 Study 1: The influence of boundary conditions (Case 1)

For this investigation we use 80 representative slip planes and the shear strain extension of Case 1, starting in each SP with 5 dislocation loops of radius r between $100\,\mathrm{nm}$ and $200\,\mathrm{nm}$ at random positions. The height of the quasi-discrete numerical SPs has a relatively small value of $h = 50\,\mathrm{nm}$ below which no appreciable difference in the system response could be observed (also see Study 2). For averaging purposes we assume an out-of-plane length of $L_z = l/\sin(\phi) = 1.15\,\mathrm{\mu m}$ resulting in an average dislocation density $\langle \rho \rangle = 3.1 \times 10^{13}/\mathrm{m}^2$. For the analysis of the influence of boundary conditions we study two configurations: in the first configuration we choose open boundaries (abbreviated as 'open BCs'), i.e. dislocations can leave the volume, and the second imposes impenetrable boundaries (abbreviated as 'imp. BCs'), i.e. dislocations can not leave the volume through the surface ∂B. The simulation is driven by a prescribed constant strain rate $\dot{\varepsilon} = 0.2\,\mathrm{\mu s}^{-1}$ until the maximum total strain $\varepsilon^{\mathrm{tot}} = 1.2\%$ is reached.

In Fig. 5.3 the evolution of the total density ρ^{tot} at three distinct time steps in the $x - y$-plane is illustrated. We observe that the configuration with open boundaries approaches a constant total density distribution while the system with impenetrable boundaries forms pile-ups of dislocations at the boundary with constant density values in between. To analyze this behavior we investigate the dislocation microstructure in the higher-dimensional configuration space at final time for a slip plane in the center of the film in more detail (Fig. 5.4). The higher-dimensional fields show
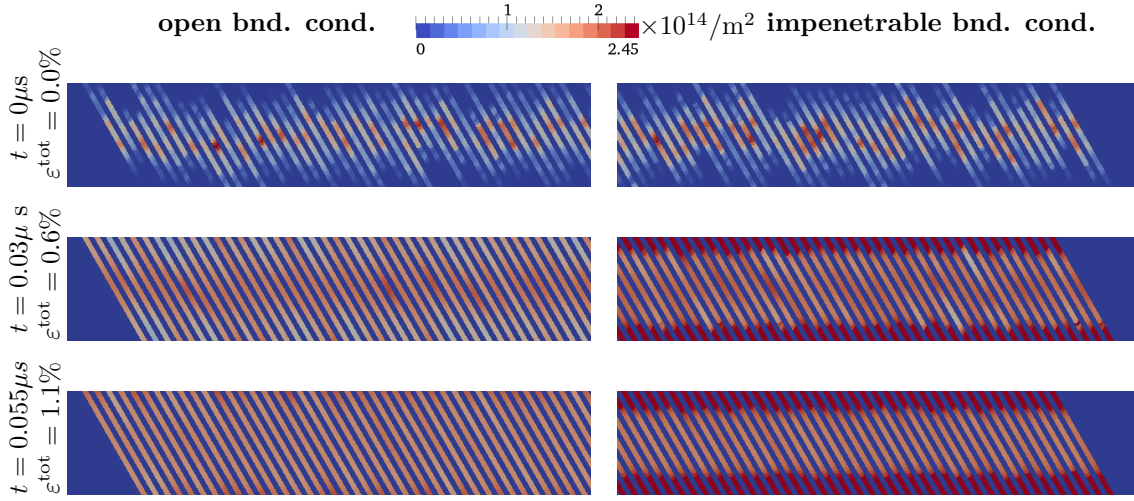
Figure 5.3: Initial distribution and time evolution of total density ρ^{tot}, Case 1, at $t = 0.03$ µs and $t = 0.055$ µs with open and impenetrable boundary conditions for the dislocation density.

that for both dislocation boundary conditions after an initial 'incubation' time the center region of the slip plane approaches a state which is characterized by only edge dislocations of positive and negative orientation: $\rho(x,\varphi)$ is approximately non-zero only for the orientations $\varphi = \pi/2$ and $\varphi = 3\pi/2$. The reason for this is that dislocation loops expanded and segments with edge orientation either left the film through the surface or pile up against the surface. In any case, only screw segments are left behind which in this 2D model thread the film into the out-of-plane direction. Investigating the curvature $k = \rho/q$ we also see that the screw segments are nearly straight (i.e. $k \approx 0$); only for the impenetrable boundaries we find a non-zero curvature shortly before the surface: here, dislocations need to bend strongly in order to adjust from the threading screw dislocation orientation to the geometry of the films' surface. This also suggests that the amount of dislocations inside the film for the impenetrable system will be significantly higher: to begin with, dislocations are not 'lost' by out-flux through the surfaces, and additionally increased line length production will take place due to the high dislocation curvature near the surfaces. Plotting the average density evolution in Fig. 5.5 (b) shows that in the elastic regime I the dislocation density is constant, i.e. the resolved shear stress is not large enough to overcome the yield stress. This is followed in regime II by a transition of free loop expansion which results in a high dislocation multiplication rate. Towards regime III, edge components are then lost through open surfaces, while for impenetrable BCs edge dislocations are deposited at the surfaces. The open system contains at final strain a density which is smaller roughly by a factor of 3, and additionally the average density even reaches a stationary state (threading screw segments are straight and thus only translate). For the system with impenetrable surfaces the average
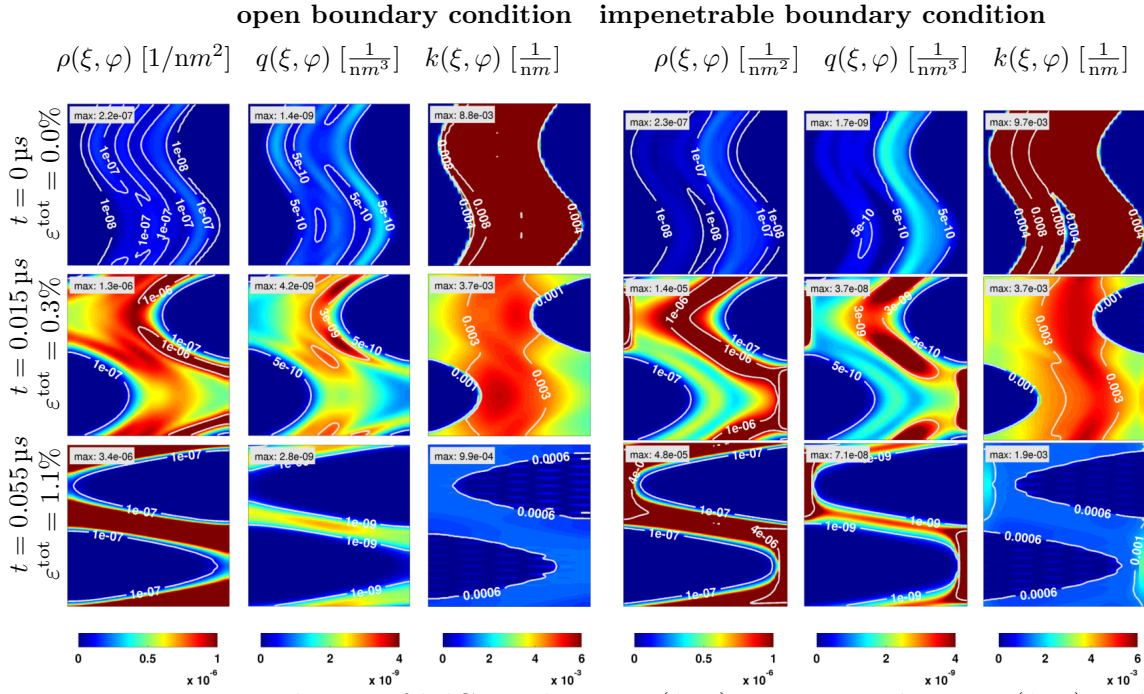
Figure 5.4: Time evolution of hdCDD density $\rho(\xi, \varphi)$, curvature density $q(\xi, \varphi)$ and curvature $k(\xi, \varphi) = q(\xi, \varphi)/\rho(\xi, \varphi)$ for open (left block) and impenetrable boundaries (right block) for a slip plane with random initial values taken from the center region of Fig. 5.3. On the vertical axis is the line orientation $\varphi \in [0, 2\pi]$, on the horizontal axis is the local ξ coordinate, the small text label indicates the maximum field value.

density increases approximately linearly (caused by the constant line length increase of deposited edges).

What are the consequences for the macroscopic stress-strain response? A higher dislocation density, on the one hand, obviously comes with a stronger influence of the Taylor equation for the yield stress. On the other hand, a higher plastic activity, where the density comes in through the Orowan relation, causes plastic softening through the solution of the elastic eigenstrain BVP. The competition of these two effects can be observed in the macroscopic stress-strain curve in Fig. 5.5 (a) where at larger strains the obtained stress level for the system with open boundaries is only slightly lower. Interesting to note is also the initial 'hump' right after the elastic regime I when softening sets in. This is caused by the fact that at an early stage dislocation loops are still comparatively small and thus contribute with a high line tension effect which effectively reduces the resolved shear stress. Once loops have expanded, this contribution is reduced and the softening behavior is sustained. A very similar behavior is also observed in DDD simulations Weygand and Gumbsch (2005).

Finally, we compare the evolution of the initial dislocation loop distribution to a distribution of positive and negative edge dislocations (dashed lines in Fig. 5.5). For the latter we choose the number of edge dislocations such that the initial density

(a) average stress vs. total strain

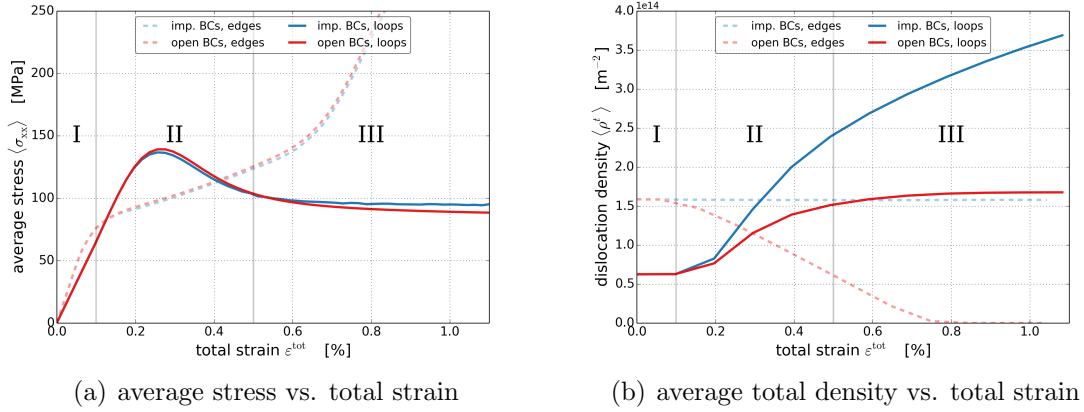(b) average total density vs. total strain

Figure 5.5: Macroscopic quantities (Case 1) for two different boundary conditions (open and impenetrable) and two different initial configurations (consisting of either only loops or only straight edge dislocations). The three different time snapshots in Fig. 5.4 correspond to the different regimes I, II, and III, respectively.

is similar to the saturation density of loops with open BCs. We observe that after the onset of plastic yield edge dislocations flow towards the surfaces (regime II). They either get lost through the surfaces (open BCs) or pile up against the surface (imp. BCs) in which case the density simply stays constant because the number of edge dislocations is preserved. This microstructure results in a dramatically different stress-strain response as compared to the system with curved dislocations: because we have neither an increase in density nor a line tension one can only observe a linear hardening (regime II) which – regardless the boundary condition – is followed by a nearly elastic regime III where the stresses are considerably different from those reached for the system with dislocation loops.

5.3.3 Study 2: Spatial coarsening from Case 1 to Case 2

In Case 1 we considered slip planes as quasi-discrete objects mimicking the situation in DDD simulations. This not only requires a very high spatial resolution for the finite element scheme, but it is also somewhat unsatisfying from a conceptual point of view to have two different resolutions (within the slip plane and perpendicular to it). If this can be avoided by use of Case 2 and whether it is admissible will be studied subsequently: for a given initial distribution of dislocations loops we compare the asymptotic system response for $h \to 0$ in Case 1 and then compare with results obtained for different values of $\triangle \overline{s}$ in Case 2.

All system and geometry properties are the same as in the previous Study 1, but this time we only compute stresses for a given dislocation configuration. To make the configurations easier to compare we simply choose a homogeneous distribution of loops. Fig. 5.6 (a) shows the resulting stresses for the quasi-discrete Case 1 for a

(a) Distribution of the stress component σ_{xx} on the left half part $(0, 5l) \times (0, l)$.

(b) Averaged stress $\langle \sigma_{xx} \rangle = \frac{1}{L_x} \int_0^{L_y} \sigma_{xx} \, \mathrm{d}x$ at $\varepsilon^{\mathrm{tot}} = 0$.
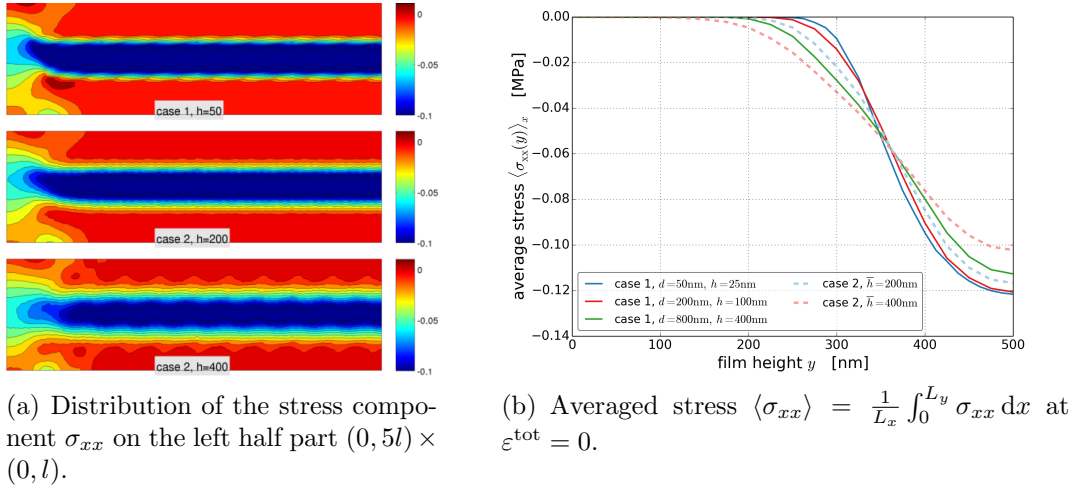
Figure 5.6: Comparison of Case 1 and Case 2 for different numerical SP heights at $t = 0$ for a homogeneous distribution of loops of the same radius. (a) shows the spatial stress distribution, (b) shows averaged stress profiles across the height. Since the configuration is symmetric, only half of the profile is shown.

SP height of $h = 50 \, \mathrm{nm}$ and two different discretizations for Case 2. If we average these stress distributions we obtain stress profiles as shown in Fig. 5.6 (b). It shows that for values of $h = 100 \, \mathrm{nm}$ and below the stresses do not change appreciably anymore. Running the same simulations for Case 2 where the plastic strain is coarse grained in between the numerical SPs and comparing with the results for Case 1 allows for the conclusion that for this system a $\triangle \bar{s} = 200 \, \mathrm{nm}$ is sufficient; also the stress-strain behavior (not shown) does not show any significant difference. The considered situation of a homogeneous loop distribution is of course artificial. In fact, differences during time evolution in particular between the very coarse Case 2 and the fine Case 1 become larger if we start with random initial values and as the plastic slip becomes more heterogeneous (early in regime II). Nonetheless, even there, our chosen approximation of Case 2 with $\triangle \bar{s} = 200 \, \mathrm{nm}$ is sufficient.

The advantage of the interpolation approach used in Case 2 becomes obvious when we take a look at the degrees of freedoms and the computational time used for the simulations shown in Tab. 5.1.

5.3.4 Study 3: A double slip configuration with Case 2

We now investigate the macroscopic elasto-plastic response together with the microstructural evolution in a configuration with the two slip systems (5.15). We use fully averaged dislocation distributions (Case 2 with $\triangle \bar{s} = 200 \, \mathrm{nm}$), and the in-

configuration	dofs (FEM + DG)	time in h.(8 proc.)
Case 1, $\triangle s = 50\,\text{nm}$, $h = 25\,\text{nm}$	$214\,962 + 1\,049\,600$	7:39:33
Case 1, $\triangle s = 100\,\text{nm}$, $h = 50\,\text{nm}$	$54\,682 + 262\,400$	1:49:01
Case 1, $\triangle s = 200\,\text{nm}$, $h = 100\,\text{nm}$	$54\,682 + 131\,200$	1:00:35
Case 2, $\triangle \overline{s} = 200\,\text{nm}$	$54\,682 + 131\,200$	1:00:44
Case 2, $\triangle \overline{s} = 400\,\text{nm}$	$54\,682 + 65\,600$	0:46:04

Table 5.1: Comparison of computational time and degrees of freedom for Case 1 and Case 2.

teraction of the dislocation densities in the two systems is described by the yield function

$$\tau_{s,g}^{\text{y}} = a\mu b_s \sqrt{\rho_1^{\text{tot}} + \rho_2^{\text{tot}}}\,, \tag{5.16}$$

where ρ_s^{tot} is reconstructed in $\mathcal{B}$ from $\rho_{s,g}^{\text{tot}}$ by averaging and interpolation using the construction (2.84). The line tension is obtained in full analogy to Study 1 for each slip system separately. Subsequently, we compare a single slip and double slip scenario with the following initial distribution of the dislocation density: in both cases we have altogether 800 dislocation loops in an averaging volume for which we again assume an out-of-plane averaging length of $L_z = 1.15\,\mu\text{m}$. The loops' radii are taken from a uniform random distribution in the range of $[100, 200]\,\text{nm}$. We either distribute them across the two slip systems or only across a single slip system such that the average dislocation density in the full body is always the same. In this study we only consider open boundaries since we focus here on the investigation of the hardening/softening effects introduced by the interaction of the slip systems and the concomitant change in dislocation microstructure. The results are illustrated in Figs. 5.7–5.9.

Initially ($\varepsilon^{\text{tot}} \leq 0.2\%$) both systems respond nearly perfectly elastic because the resolved shear stress is in almost all regions smaller than the yield stress. This can be seen in the linear increase in Fig. 5.8(a) which is a consequence of the (nearly) zero velocity in Fig. 5.7 (c) and (f).

Eventually ($0.2\% < \varepsilon^{\text{tot}} < 0.5\%$), starting from the outer regions of the density distribution where ρ^{tot} is smaller, the yield stress will be overcome. This results in a non-zero dislocation velocity mainly in the surface-near regions (Fig. 5.7 (c) and (f) and further plots shown in the Section 5.5.1). Already shortly after $\varepsilon^{\text{tot}} = 0.2\%$ it becomes visible that the single slip and double slip systems behave very differently. The reason for this lies in the crystallography of the model systems: the Burgers vectors of the symmetrically inclined slip systems are such that under the prescribed shear deformation the plastic strain tensors will partially cancel out. This results in a

higher resolved shear stress since the plastic softening contribution is smaller. At the same time, however, the resulting velocity is higher, giving rise to more dislocation activity which can be observed in the plastic strain profile (compare Fig. 5.7 (b) and (e)). For the single slip situation these relations are just the other way around: the plastic slip reduces the resolved shear stress and thus the dislocation velocity. The reduced plastic activity also shows in the evolution of the dislocation density and plastic slip which happens at a lower rate than for the double slip system, cf. Fig. 5.8(b).

profiles for the single slip configuration

| (a) total density | (b) plastic slip | (c) velocity |

profiles for the double slip configuration

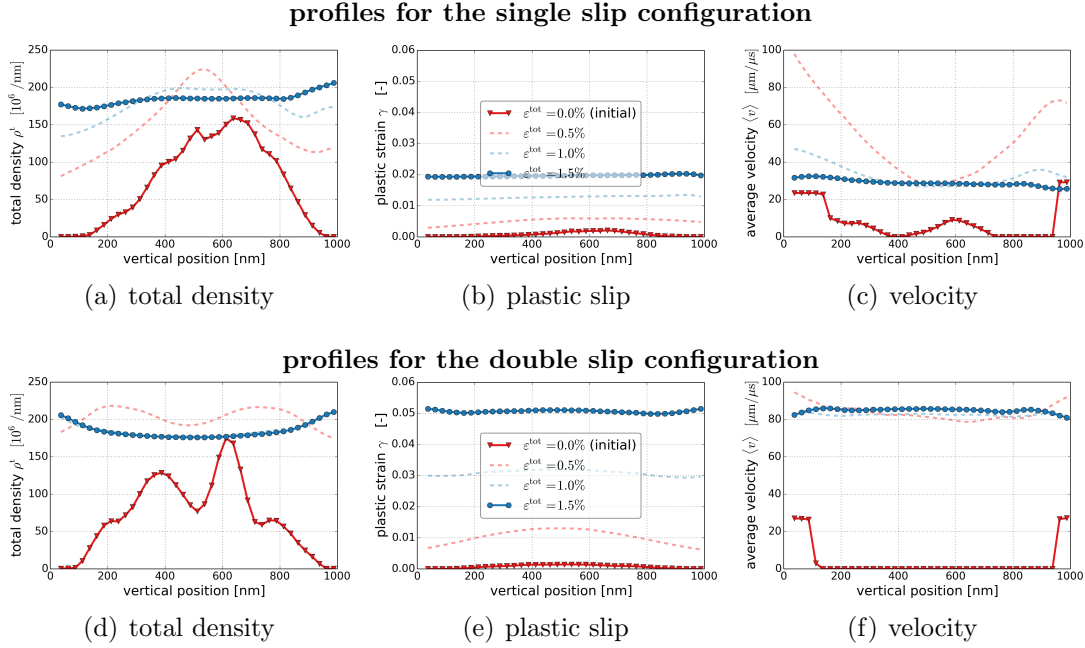| (d) total density | (e) plastic slip | (f) velocity |

Figure 5.7: Profiles of CDD field variables along a central slip plane for the single slip (a–c) and double slip configuration (d–f) for 4 different time steps. Double slip density values and plastic slip (d–f) were multiplied by a factor of 2 to make them comparable with the single slip situation.

We will now take a closer look at some details of the stress-strain curve (Fig. 5.8(a)). What causes the 'humps' and different maxima for single/double slip following the elastic regime at $\varepsilon^{\mathrm{tot}} \approx 0.5\%$? Fig. 5.9 shows the higher-dimensional density, curvature density and curvature fields. There it can be seen, that for the single slip system the lower velocity broadens the density distribution but does not allow for a more significant expansion of loops and thus retards the density production. As a consequence of the reduced loop expansion, the loops curvature is also much higher for the single slip system, giving rise to a more pronounced influence of the line tension (cf. plots in the Section 5.5.1); as a consequence of the retarded density production the yield stress is effectively lower. The latter shows in Fig. 5.8(a) in the lower maximum of the hump as compared to the double slip situation; the former shows in the steeper inclination following the hump. While loops expand the influence of the line tension becomes smaller and tends to zero with edge segments

leaving the film and screw dislocations becoming straight lines. The influence of the yield stress approaches a constant value once the density from the nearly straight edge dislocations saturates. Therefore, towards larger total strains ($> 2\%$) the only difference between the single and double slip system stems from the plastic strain, while microscopic, short-range stresses had a stronger influence on early details of the stress-strain response.
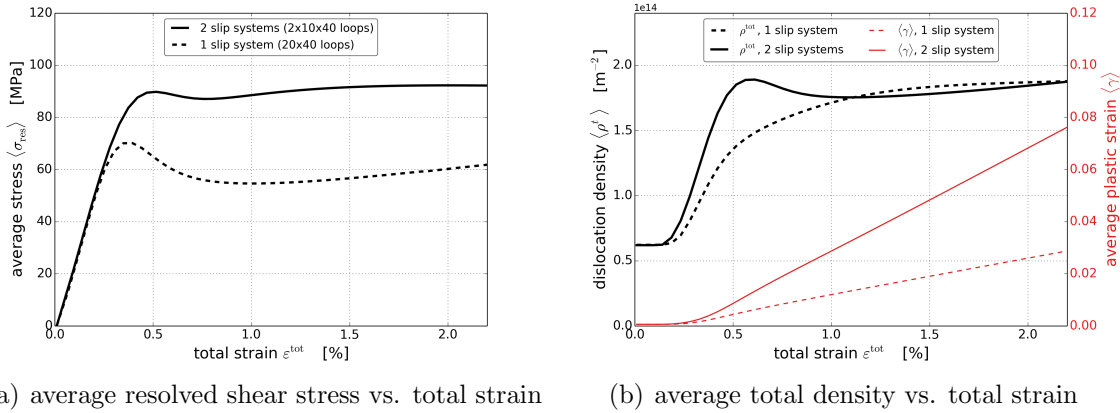

(a) average resolved shear stress vs. total strain

(b) average total density vs. total strain

Figure 5.8: Stress-strain plot and evolution of total density and plastic slip for the single slip and double slip configuration.

5.4 Summary and Conclusion

Modeling and prediction of crystal-plasticity on the micro-meter scale requires a faithful representation of the underlying physical mechanisms. We introduced the higher-dimensional CDD theory as a mathematical description of the kinematic behavior of statistically averaged ensembles of dislocations. A special emphasis was put on a consistent geometric description of the CDD field equations for the general case of arbitrarily oriented slip systems. In particular the transfer of information from two-dimensional crystallographic slip planes to the three-dimensional continuous body was concisely formulated. Furthermore, a conservative discontinuous Galerkin scheme suitable for the dislocation problem was derived. These model formulations were then applied to simulate different plain-strain slip geometries under tensile and shear loading conditions together with different physical boundary conditions. We analyzed in detail how systems of dislocation evolve while they interact with each other due to short-range and long-range stress components. In doing so we could directly link the dislocation microstructure – represented by the higher-dimensional density and curvature density – to the macroscopic behavior (e.g. stress-strain response or average density). By comparing to systems of straight edge dislocations we observed that the line curvature has a strong influence on the hardening behavior: not only did the stress-strain curve change quantitatively, it
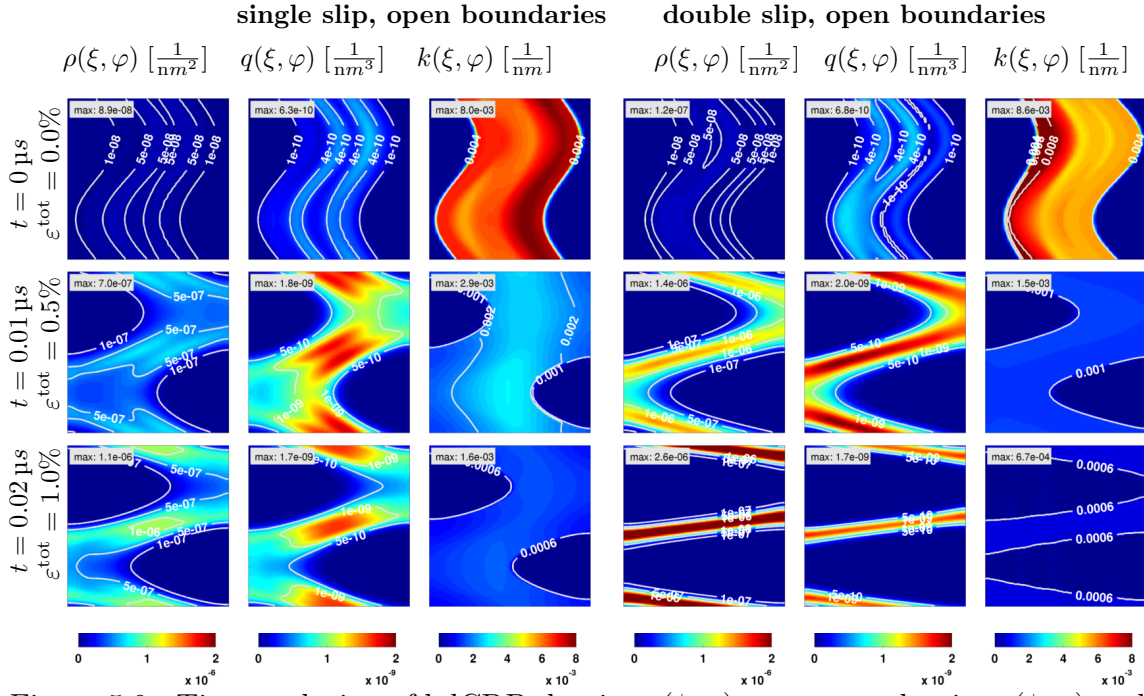
Figure 5.9: Time evolution of hdCDD density $\rho(\xi, \varphi)$, curvature density $q(\xi, \varphi)$ and curvature $k(\xi, \varphi) = q(\xi, \varphi)/\rho(\xi, \varphi)$ for open boundaries, left: in single slip configuration (compare Study 1, Fig. 5.4) and right: in double slip configuration with random initial values taken from the center region of Fig. 5.10. On the vertical axis is the line orientation $\varphi \in [0, 2\pi]$, on the horizontal axis is the local ξ coordinate, the small text label indicate the maximum field value (comparison with Fig. 5.4 of Study 1).

also changed qualitatively which would be explained by hdCDD. Furthermore, we showed how physical boundary conditions influence the orientation distribution of dislocations and again, how this impacts the system response. Finally, we studied a double slip configuration where we could again attribute the distinctly different hardening behavior for single/double slip to microstructural aspects.

The hdCDD model contains microstructural information which otherwise is only available in DDD simulations. These microstructural details have a strong influence on the system response, which is why a comparison with other models is difficult: no other standard continuum plasticity model is able to represent e.g. the conversion of SSDs into GNDs and the dislocation line length production accompanied by expansion of dislocation loops. Thus, direct comparisons with DDD simulation will be extremely interesting and helpful to further benchmark our model. The necessary extraction of information from DDD simulations and converting them into continuous fields, however, is a non trivial task which needs to be undertaken with care in future work. Additionally, DDD could be used to identify physical formulations for incorporating further dislocation interactions and reactions into our continuum model. With this we hope to go beyond what up to date is possible with DDD and

apply CDD to realistic three-dimensional systems with large numbers of interacting dislocations and plastic strain.

5.5 Appendix

5.5.1 Computation of consistent initial values

Special care has to be taken with creating initial values for CDD simulations. 'Consistent initial values' are those which represent averaged systems of dislocations such that the solenoidality of $\boldsymbol{\alpha}^{\mathrm{II}}$ is not violated, i.e. $\operatorname{div} \boldsymbol{\alpha}^{\mathrm{II}} = 0$. An additional constraint is the compatibility between a resulting GND density and the plastic shear, $\boldsymbol{\kappa}^{\perp} = \frac{1}{b}\nabla\gamma_s$. One way of guaranteeing these conditions is to create initial values in a 2-dimensional slip plane by superposition of objects which a priori fulfill these conditions. E.g. one may choose a closed dislocation loop of radius R with center point $\mathbf{r}_0$; a point $\mathbf{r}$ in $\Gamma_{s,g}$ then has the distance $d = |R(-\sin\varphi, \cos\varphi) + \mathbf{r}_0 - \mathbf{r}|$ from the loops' line and the density and the curvature can be obtained by 'smearing-out' the line such that the total line length $2\pi R$ is preserved, i.e.,

$$\rho(\mathbf{r}, \varphi) = \begin{cases} \frac{R\exp(-1/(1-(d/d_0)^2))}{2\pi \int_0^{d_0} t\exp(-1/(1-(t/d_0)^2))\,\mathrm{d}t} & \text{if} \quad d < d_0\,, \\ 0 & \text{else,} \end{cases}$$

where the parameter d_0 governs the width of the compact density distribution around the line. Note, that this results in an area density, i.e. ρ has the unit of line length per area. The curvature density can be obtained as $q(\mathbf{r}, \varphi) = \dfrac{\rho(\mathbf{r}, \varphi)}{R}$. The corresponding plastic slip generated by the expanded loop is given by $\gamma(\mathbf{r}) = b\displaystyle\int_{|\mathbf{r}-\mathbf{r}_0|}^{R+d_0}\int_0^{2\pi}\rho(\eta, 0, \varphi)\,\mathrm{d}\varphi\,\mathrm{d}\eta$. We superimpose N_d such dislocation loops with randomly chosen centers of the loops with a uniform distribution and such that the compact function for the CDD fields fits completely into the slip plane. Additionally, the loops' radii are chosen from a uniform random distribution. The 1D-slip planes represent a homogeneous distribution into the second direction, so that we integrate the CDD fields along the width for $\rho_{s,g}(\xi), q_{s,g}(\xi)$ and $\gamma_{s,g}(\xi)$, see Fig. 5.2 for an visualization.

5.5.2 Evolution of CDD field quantities for Study 3

The following figures show the evolution of total density for the single and double slip system (Fig. 5.10). The largest difference in these two situations is that due to the different stress state in double slip the dislocation activity is much more pronounced. In Fig. 5.11 also the profiles for all relevant CDD field quantities and stress components are shown. One of the key feature of hdCDD is that the distinction into GNDs and SSDs is obtained naturally from the higher-dimensional configuration space. This can be also observed in the evolution of the integrated quantities ρ^{tot} and κ^{edge} in Fig. 5.11 (a)+(b) and (g)+(h). Therein, the difference $\rho^{\text{tot}} - |\kappa^{\text{edge}}|$ would yield the SSD density of edges.
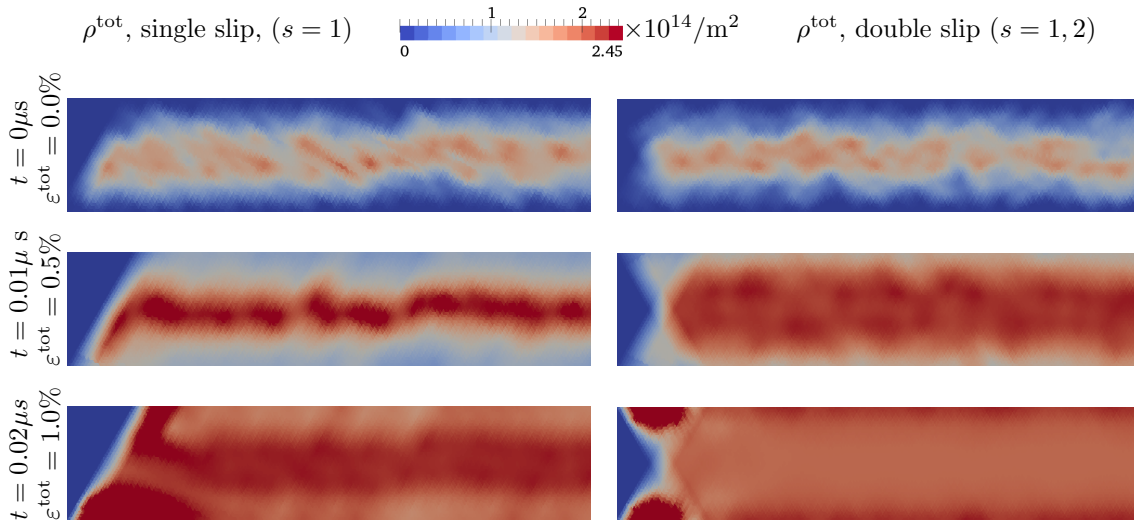

Figure 5.10: Initial distribution and time evolution of total density $\rho_{s,g}^{\text{tot}}$ for Case 2, Study 3, for system with $s = 1$ and $s = 1, 2$ at $t = 0.01$ µs and $t = 0.02$ µs with open boundary conditions for the dislocation density.

profiles for the single slip configuration

(a) total density

(b) GND density (edges)

(c) plastic slip

(d) line tension

(e) yield stress

(f) velocity

profiles for the double slip configuration

(g) total density

(h) GND density (edges)

(i) plastic slip

(j) line tension
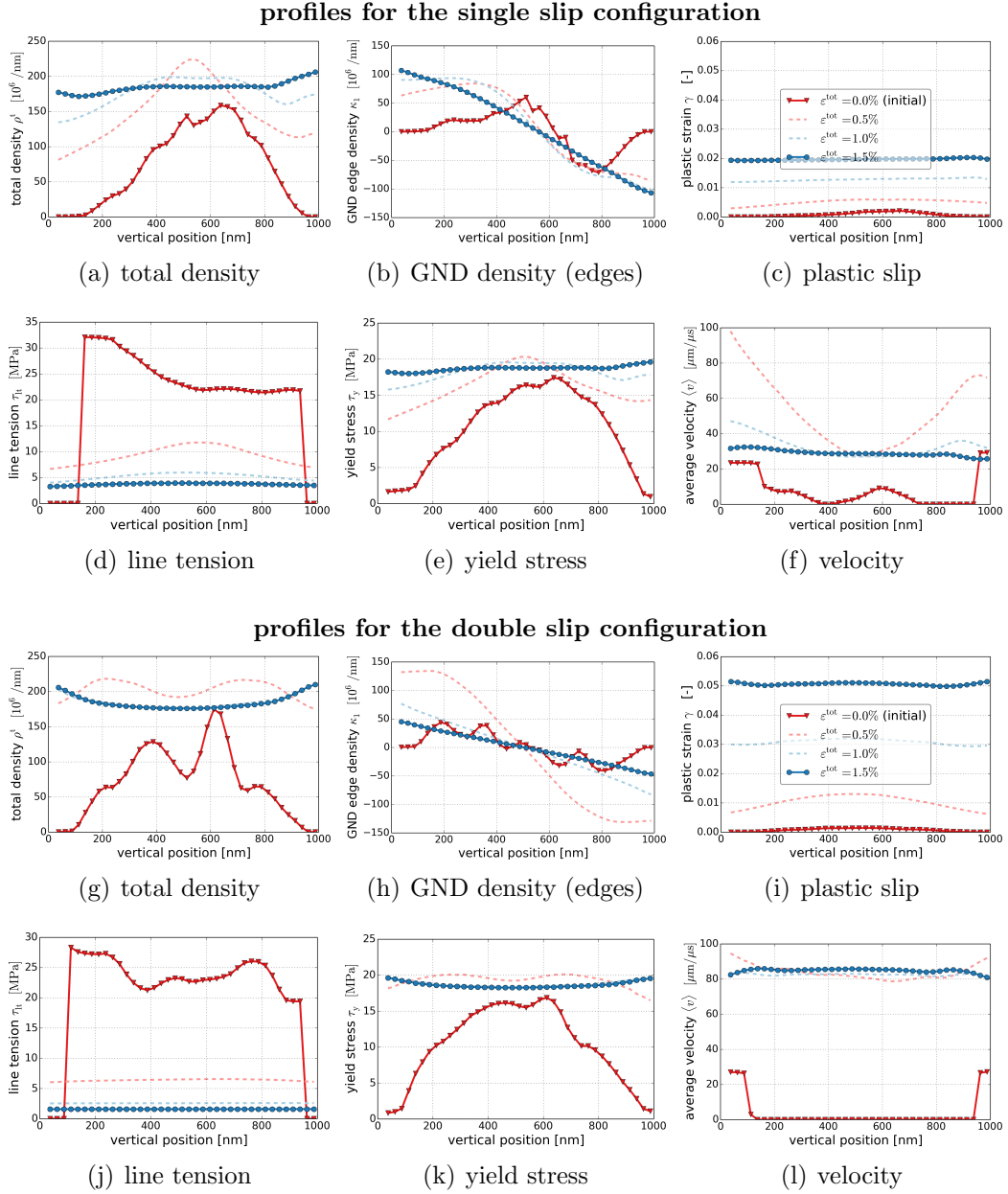

(k) yield stress

(l) velocity

Figure 5.11: Profiles of CDD field variables along a center slip plane for single slip (a-f) and double slip (g-l) configuration. Density values and plastic slip for the double slip configuration (a)-(c) were multiplied by a factor of 2 to make them comparable with the single slip configuration.

6 | Implementation

We present a parallel data structure for discontinuous Galerkin (DG) methods based on the previous M++ library which was originally designed for finite element methods (FEM) by using the Distributed Point Objects concept. M++ has many attractive features, for example transparent parallel computation, parallel direct and iterative linear solvers, parallel preconditioners such as multigrid. We also define an additional abstract linear algebra model extended to M++.

6.1 A parallel mesh model

For keeping an abstract programming model with a transparent parallel code it is required to modify some M++ structures especially with nodal points according to the discontinuous property of the test space in DG. We repeat the configuration in Wieners (2010) by considering the finest mesh as $(\mathcal{C}, \mathcal{V}, \mathcal{E}, \mathcal{F})$ of cells $\mathcal{C}$, vertices $\mathcal{V}$, edges $\mathcal{E}$ and faces $\mathcal{F}$.

Let $c \in \mathcal{C}$ be a cell, $\mathcal{V}_c \subset \mathbb{R}^3$ be the cell vertices, $\mathcal{E}_c$ be the cell edges, and $\mathcal{F}_c$ be the cell faces. For each edge $e \in \mathcal{E}_c$ is represented by a pair $(x_e, y_e) \in \mathcal{V}_c \times \mathcal{V}_c$ and its edge midpoint $z_e \in \mathbb{R}^3$. In similar fashion we also use the face midpoint z_f and the cell midpoint z_c as the corresponding keys of $f \in \mathcal{F}_c$ and $c \in \mathcal{C}$, respectively. Then we define $\mathcal{Z}_c = \mathcal{V}_c \cup \{z_e : e \in \mathcal{E}_c\} \cup \{z_f : f \in \mathcal{F}_c\} \cup \{z_c\}$ be the set of hash keys associated to the cell c. Moreover we need additional representation for each interior face f to make a connection between two cells $c, c' \in \mathcal{C}$ with $f \in \mathcal{F}_c \cap \mathcal{F}_{c'}$ by the pair of midpoints $(z_c, z_{c'})$. And we introduce the exceptional point $z = \infty$, then for a boundary faces $f \in \mathcal{F}_c$ are associated to the pair (z_c, ∞).

Then we preform a distribution of the mesh by a load balancing procedure on the processor set $\mathcal{P} = \{1, .., P\}$, where the load balancing is given by a function

$$\text{dest} : \mathcal{C} \to \mathcal{P}, \quad \mathcal{C}^p = \{c \in \mathcal{C} : \text{dest}(c) = p\},$$

defining a disjoint decomposition $\mathcal{C} = \mathcal{C}^1 \cup ... \cup \mathcal{C}^P$. This also defines $\mathcal{V}^p = \cup_{c \in \mathcal{C}^p} \mathcal{V}_c$, $\mathcal{E}^p = \cup_{c \in \mathcal{C}^p} \mathcal{E}_c$, $\mathcal{F}^p = \cup_{c \in \mathcal{C}^p} \mathcal{F}_c$ and $\mathcal{Z}^p = \cup_{c \in \mathcal{C}^p} \mathcal{Z}_c$. For the representation of boundary faces of process $\mathcal{C}^p$, such that $f \in \mathcal{F}^P$ associated with $(z_c, z_{c'})$ where $c \in \mathcal{C}^p$ but $c' \notin$

$\mathcal{C}^p$, we replace this with (z_c, ∞). This constructions give overlapping decompositions of the vertices $\mathcal{V} = \mathcal{V}^1 \cup ... \cup \mathcal{V}^P$, the edges $\mathcal{E} = \mathcal{E}^1 \cup ... \cup \mathcal{E}^P$, the faces $\mathcal{F} = \mathcal{F}^1 \cup ... \cup \mathcal{F}^P$ and the hash key $\mathcal{Z} = \mathcal{Z}^1 \cup ... \cup \mathcal{Z}^P$. The overlapping decomposition of the hash keys $\mathcal{Z}$ defines a set-valued partition map

$$\pi : \mathcal{Z} \to 2^{\mathcal{P}}, \quad \pi(z) = \{p \in \mathcal{P} : z \in \mathcal{Z}^p\}.$$

Remark : With this setting we always have $\pi(z_c) = 1$, $c \in \mathcal{C}$, in order to the disjoint decomposition of $\mathcal{C}$. We do the remark here because this will be modified for DG methods which we will see later. This modification will cause us some problems and the solution will be presented later.

In conforming FEM we have to take care of the consistency of value over nodal points on these overlapping decompositions, but in the case of DG these value are already related to different values, so the consistency over them is not needed. But as we can see in the numerical scheme, the information over the neighboring cells is required for the numerical flux $\mathbf{F}^*$. With this requirement, we define a set of **overlapping cells** together with the previous distributed mesh on each processor.

6.1.1 Overlapping cells

We define a distribution of the overlapping cells by a function

$$\begin{aligned} \text{overlap} : \mathcal{C} \;\; &\to \;\; \mathcal{P} \cup \{0\}, \\ c \;\; &\mapsto \;\; \begin{cases} p, & \exists f \in \mathcal{F}_c \text{ such that } f \in \mathcal{F}^p \text{ and } c \notin \mathcal{C}^p \\ 0, & \text{else} \end{cases} \end{aligned}$$

then define

$$\begin{aligned} \mathcal{O}_{\mathcal{C}}^p \;\; &= \;\; \{c \in \mathcal{C} : \text{overlap}(c) = p\}, \\ \mathcal{O}_{\mathcal{F}}^p \;\; &= \;\; \{f \in \mathcal{F}_c : c \in \mathcal{O}^p\}. \end{aligned}$$

Since the important components for DG methods are just cells and faces, then we do the modification just on $\mathcal{C}^p$ and $\mathcal{F}^p$ by ignoring $\mathcal{E}^p$ and $\mathcal{V}^p$. We perform the extended constructions

$$\widetilde{\mathcal{C}}^p = \mathcal{C}^p \cup \mathcal{O}_{\mathcal{C}}^p, \quad \widetilde{\mathcal{F}}^p = \mathcal{F}^p \cup \mathcal{O}_{\mathcal{F}}^p, \quad \widetilde{\mathcal{Z}}^p = \mathcal{Z}^p \cup \widetilde{\mathcal{C}}^p \cup \widetilde{\mathcal{F}}^p,$$

and then modify the partition map as

$$\widetilde{\pi} : \mathcal{Z} \to 2^{\mathcal{P}}, \quad \widetilde{\pi}(z) = \{p \in \mathcal{P} : z \in \widetilde{\mathcal{Z}}^p\}.$$

6.2 Parallel discontinuous Galerkin

For a purpose of comparison, we first repeat the configurations of finite element mesh as in Wieners (2010) which is given by a decomposition $\overline{\Omega} = \cup_{c \in \mathcal{C}} \overline{\Omega}_c$, where $\overline{\Omega}_c = \text{conv}\{\mathcal{V}_c\} \subset \mathbb{R}^3$, together with non-overlapping sub-domains $\overline{\Omega}^p = \cup_{c \in \mathcal{C}^p} \overline{\Omega}_c$. The finite element space $V = \text{span}\{\phi_i : i \in \mathcal{I}\}$ with basis ϕ_i, where $\mathcal{I}$ is the corresponding index set. Each basis function ϕ_i is associated with a dual function $\phi'_i \in V'$ such that $\langle \phi'_i, \phi_k \rangle = \delta_{ik}$ and every index $i \in \mathcal{I}$ is assigned with a nodal point $z_i \in \overline{\Omega}$. The set of nodal points is defined with $\mathcal{N} = \{z_i : i \in \mathcal{I}\}$, and in M++ we also have $\mathcal{N} \subset \mathcal{Z}$.

In case of discontinuous Galerkin, a DG mesh is also given by a decomposition $\overline{\Omega}$, and additionally comes together with overlapping sub-domains $\widetilde{\overline{\Omega}^p} = \cup_{c \in \widetilde{\mathcal{C}^p}} \overline{\Omega}_c$. We define

$$V_{DG} = \text{span}\{\phi_{c,i} : i \in \mathcal{I}_c, c \in \mathcal{C}\}$$

be a DG space with basis $\phi_{c,i}$, where $\mathcal{I}_c$ is the corresponding index set over each cell c. In order to the local property of basis function $\phi_{c,i}$, we have a associated dual function $\phi'_{c,i} \in V'_{DG}$ such that $\langle \phi'_{c,i}, \phi_{c',k} \rangle = \delta_{cc'}\delta_{ik}$. To distinguish the nodal points for the discontinuous space between cells, we group the local nodal points on each cell together and make them associate with the middle cell point z_c. The result is that we have to assign the nodal points in the setting of M++ to the center of the cells, so we have $\mathcal{N}_{DG} = \{z_c : c \in \mathcal{C}\}$ as the set of nodal points.

With this setting, we still have $\mathcal{N}_{DG} \subset \mathcal{Z}$ and moreover we define the local nodal points on each cell to be $\mathcal{N}_{DG,c} = \{z_i : i \in \mathcal{I}_c\}$. Then we can assign a basis function $\phi_{c,i}$ to a pair of nodal points $(z_c, z_i) \in \mathcal{N}_{DG} \times \mathcal{N}_{DG,c}$. We give a remark that $\#\mathcal{I}_c$ is depended on the order of the polynomial in the cell, this means with a normal DG space which we have a homogeneous order of polynomial over the domain then $\#\mathcal{I}_c$ is constant, for example in $\mathbb{R}^3$ we have 4 for linear tetrahedral and 10 for quadratic tetrahedral in a scalar space and 12 and 30 in a vector space, respectively.

The representation of a DG function $v = \sum_{c \in \mathcal{C}, i \in \mathcal{I}_c} v_{c,i}\phi_{c,i} \in V_{DG}$ is uniquely defined by its coefficient vector $(v_{c,i})_{c \in \mathcal{C}, i \in \mathcal{I}_c}$ with $v_{c,i} = \langle \phi'_{c,i}, v \rangle$. Similarly, a discrete functional $f = \sum_{c \in \mathcal{C}, i \in \mathcal{I}_c} f_{c,i}\phi'_{c,i} \in V'_{DG}$ is also uniquely represented by its coefficient vector $(f_{c,i})_{c \in \mathcal{C}, i \in \mathcal{I}_c}$ with $f_{c,i} = \langle f, \phi_{c,i} \rangle$.

6.2.1 DG parallel vector representation

We can see that both basis function $\phi_{c,i}$ and its dual function $\phi'_{c,i}$ are locally contributed on each cell. It is obviously not similar to the FEM case, because a basis function ϕ_i is partly contributed to the cells contained the associated nodal point

of ϕ_i. This means that the parallel vector representation such as an additive vector representation, which was introduced in M++ for FEM, is not needed, since the contribution of the vector is just located in the local domain on each processor, and the consistent vector representation also need to be modified. Therefore with an additional setting of overlapping cells, we have to keep the consistency of their values by defining a new **the consistent overlapping vector representation** for the DG parallel vector representation.

Consistent overlapping vector representation

This representation is used for both the coefficient vectors of DG function $(v_{c,i})_{c\in\mathcal{C},i\in\mathcal{I}_c}$ and its dual $(f_{c,i})_{c\in\mathcal{C},i\in\mathcal{I}_c}$. Since the local nodal points on each cell already group together by using its midpoint, then it is more convenient to represent the vector just as $(v_c)_{c\in\mathcal{C}}$, where $v_c = (v_{c,1}, ..., v_{c,n})^\top, n = \#\mathcal{I}_c$ is a subvector and also similar for $(f_c)_{c\in\mathcal{C}}$.

The coefficient vector $(v_c)_{c\in\mathcal{C}}$ of DG function $v \in V_{DG}$ is presented in parallel by its local restrictions $\underline{v}^p = (v_c)_{c\in\widetilde{\mathcal{C}}^p}$ which defines a mapping

$$
\begin{aligned}
E : V_{DG} &\rightarrow \underline{V_{DG}}^{\mathcal{P}} \\
v &\mapsto \underline{v} = (\underline{v}^p)_{p\in\mathcal{P}}.
\end{aligned}
$$

Then we define the constrained product space

$$
\underline{V_{DG}} = \{\underline{v} \in \underline{V_{DG}}^{\mathcal{P}} : v_c^q = v_c^p \text{ for } q \in \widetilde{\pi}^p(z_c), c \in \mathcal{C}^p\}.
$$

We have $\underline{V_{DG}} = E(V_{DG})$ and for $\underline{v} \in \underline{V_{DG}}$ a unique DG function $v \in V_{DG}$ with $E(v) = \underline{v}$ is well-defined.

Remark : The different setting of the consistent overlapping vector and the consistent vector representation defined in Wieners (2010) is that here we consider v_c^p to be a master subvector of the overlaping subvectors set $\{v_c^q, q \in \widetilde{\pi}^p(z_c), c \in \mathcal{C}^p\}$ but the representation in Wieners (2010) doesn't need a master value.

6.2.2 DG parallel matrix representation

For a parallel matrix representation for DG, we can use **the additive operator representation** defined in Wieners (2010), since the operator in DG scheme is always divided to the contribution of cells and contribution of faces. Then it is obviously that the addition of these contributions are needed over the common interior faces between processors.

Remark : It should be remarked that the parallel assembling of a matrix for DG operator in the processor p is considered only for cells $c \in \mathcal{C}^p$, then the diagonal block matrices of overlapping cells $c \in \mathcal{O}_{\mathcal{C}}^p$ are always zeros.

6.3 Parallel linear algebra

Since the additive and consistent representations previously defined in Wieners (2010) are avoided in DG function spaces, V_{DG} and V'_{DG}, the idea for reliable, transparent and efficient implementation of parallel algorithms also has to be modified. Therefore instead of the collect and accumulate procedures, the new overlap consistent procedure needs to be performed for vectors in V_{DG} of DG functions and vectors in V'_{DG} of discrete DG functionals. The new parallel operation to keep the consistency of vectors are defined below,

a) A unique DG parallel vector representation is obtained by

$$\text{OverlapConsistent} \quad : \quad \underline{V_{DG}}^{\mathcal{P}} \to \underline{V_{DG}}$$

defined by

$$\text{OverlapConsistent}(v)_c^p \quad = \quad v_c^q, \quad q \in \widetilde{\pi}(z_c), \quad c \in \mathcal{C}^q;$$

This parallel operation require only communication with the neighbouring processors

$$\mathcal{P}_p \quad = \quad \bigcup_{p \in \widetilde{\pi}(z_c)} \widetilde{\pi}(z_c), \quad c \in \mathcal{O}_{\mathcal{C}}^p.$$

The parallel data exchange in the overlap consistent routine is realized by identifying the indices by center of overlapping cells, z_c, used as a group of local nodal points in each cell.

Remark : The alternative of the overlap consistent can be achieved by using the parallel operations, collect and accumulate, by changing the master processor for every index over the overlapping cells for the additive vector representation as, $p = q : q \in \widetilde{\pi}(z_c), c \in \mathcal{C}^q$ instead of $p = \min \widetilde{\pi}(z_c)$. In the recent implementation the method of master processor modification has been used and working well with the existed FEM algorithms.

7 | Summary and Outlook

We proposed the model of elasto-plasticity that based on dislocation densities obtained from the higher-dimensional Continuum Dislocations Dynamics (hdCDD) theory. The representative slip planes are introduced and the micro structure behavior of dislocation densities and curvature densities happened within this domain. The full setting are provided by embedding multiple of representative slip planes into the elastic body.

The hdCDD theory was formulated in a more precise mathematical setting called Friedrichs' system. This formulation provided us a good framework to analyze and construct numberical methods. With this general form we showed the well-posedness for the open boundary of hdCDD together with the assumption that the velocity does not depend on the orientation direction. In the first glance of numerical methods, the explicit RKDG methods were used and the error analysis with the RK third order were considered and numerical results had been obtained. Furthermore, the new type of basis functions called Finite Volume Fourier elements (FVF) was introduced to reduce the degree of freedom for the space discretization with dG-method and overcome the mesh distribution problem for the embedded slip planes in the parallel implementation.

In the numerical experiments, these model formulations were then applied to simulate different plain-strain slip geometries under tensile and shear loading conditions together with different physical boundary conditions. We analyzed in detail how systems of dislocations evolve while they interact with each other due to short-range and long-range stress components. In doing so we could directly link the dislocation microstructure – represented by the higher-dimensional density and curvature density – to the macroscopic behavior (e.g. stress-strain response or average density). By comparing to systems of straight edge dislocations we observed that the line curvature has a strong influence on the hardening behavior: not only did the stress-strain curve change quantitatively, it also changed qualitatively which would be explained by hdCDD. Furthermore, we showed how physical boundary conditions influence the orientation distribution of dislocations and again, how this impacts the system response. Finally, we studied a double slip configuration where we could

again attribute the distinctly different hardening behavior for single/double slip to microstructural aspects.

However, this work is just only the beginning of the investigation of elasto-plasticity model based on hdCDD. A lot of simplifications of the hdCDD system were made to make the mathematical analysis and numerical treatments feasible. The interesting studies in the future can be, for example, allowing velocity to depend on orientation directions and even dislocation densities and curvature densities. This will activate more interesting behaviors of the system and maybe provide the possibility to analyze the impenetrable boundary and pile up situations.

The hdCDD model contains microstructural information which otherwise is only available in DDD simulations. These microstructural details have a strong influence on the system response, which is why a comparison with other models is difficult: no other standard continuum plasticity model is able to represent e.g. the conversion of SSDs into GNDs and the dislocation line length production accompanied by expansion of dislocation loops. Thus, direct comparisons with DDD simulation will be extremely interesting and helpful to further benchmark our model. The necessary extraction of information from DDD simulations and converting them into continuous fields, however, is a non trivial task which needs to be undertaken with care in future work. Additionally, DDD could be used to identify physical formulations for incorporating further dislocation interactions and reactions into our continuum model. With this we hope to go beyond what up to date is possible with DDD and apply CDD to realistic three-dimensional systems with large numbers of interacting dislocations and plastic strain.

Bibliography

E.C. Aifantis. On the microstructural origin of certain inelastic models. *Journal of Engineering Materials and Technology*, 106(4):326–330, 1984.

A. Arsenlis, W. Cai, M. Tang, M. Rhee, T. Oppelstrup, G. Hommes, T. G. Pierce, and V. V. Bulatov. Enabling strain hardening simulations with dislocation dynamics. *Model. Simul. Mater. Sci. Eng.*, 15:553–595, 2007.

Athanasios Arsenlis, David M. Parks, Richard Becker, and Vasily V. Bulatov. On the evolution of crystallographic dislocation density in non-homogeneously deforming crystals. *J. Mech. and Phys. Solids*, 52(6):1213–1246, June 2004. doi: 10.1016/j.jmps.2003.12.007.

E. Arzt. Size effects in materials due to microstructural and dimensional constraints: a comparative review. *Acta Mater.*, 46(16):5611–5626, 1998.

M.F. Ashby. The deformation of plastically non-homogeneous materials. *Phil. Mag.*, 21:399–424, 1970.

JP Aubin. Applied functional analysis. 2000. *Pure and Applied Mathematics (New York)*, 2000.

B. A. Bilby, R. Bullough, and E. Smith. Continuous distributions of dislocations: A new application of the methods of non-riemannian geometry. *Proc. Roy. Soc. London Ser. A*, 231:263–273, 1955.

V. V. Bulatov and Cai W. Nodal effects in dislocation mobility. *Phys. Rev. Lett.*, 89(11):115501 1–4, 2002. doi: 10.1103/PhysRevLett.89.115501.

Erik Burman, Alexandre Ern, and Miguel A Fernández. Explicit Runge-Kutta schemes and finite elements with symmetric stabilization for first-order linear PDE systems. *SIAM Journal on Numerical Analysis*, 48(6):2019–2042, 2010.

Bernardo Cockburn and Chi-Wang Shu. The Runge-Kutta local projection P1-discontinuous-Galerkin finite element method for scalar conservation laws. *RAIRO-Modélisation Mathématique et Analyse Numérique*, 25(3):337–361, 1991.

Patrick Cordier, Sylvie Demouchy, Benoît Beausir, Vincent Taupin, Fabrice Barou, and Claude Fressengeas. Disclinations provide the missing mechanism for deforming olivine-rich rocks in the mantle. *Nature*, 507(7490):51–56, 2014.

V.S. Deshpande, A. Needleman, and E. Van der Giessen. Plasticity size effects in tension and compression of single crystals. *J. Mech. Phys. Solids*, 53(12):2661–2691, DEC 2005. ISSN 0022-5096. doi: 10.1016/j.jmps.2005.07.005.

B. Devincre and L. P. Kubin. Mesoscopic simulations of dislocations and plasticity. *Mater. Sci. Eng. A*, 8:234–236, 1997.

Daniele Antonio Di Pietro and Alexandre Ern. *Mathematical aspects of discontinuous Galerkin methods*, volume 69. Springer Science & Business Media, 2011.

A. El-Azab. Statistical mechanics treatment of the evolution of dislocation distributions in single crystals. *Phys. Rev. B*, 61(18):11956–11966, May 2000. doi: 10.1103/PhysRevB.61.11956.

Alexandre Ern and Jean-Luc Guermond. *Theory and practice of finite elements, vol. 159 of Applied Mathematical Sciences*. Springer-Verlag, New York, 2004.

Alexandre Ern and Jean-Luc Guermond. Discontinuous Galerkin methods for Friedrichs' systems. I. General theory. *SIAM Journal on Numerical Analysis*, 44(2):753–778, 2006.

Alexandre Ern, Jean-Luc Guermond, and Gilbert Caplain. An Intrinsic Criterion for the Bijectivity of Hilbert Operators Related to Friedrichs' Systems. *Communications in Partial Differential Equations*, 32(2):317–341, 2007.

Ray S. Fertig and Shefford P. Baker. Simulation of dislocations and strength in thin films: A review. *Progress in Materials Science*, 54(6):874–908, 2009.

M. Fivel, M. Verdier, and G. Ganova. 3d simulation of a nanoindentation test at a mesoscopic scale. *Mat. Sci. Eng. A*, 234–236:923–926, 1997.

N.A. Fleck, G.M. Muller, M.F. Ashby, and J.W. Hutchinson. Strain gradient plasticity - theory and experiment. *Acta Metall. et Mater.*, 42(2):475–487, 1994.

P. Fredriksson and P. Gudmundson. Size-dependent yield strength of thin films. *Int. J. Plasti.*, 21(9):1834–1854, 2005. ISSN 0749-6419. doi: http://dx.doi.org/10.1016/j.ijplas.2004.09.005.

Huajian Gao and Yonggang Huang. Geometrically necessary dislocation and size-dependent plasticity. *Scripta Mater.*, 48(2):113 – 118, 2003.

N.M. Ghoniem, S. Tong, and L. Sun. Parametric dislocation dynamics: A thermodynamics-based approach to investigations of mesoscopic plastic deformation. *Phys. Rev. B*, 2000.

I. Groma. Link between the microscopic and mesoscopic length-scale description of the collective behavior of dislocations. *Phys. Rev. B*, 56(10):5807–5813, Sep 1997. doi: 10.1103/PhysRevB.56.5807.

I. Groma, F.F. Csikor, and M. Zaiser. Spatial correlations and higher-order gradient terms in a continuum description of dislocation dynamics. *Acta Mater.*, 51:1271–1281, 2003.

Morton E. Gurtin. A gradient theory of single-crystal viscoplasticity that accounts for geometrically necessary dislocations. *J. Mech. Phys. Sol.*, 50(1):5–32, 2002. ISSN 0022-5096. doi: DOI:10.1016/S0022-5096(01)00104-1.

Morton E. Gurtin, Lallit Anand, and Suvrat P. Lele. Gradient single-crystal plasticity with free energy dependent on dislocation densities. *Journal of the Mechanics and Physics of Solids*, 55(9):1853–1878, 2007.

Morton E. Gurtin, Eliot Fried, and Lallit Anand. *The mechanics and thermodynamics of continua.* Cambridge University Press, 2010.

J.S. Hesthaven and T. Warburton. *Nodal discontinuous Galerkin methods: algorithms, analysis, and applications.* Springer Verlag, 2007.

Marlis Hochbruck, Tomislav Pažur, Andreas Schulz, Ekkachai Thawinan, and Christian Wieners. Efficient time integration for discontinuous galerkin approximations of linear wave equations. *ZAMM-Journal of Applied Mathematics and Mechanics/Zeitschrift für Angewandte Mathematik und Mechanik*, 95(3):237–259, 2015.

T. Hochrainer. *Evolving systems of curved dislocations: Mathematical foundations of a statistical theory.* PhD thesis, University of Karlsruhe, IZBS, 2006.

T. Hochrainer, M. Zaiser, and P. Gumbsch. A three-dimensional continuum theory of dislocation systems: kinematics and mean-field formulation. *Phil. Mag.*, 87 (8-9):1261–1282, 2007.

T. Hochrainer, M. Zaiser, and P. Gumbsch. Dislocation transport and line length increase in averaged descriptions of dislocations. *AIP Conference Proceedings*, 1168(1):1133–1136, 2009. doi: 10.1063/1.3241258.

T. Hochrainer, S. Sandfeld, M. Zaiser, and P. Gumbsch. Continuum dislocation dynamics: towards a physical theory of crystal plasticity. *J. Mech. and Phys. Solids*, http://dx.doi.org/10.1016/j.jmps.2013.09.012, 2013.

Thomas Hochrainer. Multipole expansion of continuum dislocations dynamics in terms of alignment tensors. *Philosophical Magazine*, 95(12):1321–1367, 2015.

N.J. Hoff. First IUTAM colloquium on creep in structures, 1960.

Max Jensen. *Phd Thesis: Discontinuous Galerkin Methods for Friedrichs Systems with Irregular Solutions.* University of Oxford, 2004.

K. Kondo. On the geometrical and physical foundations of the theory of yielding. *Proc. 2. Japan Nat. Congress of Appl. Mech.*, pages 41–47, 1952.

A. M. Kosevich. Crystal dislocations and the theory of elasticity. In F. R. Nabarro, editor, *Dislocations in Solids*, volume 1, pages 33–141. North Holland, Amsterdam, 1979.

Ekkehart Kröner. *Kontinuumstheorie der Versetzungen und Eigenspannungen.* Springer, 1958.

L.P. Kubin and G. Canova. The modeling of dislocation patterns. *Scripta Metall. Mater.*, 27(8):957–962, 1992.

Z.L. Liu, Z. Zhuang, X.M. Liu, X.C. Zhao, and Z.H. Zhang. A dislocation dynamics based higher-order crystal plasticity model and applications on confined thin-film plasticity. *International Journal of Plasticity*, 27(2):201–216, 2011. ISSN 0749-6419. doi: http://dx.doi.org/10.1016/j.ijplas.2010.04.004.

AEH Love. *The mathematical theory of elasticity.* 1927.

Alexander Mielke. Evolution of rate-independent systems. *Evolutionary equations*, 2:461–559, 2005.

M. Monavari, M. Zaiser, and S. Sandfeld. Comparison of closure approximations for continuous dislocation dynamics. *Mater. Res. Soc. Symp. Proc.*, 1651, 2014. doi: 10.1557/opl.2014.62.

N. Nikitas. *Dislocation-based continuum models of crystal plasticity on the micron scale.* PhD thesis, The University of Edinburgh, 2008.

W. D. Nix and H. Gao. Indentation size effects in crystalline materials: A law for strain gradient plasticity. *Journal of the Mechanics and Physics of Solids*, 46(3): 411–425, 1998.

J.F. Nye. Some geometrical relations in dislocated crystals. *Acta Metall.*, 1:153–162, 1953.

E. Orowan. Zur Kristallplastizität. *Z. Phys.*, 89:605–659, 1934.

M. Polanyi. Über eine Art Gitterstörung, die einen Kristall plastisch machen könnte. *Z. Phys.*, 89:660–664, 1934.

B Dayanand Reddy, Christian Wieners, and Barbara Wohlmuth. Finite element analysis and algorithms for single-crystal strain-gradient plasticity. *International Journal for Numerical Methods in Engineering*, 90(6):784–804, 2012.

C. Reuber, P. Eisenlohr, F. Roters, and D. Raabe. Dislocation density distribution around an indent in single-crystalline nickel: Comparing nonlocal crystal plasticity finite-element predictions with experiments. *Acta Materialia*, 71(0):333–348, 2014. ISSN 1359-6454.

S. Sandfeld. The evolution of dislocation density in a higher-order continuum theory of dislocation plasticity. *Shaker Verlag Aachen, Germany*, 2010a.

S. Sandfeld, T. Hochrainer, M. Zaiser, and P. Gumbsch. Numerical implementation of a 3d continuum theory of dislocation dynamics and application to microbending. *Philos. Mag.*, 90(27):3697–3728, 2010.

S. Sandfeld, T. Hochrainer, M. Zaiser, and P. Gumbsch. Continuum modeling of dislocation plasticity: Theory, numerical implementation and validation by discrete dislocation simulations. *J. Mater. Res.*, 2011.

Stefan Sandfeld. *Phd Thesis: The Evolution of Dislocation density in a higher-order Continuum Theory of Dislocation Plasticity.* Karlsruhe Institue of Technology, 2010b.

Stefan Sandfeld and Giacomo Po. Direct microstructural comparison of discrete and continuum dislocation models. *arXiv preprint arXiv:1506.09167*, 2015.

Stefan Sandfeld, Mehran Monavari, and Michael Zaiser. From systems of discrete dislocations to a continuous field description: stresses and averaging aspects. *Modelling and Simulation in Materials Science and Engineering*, 21(8):085006, 2013.

Stefan Sandfeld, Ekkachai Thawinan, and Christian Wieners. A link between microstructure evolution and macroscopic response in elasto-plasticity: formulation and numerical approximation of the higher-dimensional continuum dislocation dynamics theory. *International Journal of Plasticity*, 72:1–20, 2015.

K Schulz, D Dickel, S Schmitt, S Sandfeld, D Weygand, and P Gumbsch. Analysis of dislocation pile-ups using a dislocation-based continuum theory. *Modelling and Simulation in Materials Science and Engineering*, 22(2):025008, 2014.

C Schwarz, R Sedlacek, and E Werner. Application of a continuum dislocation-based model to a tensile test on a thin film. *MSE A*, 400:443–447, JUL 25 2005. ISSN 0921-5093. Intenational Conference on Fundamentals of Plastic Deformation, La Colle sur Loup, France, Sep. 13-17, 2004.

R. Sedláček, J. Kratochvíl, and E. Werner. The importance of being curved: bowing dislocations in a continuum description. *Phil. Mag.*, 83(31–34):3735–3752, 2003.

Paul Steinmann and Erwin Stein. On the numerical treatment and analysis of finite deformation ductile single crystal plasticity. *Computer Methods in Applied Mechanics and Engineering*, 129(3):235–254, 1996.

J.S. Stolken and A.G. Evans. A microbend test method for measuring the plasticity length scale. *Acta Materialia*, 46:5109–5115, 1998.

G.I. Taylor. The mechanism of plastic deformation of crystals. *Proceedings of the Royal Society of London. Series A, Mathematical and Physical Sciences*, 145:362–415, 1934.

Vito Volterra. Sur l'équilibre des corps élastiques multiplement connexes. In *Annales scientifiques de l'Ecole Normale superieure*, volume 24, pages 401–517. Société mathématique de France, 1907.

D. Weygand and P. Gumbsch. Study of dislocation reactions and rearrangements under different loading conditions. *Modell. Sim. Eng. A*, 400-401:158–161, 2005. doi: doi:10.1016/j.msea.2005.03.102.

D. Weygand, L. H. Friedman, E. van der Giessen, and A. Needleman. Aspects of boundary-value problem solutions with three-dimensional dislocation dynamics. *Modell. Simul. Mat. Sci. Eng.*, 10:437–468, 2002.

Christian Wieners. A geometric data structure for parallel finite elements and the application to multigrid methods with block smoothing. *Computing and visualization in science*, 13(4):161–175, 2010.

Christian Wieners and Barbara Wohlmuth. A primal-dual finite element approximation for a nonlocal model in plasticity. *SIAM Journal on Numerical Analysis*, 49(2):692–710, 2011.

M Zaiser and T Hochrainer. Some steps towards a continuum representation of 3d dislocation systems. *Scripta Mater.*, 54(5):717–721, MAR 2006. ISSN 1359-6462. doi: 10.1016/j.scriptamat.2005.10.060.

M. Zaiser, M.-C. Miguel, and I. Groma. Statistical dynamics of dislocation systems: The influence of dislocation-dislocationcorrelations. *Phys. Rev. B*, 64:224102, Nov 2001. doi: 10.1103/PhysRevB.64.224102.

M. Zaiser, N. Nikitas, T. Hochrainer, and E.C. Aifantis. Modelling size effects using 3d density-based dislocation dynamics. *Phil. Mag.*, 87:1283–1306, 2007.

C. Z. Zhou, S. B. Biner, and R. LeSar. Discrete dislocation dynamics simulations of plasticity at small scales. *Acta Materialia*, 58:1565–1577, 2010.